Summer 7-13-2024

OPTICAL RESPONSES OF HYBRID ELECTROMAGNETIC NANOSTRUCTURES

Dominic Bosomtwi
University of New Mexico - Main Campus

Dominic Bosomtwi

Candidate

Electrical & Computer Engineering

Department

This dissertation is approved, and it is acceptable in quality and form for publication:

Approved by the Dissertation Committee:

Dr. Viktoriia E. Babicheva , Chairperson

Dr. Christos Christodoulou

Dr. Emil Enache-Pommer

Dr. Terefe Habteyes

OPTICAL RESPONSES OF HYBRID ELECTROMAGNETIC NANOSTRUCTURES

by

DOMINIC BOSOMTWI

B.S., Physics, University of Cape Coast, 2002

M.S., Electrical & Computer Engineering,
New Mexico State University, 2009

M.S., Optical Science & Engineering,
University of New Mexico, 2020

DISSERTATION

Submitted in Partial Fulfillment of the
Requirements for the Degree of

Doctor of Philosophy
Optical Science & Engineering

The University of New Mexico
Albuquerque, New Mexico

July, 2024

Dedicated to Nana Bosomtwi and Priscilla Bosomtwi.

Acknowledgements

I would like to express my sincere gratitude to my dissertation supervisor, Professor Viktoriia E. Babicheva, for her unwavering guidance, patience, and support throughout my doctoral journey. Her expertise, encouragement, and invaluable feedback were instrumental in shaping this dissertation into its final form.

I am deeply grateful to the members of my dissertation committee: Distinguished Professor Christos Christodoulou, Professor Terefe Habteyes, and Dr. Emil Enache-Pommer of Intel Corporation. Their insightful comments, constructive criticism, and scholarly suggestions significantly enriched and improved the quality of my work.

I am also indebted to the Optical & Engineering (OSE) program at UNM for providing me with the resources, facilities, and opportunities necessary to complete this dissertation. I am particularly grateful to Professor Daniel Feezel, OSE program chair, for his invaluable support and guidance during challenging times. I would also like to express my appreciation to Ms. Doris Williams, the OSE senior academic advisor, for her administrative support and assistance.

My deepest gratitude extends to my son, Nana, and daughter, Priscilla. They have been a constant source of encouragement throughout this journey, my pillars of strength during both the highs and lows of my doctoral program.

Last but not least, I am grateful to all my friends, especially Ms. Shruti I. Gharde. Their unwavering support, encouragement, and presence throughout this challenging yet rewarding endeavor have meant the world to me.

This dissertation would not have been possible without the support and encouragement of each and every individual mentioned above. I thank you all from the bottom of my heart.

Optical Responses of Hybrid Electromagnetic Nanostructures

by

DOMINIC BOSOMTWI

B.S., Physics, University of Cape Coast, 2002

M.S., Electrical & Computer Engineering, New Mexico State University, 2009

M.S., Optical Science & Engineering, University of New Mexico, 2020

Ph.D., Optical Science & Engineering, University of New Mexico, 2024

Abstract

Fano resonances result from the interference between a broad background and a narrow state, producing asymmetric scattering profiles. Under specific conditions, destructive interference collapses the Fano resonance width, leading to bound states in the continuum (BICs) that localize light within a nanostructure while maintaining an infinitely high-quality factor (Q-factor).

This dissertation explores the design of nanostructures with multilayer hybrid plasmonic-dielectric metasurfaces using full-wave numerical simulations, facilitating multiple Fano resonances and BICs. By adjusting nanoantenna dimensions, multiple modes are excited at plasmonic-dielectric interfaces, leading to strong interactions and hybridization of energy levels, manifested as Rabi splitting.

These findings enable advancements in photonics, including tunable devices, high-Q-factor resonators, and optical filters. Additionally, the study designs nanostructures to enhance plasmonic hot electron generation from gold nanoelectrodes, optimizing lattice periods for maximum field enhancement and electron injection into water, offering guidelines for designing plasmonic nanostructures for hot electron applications.

Contents

Chapter 1

Contents

1.0 Introduction

Electromagnetic nanostructures, characterized by their layered configurations of alternating materials with distinct refractive indices, arranged in periodic or quasi-periodic formations, have emerged as a powerful tool for manipulating light at the nanoscale. These structures exhibit unique optical properties due to the interference, coupling, and confinement of electromagnetic waves within them. This has driven extensive research and development efforts in recent years [1-3].

Several well-established examples of layered nanostructures include photonic crystals, negative-index metamaterials (NIMs), plasmonic nanostructures, and optical and hybrid metasurfaces. Each type offers distinct advantages and finds application in a specific set of areas.

Photonic crystals excel at controlling light propagation within periodic dielectric structures [3].

Negative-index metamaterials (NIMs) derive their unusual properties from carefully designed sub-wavelength inclusions [4].

Plasmonic nanostructures exploit the collective oscillations of free electrons at metal-dielectric interfaces [5].

In contrast to their three-dimensional counterparts, optical metasurfaces offer several advantages: reduced losses, easier fabrication, and enhanced ability to manipulate light propagation. These features have revolutionized the field of optics, enabling functionalities like aberration-free lensing, wavefront shaping, and polarization control that surpass the limitations of conventional optical components [6].

The ability of optical metasurfaces to manipulate the phase, amplitude, and polarization of light locally stems from the careful design of individual scatterers. By engineering the geometry, size, orientation, and material composition of these scatterers, one can encode specific optical responses that achieve the desired functionalities. This design flexibility allows for a high degree of control over light, facilitating applications in diverse areas ranging from advanced imaging systems and sensors to optical communications and energy harvesting [6, 7].

Hybrid metasurfaces are essentially two-dimensional structures composed of subwavelength elements that can manipulate and alter electromagnetic waves. However, their unique characteristic lies in their composition. They combine different materials and structures, each with distinct properties, into a unified platform.

The concept of "hybrid" originates from an innovative strategy to merge the strengths of different components, such as plasmonic, dielectric, and even active materials, into a single metasurface. This approach not only leverages the advantages of individual elements but also minimizes their respective drawbacks, creating a versatile and robust system for manipulating light at the nanoscale [7, 8].

The benefits of hybrid metasurfaces are multifaceted. Firstly, they offer increased design flexibility, enabling the creation of multifunctional and tunable optical elements. By harnessing the advantageous properties of diverse components, they achieve a broader spectrum of light manipulation capabilities, exceeding the limitations of traditional optical elements [8, 9].

Secondly, hybrid metasurfaces can potentially exhibit enhanced performance in terms of efficiency and bandwidth. This is achieved by strategically integrating materials with complementary characteristics, which is particularly valuable in applications demanding high performance, such as holography, imaging, and sensing [8, 9].

Thirdly, by incorporating active materials, hybrid metasurfaces can achieve dynamic tunability, a highly sought-after feature that allows real-time control of optical responses. This tunability can be triggered by various stimuli, including electric fields, temperature changes, or light itself [10-12].

1.1 Overview

This dissertation investigates **layered electromagnetic nanostructures**, a rapidly evolving field with transformative potential for photonics, sensing, quantum information processing, and telecommunication systems. These nanostructures possess a unique ability to manipulate

light at the nanoscale, paving the way for next-generation optical devices with superior performance.

Understanding these structures requires a foundation in the fundamental principles of electromagnetic wave propagation in layered media and the application of Maxwell's equations at the nanoscale. This theoretical framework, explored in detail throughout the dissertation, empowers the analysis of light-matter interactions within the structures. These interactions lead to fascinating phenomena like surface plasmon polaritons and enhanced light-matter interaction, holding promise for high-quality optical devices and efficient hot electron generation [13-17].

Following this foundation, the dissertation delves deeper by focusing on specific optical phenomena crucial for nanostructure design:

Surface plasmon theory: Explores the collective oscillation of electrons at the metal-dielectric interface, enabling light confinement and manipulation.

Fano resonances: Analyzes the interplay of constructive and destructive interference, leading to sharp spectral features with potential applications in ultrasensitive sensing.

Bound states in the continuum (BICs): Investigates localized light states within the continuum, offering opportunities for high-*Q* microcavities and sensors.

Rabi splitting: Examines the splitting of energy levels due to strong light-matter interaction, holding promise for quantum information processing.

Hot electron generation in plasmonic nanoelectrodes: Analyzes the generation of energetic electrons upon light absorption in plasmonic nanostructures, with applications in photocatalysis and photodetection.

This dissertation explores the mechanisms, applications, and ongoing research associated with various phenomena exhibited by layered electromagnetic nanostructures. These nanostructures hold immense potential for applications across diverse scientific and technological fields:

Sensing: Fano resonances enable the development of highly sensitive optical sensors due to their sharp spectral features.

Optical Communication and Lasers: Bound states in the continuum (BICs) offer exciting opportunities for the design of high-Q devices, critical for efficient light manipulation in optical communication and lasers.

Quantum Information Processing: Rabi splitting, a phenomenon arising from strong light-matter interaction, holds promise for the development of novel quantum technologies.

Photodetection and Photocatalysis: Hot electron generation in plasmonic nanoelectrodes finds applications in photodetection and photocatalysis.

The analysis leverages the **Finite Element Method** (FEM) with the frequency-domain solver within CST Studio Suite software. This powerful technique enables full-wave simulations for meticulous analysis of intricate optical responses in complex structures.

In conclusion, this dissertation presents a comprehensive exploration of the optical responses of layered electromagnetic nanostructures. By weaving together fundamental principles, advanced simulations, and in-depth analysis of key phenomena, it offers a valuable contribution to this exciting and rapidly evolving field.

1.2. Aims and objectives of the study

This dissertation presents a comprehensive investigation of the optical responses exhibited by layered electromagnetic nanostructures. These structures have garnered significant interest due

to their remarkable properties, which have revolutionized the fields of photonics and optics and led to numerous applications across diverse scientific and technological disciplines.

The primary objective of this research is to deepen our understanding of the light-matter interaction within layered electromagnetic nanostructures. This will be achieved by meticulously examining the intricate processes governing how these structures interact with light and the resulting effects. Phenomena such as reflection, transmission, and absorption of light by the nanostructures will be rigorously studied. Mathematical modeling and computational simulations will be employed to generate accurate predictions of these interactions.

The dissertation pursues several specific objectives. The initial step involves a comprehensive review of the existing literature related to the optical properties of layered electromagnetic nanostructures. This review will be instrumental in identifying potential areas for further exploration and knowledge gaps, ultimately enriching our understanding of the current research landscape in this field.

Building upon the foundation established by the literature review, a robust theoretical framework will be developed to explain the optical responses of these nanostructures. This framework will be anchored in Maxwell's equations and their corresponding boundary conditions, which form the bedrock of our understanding of electromagnetic wave behavior.

Next, the dissertation will develop mathematical models for accurately predicting the optical behavior of these nanostructures. These models will specifically focus on the reflection, transmission, and absorption properties of the structures. They will be designed with a degree

of generality to allow for their application to a broad range of layered structures and varying characteristics of incident light.

The developed mathematical models will be validated through computational simulations. These simulations will not only verify the models' accuracy but also provide valuable visualizations of the complex light-matter interactions taking place within the layered structures. These visualizations will be instrumental in understanding and interpreting these interactions.

The research will explore potential practical applications arising from the findings. A particular area of interest lies in the field of sensor development. Ultimately, the goal is to leverage the insights gained from this research to design novel devices or systems that capitalize on the unique optical properties of layered electromagnetic nanostructures.

Finally, the research findings will be disseminated to the wider scientific community through publication in peer-reviewed scientific journals and presentations at relevant conferences. This objective is rooted in the belief that scientific progress thrives on collaboration. It is hoped that this research will contribute to the collective understanding in this domain.

This dissertation extends beyond a purely academic exercise. It represents an ambitious effort to push the boundaries of knowledge in the realm of nano-optics and photonics. By shedding light on the fascinating world of layered electromagnetic nanostructures and their interaction with light, this research aspires to inspire and facilitate further technological innovation. Consequently, it aims to enrich our understanding of nano-optics and expand our capacity to harness its potential.

In conclusion, this dissertation presents a comprehensive investigation designed to enhance our understanding of the optical responses exhibited by layered electromagnetic nanostructures. The research objectives, encompassing a literature review, theoretical foundation, development of mathematical models, computational simulations, exploration of practical applications, and dissemination of results, all contribute to achieving this goal. The outcomes of this research are expected to contribute to the development of novel devices and systems that exploit the unique optical properties of these nanostructures.

1.3 References

[1] P. Yeh, “Optical Waves in Layered Media.” Wiley, 2008.

[2] D. K. Gramotnev and S. I. Bozhevolnyi, “Plasmonics beyond the diffraction limit, Nature Photonics4(2)”, 83-91 (2010).

[3] E. Yablonovitch, “Inhibited Spontaneous Emission in Solid-State Physics and Electronics”, Physical Review Letters 58 (20), 2059–2062 (1987).

[4] J. B. Pendry, “Negative Refraction Makes a Perfect Lens,” Physical Review Letters 85(18), 3966–3969 (2000).

[5] S. A. Maier, “Plasmonics: Fundamentals and Applications”. Springer, 2007.

[6] N. Yu and F. Capasso, “Flat optics with designer metasurfaces,” Nature Materials 13 (2), 139–150 (2014).

[7] P. Genevet, F. Capasso, F. Aieta, M. Khorasaninejad, and R. Devlin,” Recent advances in planar optics: from plasmonic to dielectric metasurfaces,” Optica 4(1), 139-152 (2018).

[8] Y. Yang, W. Wang, P. Moitra, I. I. Kravchencko, D. P. Briggs, and J. Valentine, "Dielectric meta-reflectarray for broadband linear polarization conversion and optical vortex generation," Nano Letters 14 (3), 1394–1399 (2014).

[9] S. Wang, P. C. Wu, V. C. Su, C. Y. Liao, C. W. Qiu, and D. P. Tsai, “A broadband achromatic metalens in the visible”, Nature Nanotechnology 13(3), 227–232 (2016).

[10] D. Shrekenhamer and W. J. Padilla, “Liquid crystal tunable metamaterial absorber,” Physical Review Letters 110 (17), 177403 (2013).

[11] M. Thangamuthu, T. V. Raziman, O. J. F. Martin, and J. Tang, "Review—Origin and Promotional Effects of Plasmonics in Photocatalysis," Journal of The Electrochemical Society 169 (5), 036512 (2022).

[12] D. K. Gramotnev and S. I. Bozhevolnyi, “Plasmonics beyond the diffraction limit,” Nature Photonics 4 (2), 83-91 (2010).

[13] J. Jin, “The Finite Element Method in Electromagnetics.” Wiley, 2002.

[14] A. E. Miroshnichenko, S. Flach, and Y. S. Kivshar, "Fano resonances in nanoscale structures,” Reviews of modern physics 82 (3), 2257 (2010).

[15] C. W. Hsu, B. Zhen, A. D. Stone, J. D. Joannopoulos, and M. Soljačić, “Bound states in the continuum,” Nature Reviews Materials1 (7), 1-13 (2016).

[16] P. Törmä and W. L. Barnes, "Strong coupling between surface plasmon polaritons and emitters: a review," Reports on Progress in Physics78(1), 013901 (2015).

[17] M. L. Brongersma, N. J. Halas, and P. Nordlander, “Plasmon-induced hot carrier science and technology," Nature nanotechnology 10(1), 25-34 (2015).

Chapter 2

Contents

2.0 Introduction

This chapter delves into the intricate interplay of light and layered nanostructures, a phenomenon critical for advancements in imaging, sensing, telecommunications, solar energy conversion, and numerous other fields. Unveiling these interactions is paramount for the development of next-generation technologies [1,2].

Section 2.1 lays the foundation by providing a historical overview of electromagnetic theory, with a particular focus on Maxwell's equations. These fundamental equations govern the behavior of electric and magnetic fields, forming the cornerstone of our understanding of the optical properties exhibited by layered nanostructures. This section highlights how Maxwell's equations, by unifying the laws of electricity and magnetism, revolutionized the exploration of light-matter interactions at the nanoscale.

Building upon this foundation, Section 2.2 explores the importance of the optical responses of layered nanostructures and introduces the Transfer Matrix Method (TMM). Derived from applying Maxwell's equations with appropriate boundary conditions, TMM serves as a testament to the power of these equations in analyzing and predicting light's behavior as it interacts with layered nanostructures [3,4]. This section emphasizes how TMM offers valuable insights into the complex optical phenomena displayed by these structures.

Section 2.3 leverages TMM to analyze the transmission and reflection of light through layered structures. This understanding empowers us to manipulate light effectively at the nanoscale, enabling the optimization of structures for specific applications. For instance, it can be used to enhance light absorption in solar cells or improve sensitivity in sensors [5,6,7].

Finally, Section 2.4 shifts our focus to surface plasmons, a phenomenon where light interacts with free electrons at the metal-dielectric interfaces within nanostructures. This interaction confines light to subwavelength dimensions, significantly enhancing light-matter interactions and opening exciting possibilities for nanophotonic device development [8,9].

This chapter embarks on a journey, traversing from the fundamental insights provided by Maxwell's equations and the historical evolution of electromagnetic theory to the cutting-edge applications in nanophotonics. By skillfully combining theoretical principles with advanced computational methods, we unlock innovative strategies to harness the potential of layered nanostructures, paving the way for groundbreaking technological advancements.

2.1 Historical background of electromagnetic waves and Maxwell's equations

Unraveling the mysteries of electromagnetic fields, a cornerstone of physics, has been a centuries-long pursuit. The journey began with simple observations and experiments, culminating in a more comprehensive understanding of the universe thanks to the pioneering work of scientists like James Clerk Maxwell. This development has had a profound impact on modern optics, the science of light, granting us the ability to manipulate and utilize light in various technologies [10].

The earliest documented understanding of electricity and magnetism can be traced back to ancient civilizations. The Greeks observed that rubbed amber attracted certain objects, while Chinese scholars documented the magnetic properties of lodestone, a naturally magnetized

mineral [11]. These fundamental observations laid the groundwork for the future development of electromagnetic field theory.

By the 17th century, scientists began a more rigorous investigation of these phenomena. William Gilbert's treatise, "De Magnete," detailed extensive experiments with magnetism, establishing a foundational understanding of the subject [12]. Building upon this work, Benjamin Franklin's mid-18th century experiments with electricity expanded our knowledge of this enigmatic force, contributing to the definition of key concepts like the conservation of electrical charge [13].

The 19th century witnessed significant progress in unifying the understanding of these forces. Michael Faraday discovered a profound connection between electricity and magnetism, paving the way for their eventual unification [14]. Andre-Marie Ampère's work further elaborated on this relationship, shedding light on the intricate interplay between electricity and magnetism [15].

James Clerk Maxwell's groundbreaking work in the 1860s marked a pivotal moment in the narrative. He formulated a set of equations, now known as Maxwell's equations, that elegantly unified the laws of electricity and magnetism into a single framework [16]. Notably, Maxwell further theorized that light itself was an electromagnetic wave. This groundbreaking discovery not only hinted at the existence of other types of electromagnetic waves but also revolutionized our understanding of light, ushering in the era of modern optics [16].

Maxwell's revelation that light is an electromagnetic wave laid the foundation for our understanding of its behavior and interaction with matter. This knowledge has been essential for the development of diverse optical technologies, ranging from simple lenses and mirrors to

sophisticated instruments like microscopes and telescopes, and even fiber optics for telecommunication.

Further advancements in the 20th century, particularly quantum mechanics and Einstein's theory of relativity, further refined our comprehension of light. Quantum mechanics introduced the concept of photons, the fundamental units of light, which led to revolutionary technologies like lasers and light-emitting diodes (LEDs) [16]. Einstein's theory of relativity expanded our understanding of light's motion and interaction with space and time, leading to a deeper grasp of phenomena like gravitational lensing, where light bends around massive objects [17].

James Clerk Maxwell, 1831-1879

Figure. 2.1: First to propose that light is an electromagnetic wave.

Maxwell's equations play a fundamental role in classical electrodynamics, optics, and the study of electric circuits. These equations represent an elegant unification of what were previously considered separate principles. They encompass Gauss's law for both electric and magnetic fields, Faraday's law of electromagnetic induction, and Ampère's law (incorporating Maxwell's insightful modifications).

The importance of these equations cannot be overstated, as they provide the foundation for comprehending a vast array of electromagnetic phenomena.

While Maxwell's equations originally describe the evolution of electric and magnetic fields over time, certain applications in optics and radio frequency engineering deal with fields exhibiting sinusoidal variations. These variations are termed time-harmonic or phasor fields, and working with the time-harmonic formulation of Maxwell's equations can be more efficient in such cases [18, 19].

Therefore, the time-harmonic form of Maxwell's equations is presented as follows:

1. Gauss's Law for Electricity: $\nabla \cdot \vec{E} = {}^{\rho}/_{\varepsilon_0}$ (2.1),

2. Gauss's Law for Magnetism: $\nabla \cdot \vec{H} = 0$ (2.2),

3. Faraday's Law: $\nabla \times \overrightarrow{E} = -i\omega\vec{B}$ (2.3),

4. Ampère-Maxwell's Law: $\nabla \times \vec{H} = \vec{J} + i\omega\vec{D}$ (2.4).

In these equations: ∇ (nabla) symbolizes a vector differential operator, $\vec{E}$ is the electric field vector, $\vec{H}$ stands for the magnetic field vector, $\vec{B}$ signifies the magnetic flux density vector, $\vec{D}$ represents the electric displacement field vector, ρ denotes the free electric charge density, $\vec{J}$ refers to the free current density vector, ε_0 corresponds to the permittivity of free space,

$\omega = 2\pi f$ is the angular frequency (f being the frequency of the electromagnetic wave), and 'i' is the imaginary unit.

The operators "•" and "×" signify the dot product and cross product, respectively.

In the context of Maxwell's equations, the electric field ($\vec{E}$) and the electric displacement field ($\vec{D}$), as well as the magnetic field ($\vec{H}$) and the magnetic flux density ($\vec{B}$), are related through the properties of the materials in which these fields exist.

The relationship between $\vec{E}$ and $\vec{D}$ is given by: $\vec{D} = \varepsilon\vec{E}$ (2.5).

Here, ε is the permittivity of the material. It is the measure of a material's ability to store electrical energy in an electric field. For vacuum, ε is denoted by ε_0 (the permittivity of free space), but for other materials, ε is given by $\varepsilon = \varepsilon_r\varepsilon_0$, where ε_r is the relative permittivity or dielectric constant of the material.

The relationship between $\vec{H}$ and $\vec{B}$ is given by: $\vec{B} = \mu\vec{H}$ (2.6).

Here, μ is the permeability of the material. It measures the ability of a material to establish an internal magnetic field in response to an applied magnetic field. For vacuum, μ is denoted by μ_0 (the permeability of free space), but for other materials, μ is given by $\mu = \mu_r\mu_0$, where μ_r is the relative permeability of the material.

It is important to emphasize that for materials, both permittivity (ε) and permeability (μ) are usually complex quantities. This means they are expressed as $\varepsilon = \varepsilon' - i\varepsilon''$, and $\mu = \mu' - i\mu''$, where ε' and μ' are the real parts, and ε'' and μ'' are the imaginary parts of permittivity and permeability, respectively.

Also, in both cases, these relations assume that the material is linear, isotropic, and homogeneous, meaning that the permittivity and permeability are constant throughout the material and the same in all directions.

If these conditions are not met, ε and μ can become tensors, and the relationship between $\vec{E}$ and $\vec{D}$ or $\vec{H}$ and $\vec{B}$ can become more complex. Thus, in anisotropic materials, the relationship between the electric field vector ($\vec{E}$), electric displacement field vector ($\vec{D}$), and permittivity (ε) is of fundamental importance. Anisotropic materials are those whose properties vary with direction due to the underlying crystal structure, molecular alignment, or microstructural organization. In such materials, the permittivity ($\bar{\bar{\varepsilon}}$) becomes a tensor (3x3 matrix) instead of a scalar as in isotropic materials. The permittivity tensor, ($\bar{\bar{\varepsilon}}$) is represented as:

$$\bar{\bar{\varepsilon}} = \begin{pmatrix} \varepsilon_{xx} & \varepsilon_{xy} & \varepsilon_{xz} \\ \varepsilon_{yx} & \varepsilon_{yy} & \varepsilon_{yz} \\ \varepsilon_{zx} & \varepsilon_{zy} & \varepsilon_{zz} \end{pmatrix}$$

The relationship between $\vec{E}$ and $\vec{D}$ in anisotropic materials is given by the equation $\vec{D} = \bar{\bar{\varepsilon}}\vec{E}$.

Here, $\vec{D}$ is a column vector representing the electric displacement field, $\vec{E}$ is a column vector representing the electric field. In component form, this equation can be expressed as:

$$\begin{pmatrix} D_x \\ D_y \\ D_z \end{pmatrix} = \begin{pmatrix} \varepsilon_{xx} & \varepsilon_{xy} & \varepsilon_{xz} \\ \varepsilon_{yx} & \varepsilon_{yy} & \varepsilon_{yz} \\ \varepsilon_{zx} & \varepsilon_{zy} & \varepsilon_{zz} \end{pmatrix} \cdot \begin{pmatrix} E_x \\ E_y \\ E_z \end{pmatrix}$$

Where:

D_x, D_y, D_z are the components of the electric displacement field vector $\vec{D}$ along the *x*, *y*, and *z* directions, respectively.

E_x, E_y, E_z are the components of the electric field vector $\vec{E}$ along the *x*, *y*, and *z*- directions, respectively.

The permittivity tensor is symmetric, meaning $\varepsilon_{ij} = \varepsilon_{ji}$, and accounts for the material's anisotropic behavior. The diagonal elements (ε_{xx}, ε_{yy}, ε_{zz}) represent the permittivity along the principal axes (x, y, z), while the off-diagonal elements (ε_{xy}, ε_{xz}, ε_{yx}, ε_{yz}, ε_{zx}, ε_{zy}) represent the coupling between different directions.

An anisotropic permittivity tensor characterizes materials that exhibit distinct electrical properties along different axes. This anisotropy leads to a directional dependence in the material's response to an electric field. To fully capture this behavior, the permittivity tensor can take on different values depending on the direction within the material [21, 22].

Anisotropic materials play a crucial role in various applications, including the design of optical devices, anisotropic metamaterials, and electronic components. Photonic crystals, negative-index metamaterials (NIMs), plasmonic nanostructures, optical metasurfaces, and hybrid metasurfaces are all examples where anisotropic materials contribute to achieving unique and tailored functionalities [23-25].

In conclusion, the historical journey from simple ancient observations to our current sophisticated understanding of electromagnetism exemplifies the power of human curiosity and scientific exploration. This journey has been instrumental in revolutionizing optics, deepening our knowledge of light, and enabling a multitude of technologies that shape our world. As the field of electromagnetism continues to evolve, it holds the promise of further illuminating the universe and opening new avenues for technological progress.

2.2. Overview and significance of optical responses of layered electromagnetic nanostructures

The discovery of surface plasmon polaritons (SPPs) in the mid-20th century, collective oscillations of free electrons at a metal surface, laid the groundwork for the field of plasmonics and, by extension, layered nanostructures. This discovery fueled deeper exploration into how light interacts with metals, particularly at interfaces between different media [26].

By the late 20th century, advancements in nanotechnology and the ability to fabricate layered structures with nanoscale precision opened doors to new research avenues. Layered electromagnetic nanostructures are typically constructed by stacking materials with varying refractive indices or electromagnetic properties. By harnessing interference effects between these layers, structures can be meticulously designed to exhibit a desired response to incident light. Furthermore, by tailoring the thickness, material properties of each layer, and the total number of layers, the optical response can be optimized for specific applications, ranging from highly reflective mirrors and antireflective coatings to efficient light-emitting devices [27, 28].

The field of nanotechnology has witnessed a surge of interest in the optical responses of layered electromagnetic nanostructures due to their potential for transformative applications in photonics, biomedical imaging, and beyond. This profound interest stems from their unique ability to manipulate light-matter interactions at subwavelength scales, leading to novel optical phenomena and unparalleled device functionalities [29-31].

The optical response of a material essentially describes its interaction with incident light. It is typically characterized by processes such as reflection, transmission, absorption, and

scattering. Nanostructures stand out because their optical responses can be precisely controlled by manipulating their size, shape, composition, and arrangement. Layered structures like thin films, quantum wells, metamaterials, and photonic crystals are prime examples of layered electromagnetic nanostructures, exhibiting resonant behaviors such as localized surface plasmon resonance (LSPR) and Fabry-Pérot resonances. These phenomena enable strong light confinement and enhanced light-matter interactions [32, 33].

One of the most captivating aspects of layered nanostructures is the ability to manipulate light at scales smaller than its wavelength. By meticulously engineering these structures, it becomes possible to control the phase, amplitude, and polarization of light in ways that bulk materials cannot achieve. For instance, metasurfaces, essentially two-dimensional metamaterials, can be spatially engineered to manipulate an incident light wave almost arbitrarily. This opens exciting possibilities for the development of flat optics, holography, and highly integrated photonic devices [34-36].

The unique optical properties of layered nanostructures have yielded diverse and impactful applications across various fields.

Energy Sector: Multilayered nanostructures have been implemented to enhance light absorption in solar cells, leading to improved energy conversion efficiencies.

Electronics: The design of high-speed transistors and lasers has been significantly influenced by quantum wells, a type of layered nanostructure.

Data Storage: Layered nanostructures play a role in the development of high-density optical storage media, such as Blu-ray discs.

Biomedicine: Nanostructured materials are increasingly employed for in vivo imaging, biosensing, and therapeutic applications. For instance, plasmonic nanoparticles can enhance the signal of Raman scattering (Surface-Enhanced Raman Scattering, SERS), offering a powerful tool for the detection and identification of molecules in biomedical diagnostics [37-40].

2.3 Theoretical foundations of the transfer-matrix method (TMM)

Consider a system as illustrated in Fig. 2.2, consisting of a single layer film of thickness t and refractive index n_1, sandwiched between a covering layer with refractive index n_0 and a substrate with refractive index n_s. Light is incident from one side of the system. While the system exhibits homogeneity along the x and y-directions, it has variations along the z-direction, perpendicular to the layers.

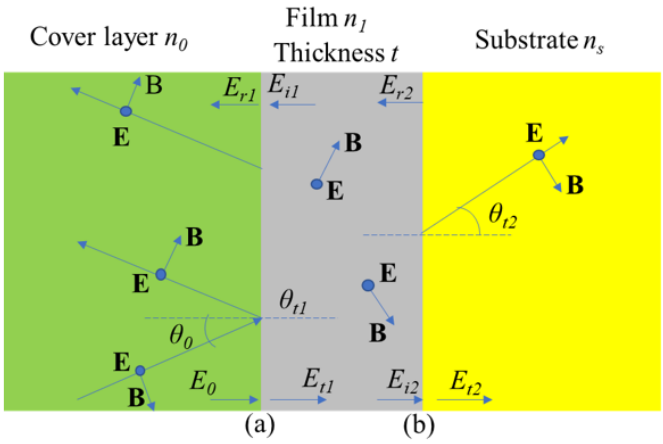

Figure.2.2. Single layer film of thickness t and index refraction n_1 on a substrate of index n_s placed in a medium with refractive index of n_0.

Understanding the optical responses generated by such a system is facilitated by methods grounded in theoretical principles. Maxwell's equations, along with their corresponding

boundary conditions, can be applied to analyze the fields within these layers. According to Maxwell's equations, the electric field is continuous across the boundary between two media. Therefore, if the electric field is known at the beginning of a layer, the field at the end can be derived using a well-defined mathematical operation.

Several theoretical approaches have been developed to gain a comprehensive understanding of the optical responses arising from these systems. The Transfer-Matrix Method (TMM) stands out for its exceptional efficacy. The TMM has been specifically adapted to calculate the transmittance (T) and reflectance (R) associated with layered structures like the one depicted in Fig. 2.2. As we progress through this chapter, we will delve into the application of TMM to compute these transmittances and reflectances for our system structure. The system matrix is essentially the product of individual layer matrices.

Therefore, the TMM proves to be a powerful tool for designing structures like anti-reflective coatings and dielectric mirrors. The conceptual analysis and subsequent theory of the TMM follow the approach outlined by Pedrotti, and Born & Wolf [36, 37].

Figure 2.2 illustrates a one-layer film, along with the components of the associated electric and magnetic fields of the incident, reflected, and transmitted waves.

We assume a homogeneous, isotropic film with refractive index n deposited on a substrate with refractive index ns. The structure is then placed in a medium with an index of refraction no. A beam of light is incident on the first interface (a), where it undergoes partial reflection. Part of the beam may also experience total internal reflection within the film, while another portion is transmitted at the second interface (b).

According to Maxwell's equations, and by applying boundary conditions at the interfaces, the tangential components of the resultant electric and magnetic fields are continuous across the interface as shown below in equations (2.7) and (2.8).

$$\begin{aligned} E_a &= E_o + E_{r1} = E_{t1} + E_{i1} \\ E_b &= E_{i2} + E_{r2} = E_{t2} \end{aligned} \tag{2.7}$$

$$\begin{aligned} B_a &= B_o \cos\theta_o - B_{r1} \cos\theta_o = B_{t1} \cos\theta_{t1} - B_{i1} \cos\theta_{t1} \\ B_b &= B_{i2} \cos\theta_{t1} - B_{r2} \cos\theta_{t1} = B_{t2} \cos\theta_{t2} \end{aligned} \tag{2.8}$$

In this context, the magnetic and electric fields are interconnected through the equation:

$$\vec{B} = n\sqrt{\varepsilon_0 \mu_0}\vec{E} \tag{2.9}.$$

with the magnetic field possessing both tangential and perpendicular components. As such, utilizing equation (2.9) allows us to recast equation (2.8) in the following form:

$$\begin{aligned} B_a &= \left(n_o\sqrt{\varepsilon_o\mu_o}\cos\theta_o\right)\left(E_o - E_{r1}\right) = \left(n_1\sqrt{\varepsilon_o\mu_o}\cos\theta_{t1}\right)\left(E_{t1} - E_{i1}\right) = \gamma_o\left(E_o - E_{r1}\right) = \gamma_1\left(E_{t1} - E_{i1}\right) \\ B_b &= \left(n_1\sqrt{\varepsilon_o\mu_o}\cos\theta_{t1}\right)\left(E_{i2} - E_{r2}\right) = \left(n_s\sqrt{\varepsilon_o\mu_o}\cos\theta_{t2}\right)\left(E_{t2}\right) = \gamma_1\left(E_{i2} - E_{r2}\right) = \gamma_s\left(E_{t2}\right) \end{aligned}$$

(2.10)

Here, we denote, $\gamma_o \equiv n_o\sqrt{\varepsilon_o\mu_o}\cos\theta_o$, $\gamma_1 \equiv n_1\sqrt{\varepsilon_o\mu_o}\cos\theta_{t1}$ and $\gamma_s \equiv n_s\sqrt{\varepsilon_o\mu_o}\cos\theta_{t2}$. The phase difference δ between E_{i2} and E_{t1} is given by $\delta = k_o\Delta = \left(2\pi/\lambda_o\right)n_1 t\cos\theta_{t2}$. This enables us to express the electric fields as $E_{i2} = E_{t1}e^{-i\delta}$ and $E_{i1} = E_{r2}e^{-i\delta}$ respectively. Thus, given the boundary conditions, we can formulate the following:

$$E_b = E_{t1}e^{-i\delta} + E_{i1}e^{i\delta} = E_{t2}$$
$$B_b = \gamma_1\left(E_{t1}e^{-i\delta} - E_{i1}e^{i\delta}\right) = \gamma_s E_{t2} \qquad (2.11).$$

By determining E_{t1} and E_{i1} in relation to E_b and B_b, we consequently obtain the following expression:

$$E_{t1} = \left(\frac{\gamma_1 E_b + B_b}{2\gamma_1}\right)e^{i\delta}$$
$$E_{i1} = \left(\frac{\gamma_1 E_b - B_b}{2\gamma_1}\right)e^{-i\delta} \qquad (2.12).$$

Next, we incorporate equation (2.12) into equations (2.7) and (2.8), yielding the subsequent result:

$$E_a = E_b\cos\delta + B_b\left(\frac{i\sin\delta}{\gamma_1}\right)$$
$$B_a = E_b\left(i\gamma_1\sin\delta\right) + B_b\cos\delta \qquad (2.13).$$

We can transpose equation (2.14) into a matrix form, connecting the field components at the initial boundary to those at the subsequent one. Here, E_1 and B_1 represent the electric and magnetic fields within the film respectively, as depicted in Equation (8) that follows.

$$\begin{pmatrix} E_a \\ B_a \end{pmatrix} = \begin{pmatrix} \cos\delta & \frac{i\sin\delta}{\gamma_1} \\ i\gamma_1 & \cos\delta \end{pmatrix}\begin{pmatrix} E_1 \\ B_1 \end{pmatrix} = M_1\begin{pmatrix} E_1 \\ B_1 \end{pmatrix} \qquad (2.14),$$

The matrix M_1 represents the transfer matrix specific to the film. In a multi-layer structure system, each layer boasts its unique transfer matrix. Thus, in a system composed of *N* layers, each layer, denoted as *j*, possesses a transfer matrix M_j, with *j* increasing in the direction of

propagation. In this context, the stack layers align perpendicularly to the propagation direction. This allows us to express the entire system's transfer matrix as follows:

$$M_s = M_1 \cdot M_2 \cdots\cdots M_N \qquad (2.15).$$

2.4 Transfer matrix method (TMM) analysis of multilayer Structures

Figure 2.3 depicts a schematic representation of the Transfer Matrix Method (TMM) applied to a multilayer structure. Each layer (represented by distinct colors) is characterized by a unique transmission matrix (T_0, T_1, and T_s), encapsulating its optical properties and propagation characteristics along the *z*-direction (assumed to be homogeneous in the *x* and *y* directions). Light incident from region I interacts with each layer as it propagates, and these interactions are mathematically described by the corresponding transmission matrices. The total transmission through the entire structure to region II is efficiently calculated by the product $T_{total} = Ts \cdot T_1 \cdot T_0$, accounting for the cumulative effect of all layers.

TMM provides a powerful tool for analyzing light propagation through complex multilayer structures. It allows researchers to systematically and efficiently assess various optical phenomena, facilitating the design and optimization of diverse photonic devices and systems. By utilizing TMM, researchers can gain crucial insights into the intricate interplay between light and individual layers within a multilayer structure. This understanding underpins advancements in nanophononics research and unlocks the potential of layered electromagnetic nanostructures for applications such as imaging, sensing, quantum information processing, directional scattering, and enhanced solar energy conversion.

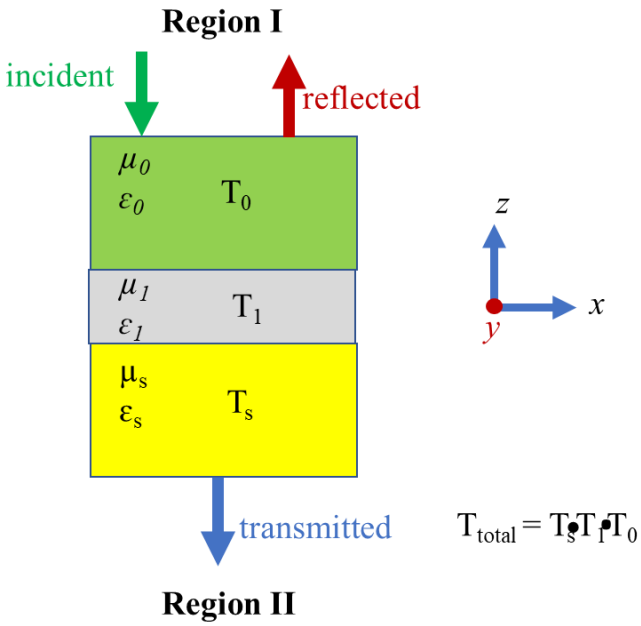

Figure.2.3 Concept of transfer matrices method (TMM) for a multilayered structure.

We can represent equation (2.15) in a more compact manner as:

$$M_s = \prod_{i=1}^{N} M_i \qquad (2.16).$$

By enforcing the boundary conditions at the interfaces within the multi-layer system, we can also write the transfer matrix in the following manner:

$$\begin{pmatrix} E_o + E_{r1} \\ \gamma_o \left(E_o - E_{r1}\right) \end{pmatrix} = \begin{pmatrix} m_{11} & m_{12} \\ m_{21} & m_{22} \end{pmatrix} \begin{pmatrix} E_{t2} \\ \gamma_s E_{t2} \end{pmatrix} \qquad (2.17).$$

Drawing from equation (2.18), we can derive the reflection and transmission coefficients as $r = {}^{E_{r1}}/_{E_0}$ and $t = {}^{E_{t2}}/_{E_0}$ respectively. These two parameters can also be described in relation to the transfer matrix elements and other variables associated with the transfer matrix as follows:

$$r = \frac{\gamma_o m_{11} + \gamma_o \gamma_s m_{12} - m_{21} - \gamma_s m_{22}}{\gamma_o m_{11} + \gamma_o \gamma_s m_{12} + m_{21} + \gamma_s m_{22}} \qquad (2.18),$$

$$t = \frac{2\gamma_o}{\gamma_o m_{11} + \gamma_o \gamma_s m_{12} + m_{21} + \gamma_s m_{22}} \qquad (2.19).$$

Equations (2.18) and (2.19) provide a universally applicable method for calculating reflection and transmission coefficients across any multi-layered structures. In addition, these equations also enable us to ascertain the reflectance and transmittance values from $R = |r|^2$ and $T = |t|^2$, correspondingly. Therefore, when designing *N* alternating layers featuring low (n_L) and high (n_L) refractive indices, we can derive the transfer matrix as follows:

$$M_s = \left(M_H M_L\right)^N = \left(\begin{pmatrix} \cos\delta(H) & \frac{i\sin\delta(H)}{\gamma_H} \\ i\gamma_H \sin\delta(H) & \cos\delta(H) \end{pmatrix} \begin{pmatrix} \cos\delta(L) & \frac{i\sin\delta(L)}{\gamma_L} \\ i\gamma_L \sin\delta(L) & \cos\delta(L) \end{pmatrix} \right)^N \qquad (2.20).$$

2.5 Modeling multilayer structures with the transfer matrix method (TMM)

This section leverages the transfer matrix derived in Section 2.2 (Equation 2.20) to calculate the transmittance and reflectance of various multilayer nanostructures. For simplicity, we will focus on an *N*-periodic stack system, as depicted in Fig. 2.4. To facilitate calculations, we define the we define the optical thickness as one quarter of the wavelength, which is typically denoted as $n_H L_H = n_L L_L = \lambda_0/4$, where λ_0 represents the chosen reference operating wavelength.

Additionally, we assume the system is composed of non-magnetic materials, resulting in a layered stack with alternating refractive indices, $n_1 = \sqrt{\varepsilon_1 \mu_1} = \sqrt{\varepsilon_1}$ and $n_2 = \sqrt{\varepsilon_2 \mu_2} = \sqrt{\varepsilon_2}$,

forming layers with thicknesses *a* and *b*, respectively. The refractive indices of the incident and transmitted media are denoted as n_0 and n_s, respectively.

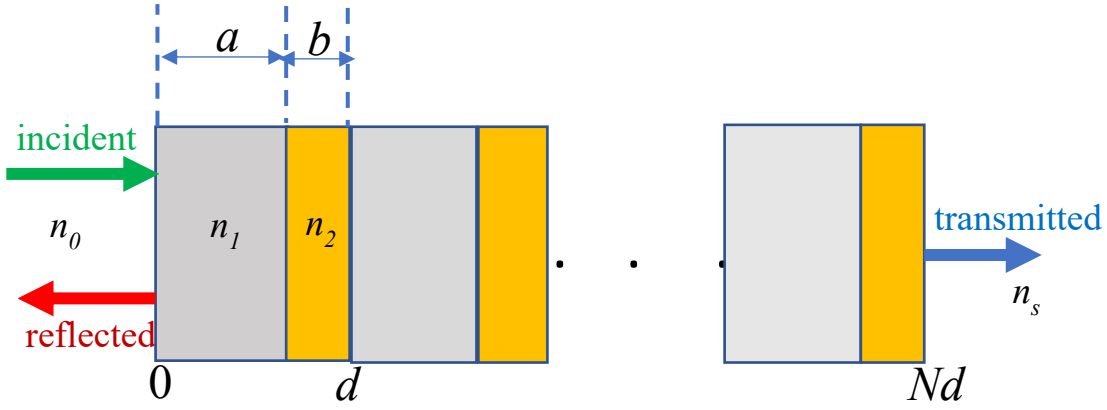

Figure.2.4. *N*-period stack consisting of two layers with thicknesses *a* and *b* and constant real indices of refraction n_1 and n_2,

A quarter-wave stack is characterized by the equation $n_1 a = n_2 b = \lambda_0/4 = \pi c/2\omega_0$, where ω_0 is the frequency at the middle of the band gap, and *c* is the speed of light in vacuum.

The Transfer Matrix Method (TMM) was employed to simulate a multilayer structure composed of alternating high and low refractive index materials. Silicon nitride (n_1 =1.9) and silicon dioxide (n_2 = 1.46) were chosen for the high and low index layers, respectively. Air (n_0 = 1) served as the incident medium, and the substrate was silicon (Si) with a refractive index of n_s = 3.48. The design wavelength ($\lambda_0 = 1.55\mu m$) was defined, and the transmittance and reflectance were calculated for structures with *N* = 1, 2, 6, 8, and 10 bilayers. Figures 2.5, 2.6, and 2.7 depict the reflectance and transmittance spectra as functions of frequency (ω), normalized by the variable ω/ω_0, for all *N* values.

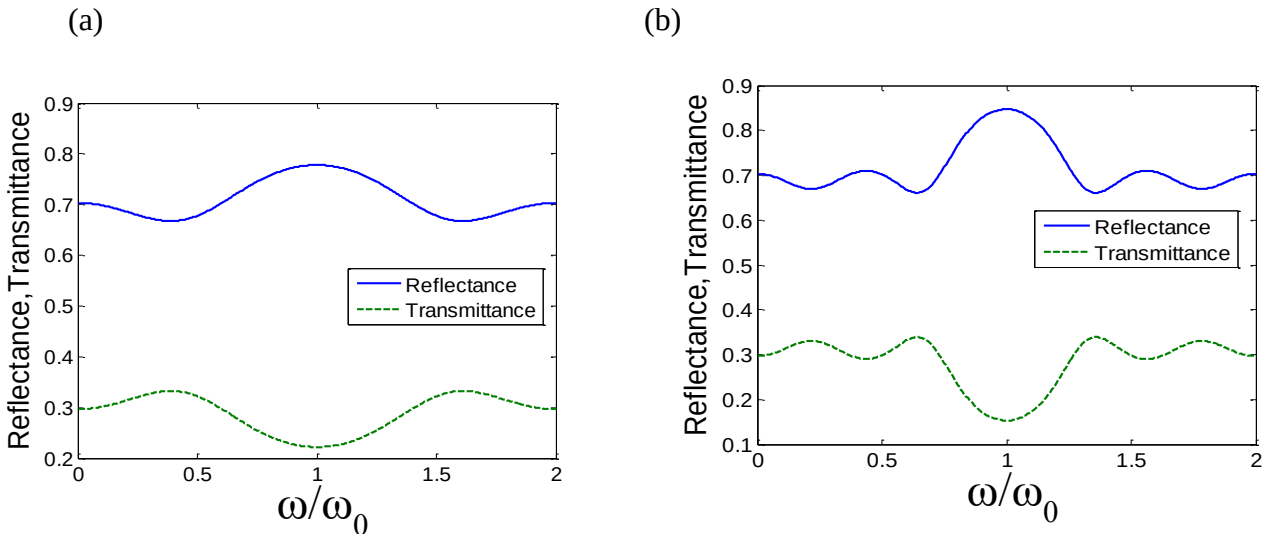

Figure. 2.5 Reflectance and transmittance for the multi-layer structure. (a) displays the scenario for N=1, while panel (b) illustrates the case for N=2.

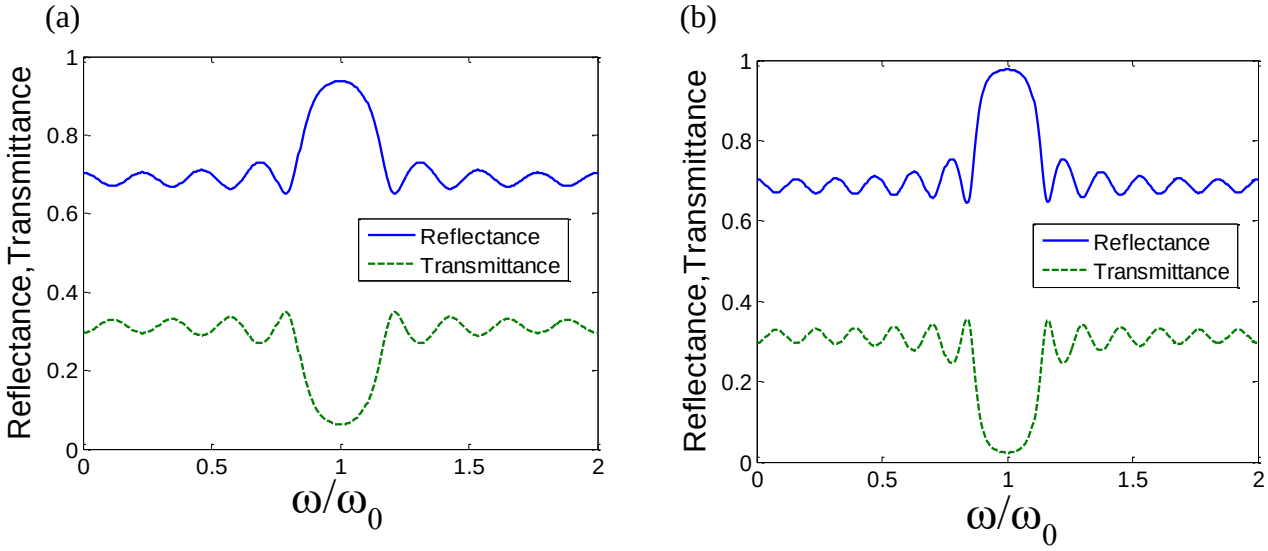

Fig. 2.6. Reflectance and transmittance for the multi-layer structure. (a) displays the scenario for N = 4, (b) illustrates the case for N = 6.

(a) (b)

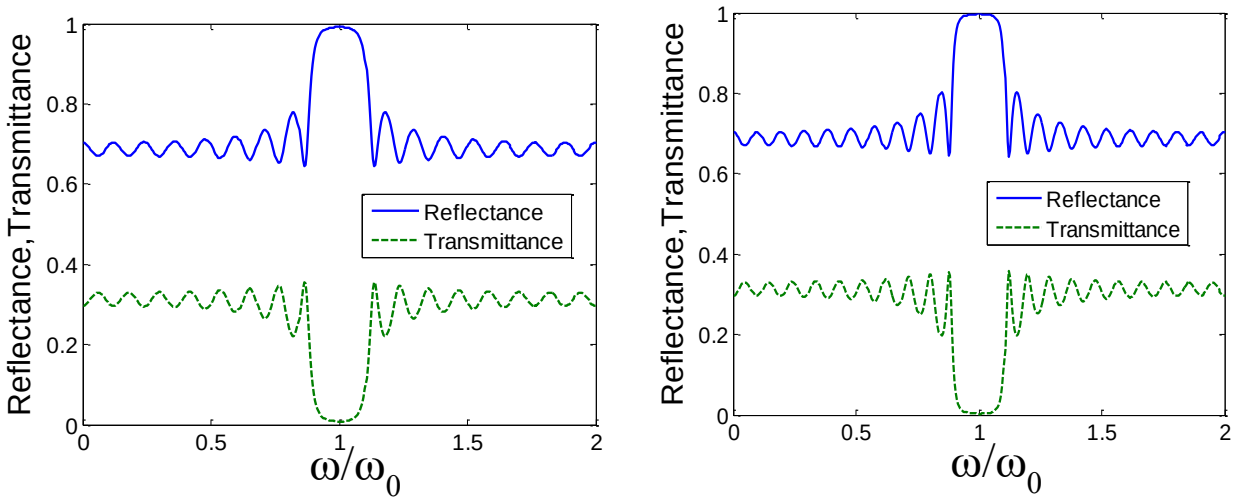

Figure. 2.7. Reflectance and transmittance for the multi-layer structure. (a) displays the scenario for N = 8, (b) illustrates the case for N = 10.

To investigate the influence of structural defects, we further analyzed the reflection and transmission responses by introducing a controlled imperfection. Specifically, the thickness of one silicon nitride layer was extended to a half-wavelength, while maintaining the silicon dioxide layer thickness at a quarter-wavelength. The resulting spectral calculations for reflectance and transmittance are presented in Figs. 2.8, 2.9, and 2.10.

(a) (b)

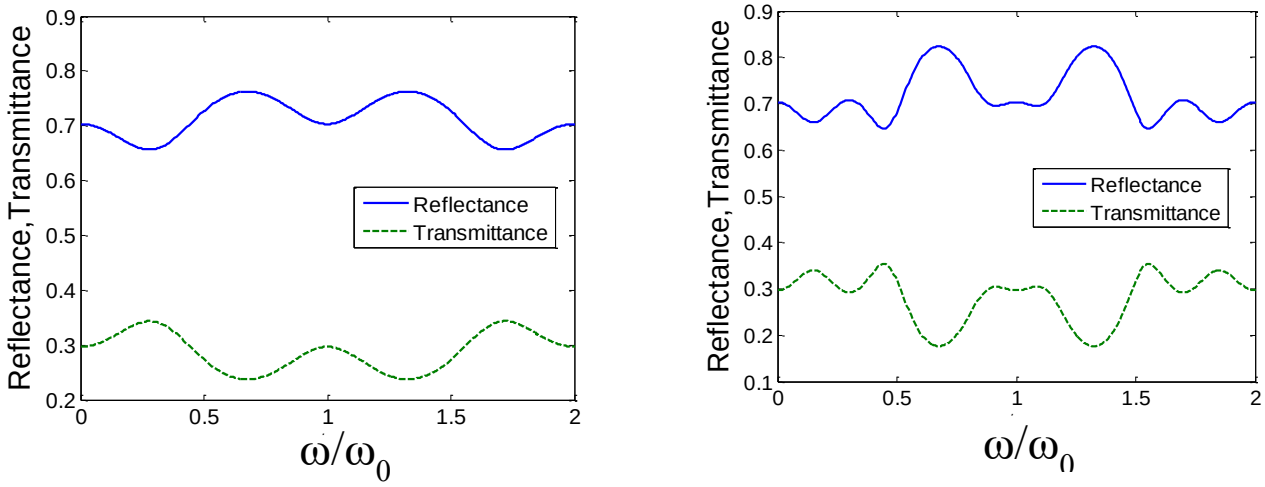

Figure 2.8. Reflectance and transmittance responses characteristic to the multilayered structure. (a) condition when N =1, (b) demonstrates the scenario for N = 2.

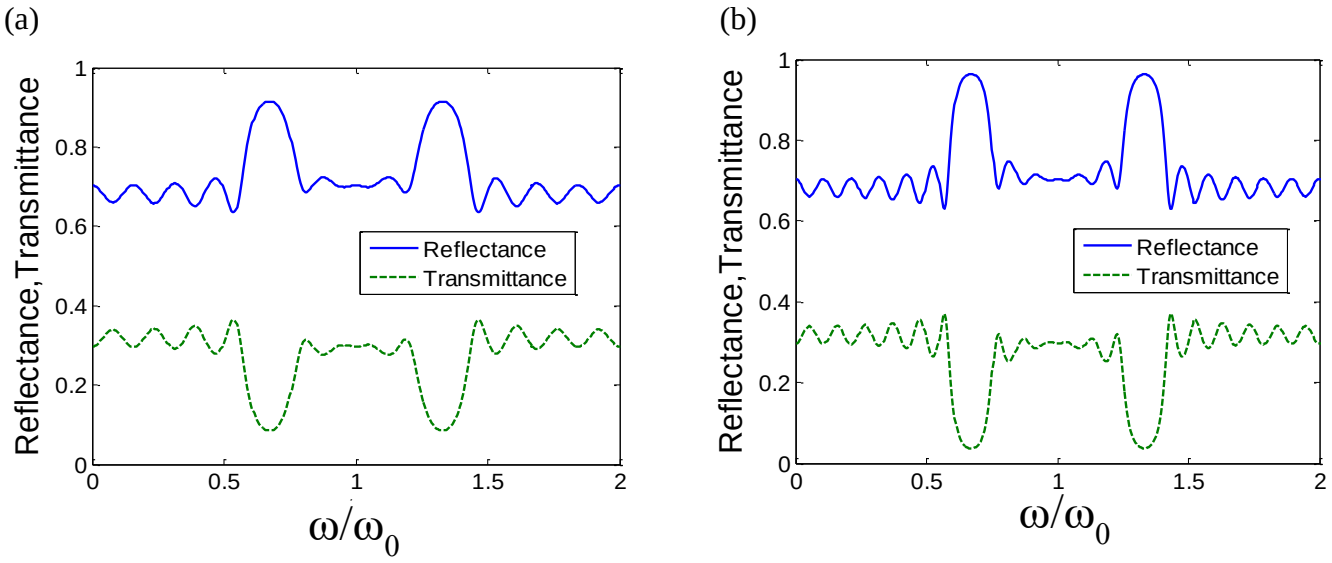

Figure 2.9. Reflectance and transmittance responses characteristic of the multilayered structure. (a) condition when N = 4, (b) demonstrates the scenario for N = 6

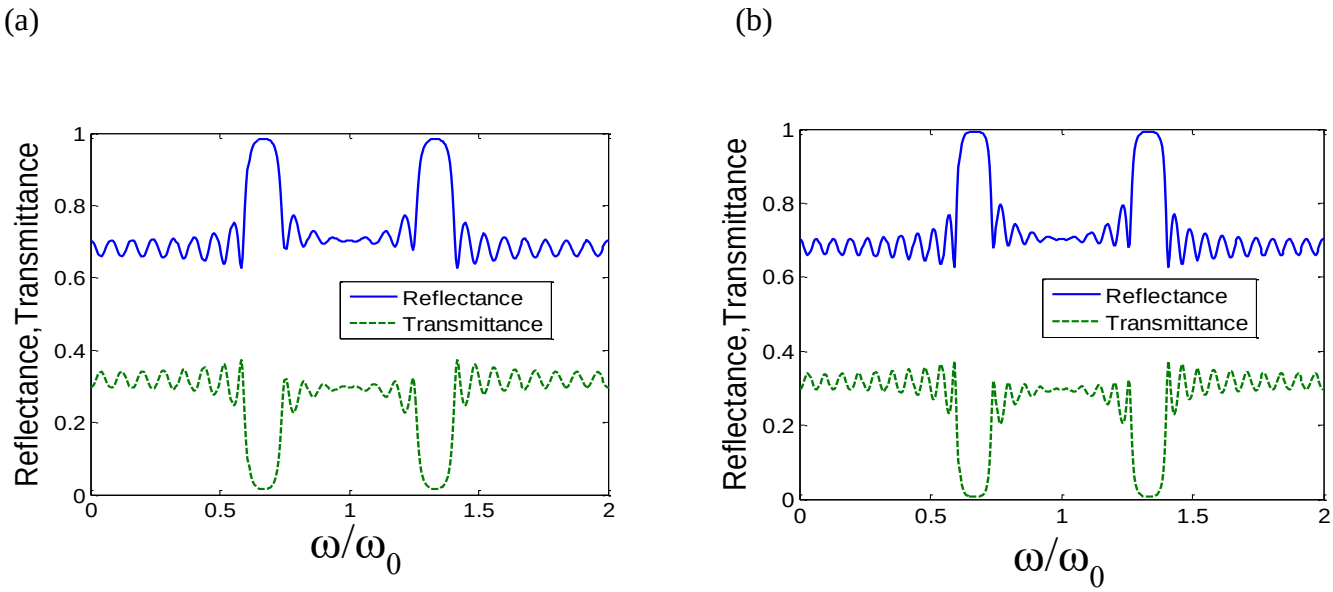

Figure 2.10. Reflectance and transmittance responses characteristic to the multilayered structure. (a) condition when N = 8, (b) demonstrates the scenario for N = 10.

To explore the effect of a frequency-dependent permittivity, we further analyze the system's transmittance after replacing a single layer with a material exhibiting such behavior. For the case of simple metals lacking a damping rate, the metal permittivity can be simplified using Drude's model, expressed by the equation:

$$\varepsilon(\omega) = 1 - \omega_p^2/\omega^2.$$

Where ε(ω) is the frequency-dependent permittivity, ω_p is the plasma frequency ω is the angular frequency. This substitution allows us to investigate how the system's optical response changes when a layer exhibits a permittivity that varies with frequency.

Figure 2.11 illustrates the calculated transmittance spectrum after substituting the second layer of the structure with gold. The simulations were performed for terahertz (*THz*) frequencies, with specific values of $\omega_p = 4350\pi THz$, $\lambda_0 = 1.55\ \mu m$, and N =5. The refractive indices of the substrate (n_s = 3.48), incident medium (n_0 = 1), and remaining dielectric layers n_1= 1, and $n_2 = \sqrt{\varepsilon(\omega)}$. This analysis demonstrates how incorporating a metallic layer with a frequency-dependent permittivity (as modeled by Drude's model for gold) affects the overall optical response of the multilayer structure.

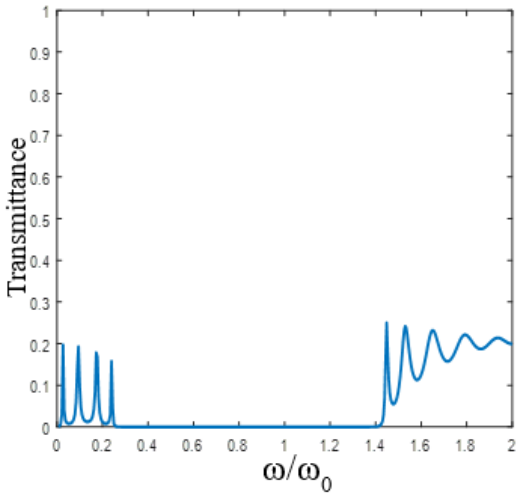

Figure. 2.11. Transmittance plot for the multilayered structure with N=5 layers, $n_1 = 1$, $n_2 = \sqrt{\varepsilon(\omega)}$.

The Transfer Matrix Method (TMM) is a powerful and versatile computational tool for analyzing the optical responses of multilayered nanostructures. It can handle systems with any number of layers, enabling accurate predictions of light-matter interactions. Understanding these interactions is critical for designing nanostructures with tailored optical properties.

TMM facilitates the prediction and manipulation of resonant modes crucial in nanophotonics, such as surface plasmons and Fabry-Pérot resonances. These resonances in layered nanostructures can lead to fascinating phenomena like Fano resonances, bound states in the continuum, and strong coupling. By adjusting structural parameters, scientists can modulate these resonances, opening doors for applications in sensing, optical switching, filtering, and diverse photonic devices.

The study of optical responses in layered nanostructures holds growing importance within photonics. Initially, scientists developed and refined mathematical models and theories to

comprehend these complex interactions, laying a strong foundation. As these tools became more sophisticated, our understanding deepened, propelling the field forward.

Understanding these optical responses has vast and diverse practical applications. Their potential impact spans telecommunications, data storage, medical imaging, quantum information processing, and solar energy capture. This breadth ensures the field remains a research focal point, driving continuous innovation.

The study and comprehension of optical responses in layered electromagnetic nanostructures are of paramount importance. The Transfer Matrix Method serves as a critical tool for accurately calculating these responses and predicting light-matter interactions. This knowledge unlocks a treasure trove of possibilities for technological advancements across various fields, pushing the boundaries of information technology, energy production, healthcare, and beyond. As our ability to design and control layered nanostructures evolves, their applications will continue to expand, further fueling progress and innovation.

2.6 Surface plasmons

The early 20th century witnessed the first experimental discovery of surface plasmons, attributed to R. W. Wood. In 1902, Wood observed anomalies in his measurements of wavelength and angular dependence of polychromatic light reflectivities from metallic diffraction gratings. One anomaly involved a rapid change in light intensity at specific narrow wavelength ranges depending on the grating periodicity or wavelengths at certain fixed angles of incidence, rather than the metal properties themselves [38].

Lord Rayleigh proposed an explanation for this anomaly, suggesting it occurred at wavelengths where a diffracted wave appeared or vanished, giving rise to the term "Rayleigh anomaly" [39].

Wood observed another anomaly: a decrease in light intensity by the gratings, marked by a dark minimum and a bright maximum in the diffracted light spectrum. The spectral positions of these bands depended on the dielectric functions of the metals used in the gratings. This phenomenon was later attributed by Fano (1941) to the excitation of electromagnetic surface waves on the surface of the periodic metallic diffraction grating [40].

Numerous researchers have made significant contributions to the development of surface plasmon research. For instance, Ritchie's 1957 work on collective excitations of surface oscillations at metallic film boundaries led to the theoretical derivation of the dispersion relations of surface plasmon polaritons (SPPs) in thin metallic films. These findings were later confirmed experimentally by Powell and Swan [41, 42].

In 1958, Thurbadar observed a substantial decrease in the reflection spectrum while measuring light reflectivity from thin metallic films on a substrate. However, he did not attribute this effect to surface plasmon excitation. Ten years later, Otto explained Thurbadar's results, revealing that the significant reduction in reflectivity stemmed from the excitation of surface plasmons using a method known as attenuated total reflection (ATR) [43].

Around the same time, Kretschmann and Raether independently reported the excitation of surface plasmons using the ATR method in a different configuration. The ATR method has since become a vital tool for optically exciting surface plasmons at the interface between metals and dielectrics [44, 45].

Surface plasmons are collective oscillations of free electrons confined at the interface between a metal and a dielectric nanostructure. These confined electron oscillations can trigger corresponding electromagnetic field oscillations at the interface. This intricate interplay between electromagnetic wave oscillations and the motion of charges is referred to as surface plasmon polaritons (SPPs). A localized surface plasmon (LSP) is a specific type of surface plasmon that arises when the collective electron oscillations are confined within a metallic nanoparticle, particularly when the particle size is comparable to or smaller than the wavelength of light used for excitation. This confinement effect leads to unique properties of LSPs, distinct from those of propagating surface plasmons at a metal-dielectric interface [46,47].

This subsection explores the theory of bulk and surface plasmon-polaritons. We will first derive the dielectric function for bulk plasmon-polaritons using the Drude model's assumptions to understand their dispersion relation. Then, we will examine the conditions necessary for the existence of surface plasmon-polaritons at the metal-dielectric interface and derive their dispersion relation. Finally, we will demonstrate how to utilize the derived dispersion relation equations to calculate the frequency and wavelength of surface plasmon-polaritons, providing insights into their fundamental properties and behaviors.

2.6.1Theoretical analysis of surface plasmons

Our investigation will delve into the metal's dielectric response, which is intimately linked to its electron density (n).

We start our discussion by considering the effects of free electrons (no interband transitions) and formulate the equation of motion for an oscillating external field as:

$$\boldsymbol{E}(t) = \boldsymbol{E_0}\exp(-i\omega t) \qquad (2.21).$$

In its time-varying form, this equation becomes:

$$m\frac{d^2r}{dt^2} + m\gamma\frac{dr}{dt} = -e\boldsymbol{E_0}\exp(-i\omega t) \qquad (2.22).$$

Assuming a specific solution to equation (2.22), we can write

$$\boldsymbol{r}(t) = \boldsymbol{E_0}\exp(-\omega t)\Big/ m(\omega^2 + i\gamma\omega) \qquad (2.23).$$

Here, the complex amplitude accounts for any phase shift between the driving field and the medium's response.

The polarization $\boldsymbol{P}$ resulting from electron displacement can then be computed using:

$$\boldsymbol{P} = -ne\boldsymbol{r} \qquad (2.24).$$

Substituting Equation 2.1.3 into Equation 2.1.4, the polarization transforms to:

$$\boldsymbol{P} = -ne^2\boldsymbol{E}\Big/ m(\omega^2 + i\gamma\omega) \qquad (2.25).$$

In the case of a linear, isotropic, and nonmagnetic medium, we define the constitutive relation as:

$$\boldsymbol{D} = \varepsilon_0 \varepsilon \boldsymbol{E} \qquad (2.26).$$

In this context, $\boldsymbol{D}$ denotes the electric displacement, $\boldsymbol{E}$ represents the electric field, ε_0 refers to the permittivity of free space (valued at 8.854 x 10^{-12} F/m), and ε indicates the dielectric constant or relative permittivity. Meanwhile, we can relate the electric displacement $\boldsymbol{D}$ to the electric field $\boldsymbol{E}$ and medium polarization via:

$$\boldsymbol{D} = \varepsilon_0 \boldsymbol{E} + \boldsymbol{P} \qquad (2.27).$$

By combining equations (2.26), (2.27), and (2.28), we can derive an expression for the electric displacement:

$$\boldsymbol{D} = \varepsilon_0 \left({\omega_p^2}/{(\omega^2 + i\gamma\omega)} \right) \boldsymbol{E} \qquad (2.28)$$

The term $\omega_p^2 = {ne^2}/{\varepsilon_0 m}$ is recognized as the plasma frequency, where m denotes the electron mass, e stands for the electronic charge, and γ represents the damping constant, which is expressed as $ne/m\sigma$, with σ referring to the metal's conductivity. By comparing Equations (2.1.6) and (2.1.8), we can derive an expression for the dielectric function of the free electron gas, as:

$$\varepsilon(\omega) = 1 - {\omega_p^2}/{(\omega^2 - i\gamma\omega)} \qquad (2.29).$$

The given equation can be conveniently expressed in terms of its real and imaginary components, where $\varepsilon(\omega)$ is represented as $\varepsilon_1(\omega) + i\varepsilon_2(\omega)$. To be more explicit, we can define $\varepsilon_1(\omega)$and $\varepsilon_2(\omega)$ as follows:

$\varepsilon_1(\omega) = 1 - {\omega_p^2}/{(\omega^2 + \gamma^2)}$ and $\varepsilon_2(\omega) = 1 - \frac{\gamma\omega_p^2}{\omega(\omega^2+\gamma^2)}$.

Thus, the equation takes the form:

$$\varepsilon(\omega) = 1 - \frac{\omega_p^2}{\omega^2+\gamma^2} + \frac{i\gamma\omega_p^2}{\omega(\omega^2+\gamma^2)} \qquad (2.30).$$

Please note that this separation into real and imaginary parts allows for a clearer understanding of the physical implications of the equation. The real part, $\varepsilon_1(\omega)$, corresponds to the dispersive behavior of the material, while the imaginary part, $\varepsilon_2(\omega)$, accounts for its absorptive or dissipative characteristics.

For a medium that is both isotropic and lossless, where ω is significantly large ($\omega >> \gamma$), the dielectric function is primarily real. As such, the dielectric function, $\varepsilon_1(\omega)$ simplifies to:

$$\varepsilon(\omega) = 1 - {\omega_p^2}/{\omega^2} \qquad (2.31).$$

As an illustration, Fig.2.12 presents a plot of both real and imaginary components of the dielectric constant based on Equation (2.29). This plot pertains to a free electron gas with a plasma frequency $\omega_p = 13.8 \times 10^{15} S^{-1}$ and a damping constant $\gamma = 1.075 \times 10^{14} S^{-1}$, as extrapolated from the Drude model for a free electron gas.

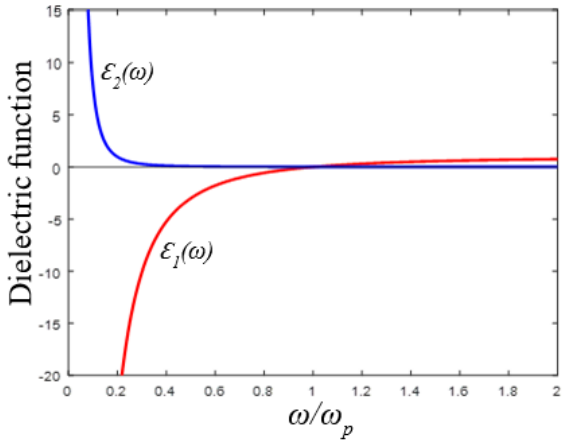

Figure.2.12. Real $\varepsilon_1(\omega)$ and imaginary $\varepsilon_2(\omega)$ parts of the dielectric function of an electron gas.

In light of equation (2.32), we can discern that for frequencies below the plasma frequency, the dielectric function is real and negative, leading to a purely imaginary wavenumber *k*, due to the strong imaginary part of the refractive index $n = \sqrt{\varepsilon}$. Consequently, incident electromagnetic wave cannot penetrate the metal but is totally reflected, making them shiny in the visible range. The fields do, however, exhibit slight penetration into the metal, resulting in an exponential attenuation. Beyond the plasma frequency, the dielectric function turns positive. The field oscillations then outpace the free electrons, leading to a real-valued wavenumber, and the metal loses its reflective property.

In pursuit of the dispersion relation of bulk plasmons, Maxwell's curl equations can be united to form the wave equation:

$$\left(\varepsilon/_{c^2}\right)\frac{\partial^2 E}{\partial t^2} = \nabla^2 E \qquad (2.32)$$

We can explore a solution for Equation (2.33) using **E** = exp (*i* (**k**.**r** - ωt)), which results in:

$$\left(\varepsilon\mu/_{c^2}\right)\omega^2 = k^2 \;\Rightarrow k = (\omega/_c)\sqrt{\varepsilon\mu} \qquad (2.33).$$

Implementing Equations (2.31) and (2.33) alongside $\mu = 1$ for nonmagnetic media, we obtain:

$$k = (\omega/c)\sqrt{1 - \omega_p^2/\omega^2} \qquad (2.34),$$

which leads to the dispersion equation:

$$\omega^2 - \omega_p^2 = k^2c^2 \Rightarrow \omega^2 = \omega_p^2 + k^2c^2 \qquad (2.35).$$

The dispersion relation of bulk plasmon polaritons, as per equation (2.35), is graphically represented in Fig.2.13, which shows that metals allow propagation of electromagnetic waves above the plasma frequency. Thus, metals become transparent.

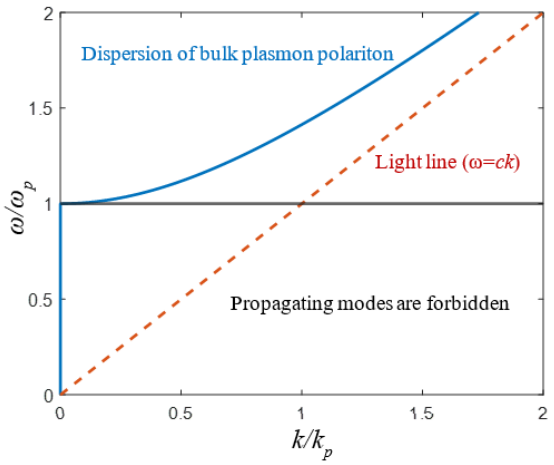

Figure.2.13. Dispersion relation of bulk plasmon polariton of free electron gas. Propagation of electromagnetic wave is not allowed below ω_p since the wavenumber k is imaginary. The plasma wavenumber, $k_p = \omega_p/c$.

As can be observed in Fig.2.13, the bulk plasmon modes lie close to the light line at high frequencies, while they move away from it at low frequencies. Solving the dispersion relation of equation (2.35) shows that solutions lie above the light line where $\omega > \omega_p$, allowing for transverse electromagnetic (TEM) waves to propagate with group velocity $V_g = d\omega/dk < c$

(which is lower than the speed of light). Conversely, where $\omega < \omega_p$, electromagnetic wave propagation is not permitted, thus creating a forbidden region for the bulk plasmon.

2.6.2 Surface plasmon polaritons at a planar interface

This section establishes the dispersion relation for surface plasmon polaritons (SPPs) arising at the interface between a dielectric and a metal (Figure 2.14). SPPs are collective electron density waves that propagate along the interface. They exploit the free movement of loosely bound electrons in metals in response to an external electric field.

Here, we focus on a single planar interface and determine the dispersion relation for the SPP modes supported at this interface using Maxwell's equations and appropriate boundary conditions for the fields in each medium. We consider solutions for propagating waves guided along the flat interface ($z = 0$ in the Cartesian coordinate system) that exhibit exponential decay in both positive and negative z-directions away from the interface (Figure 2.14). This indicates modes propagating along the *x*-direction.

The dielectric medium is characterized by a positive real and frequency-independent dielectric constant (ε_1). The metal medium, on the other hand, is described by a complex, frequency-dependent dielectric function ($\varepsilon_2(\omega)$) following the Drude model.

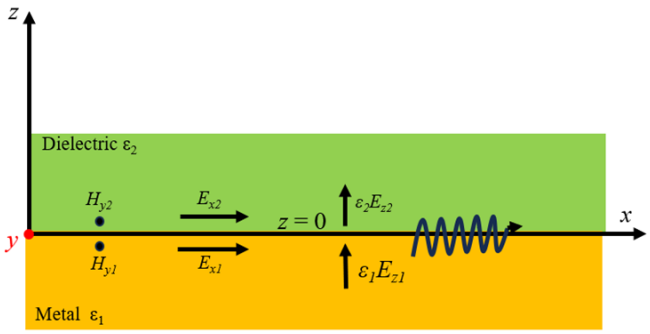

Figure.2.14. Schematic of SPP modes at the interface between metal and dielectric.

Our objective is to find solutions for possible guided modes localized at the interface by solving Maxwell's equations in both half-spaces ($z > 0$ and $z < 0$). These modes correspond to transversemagnetic (TM) or p-polarized waves. We assume a time-harmonic field of the form

$$\mathbf{E} = \mathbf{E_0}\exp\left[i\left(k_x x + k_z z\right)\right]\exp(-i\omega t) \qquad (2.36),$$

that excites these localized plasmon waves.

Now let's consider the interface between air (medium 2) and metal (medium 1).

For $z > 0$, we denote the electric and magnetic fields as:

$$\begin{cases} E_2 = \begin{pmatrix} E_{x2} \\ 0 \\ E_{z2} \end{pmatrix} e^{j(k_{x2}x + k_{z2}z - \omega t)} \\ H_2 = \begin{pmatrix} 0 \\ H_{y2} \\ 0 \end{pmatrix} e^{j(k_{x2}x + k_{z2}z - \omega t)} \end{cases}$$

Similarly, for $z < 0$, these fields are expressed as:

$$\begin{cases} E_1 = \begin{pmatrix} E_{x1} \\ 0 \\ E_{z1} \end{pmatrix} e^{j(k_{x1}x - k_{z1}z - \omega t)} \\ H_1 = \begin{pmatrix} 0 \\ H_{y1} \\ 0 \end{pmatrix} e^{j(k_{x1}x - k_{z1}z - \omega t)} \end{cases}$$

Applying boundary conditions at the interface where $z = 0$, we equate the components of the electric and magnetic fields as:

$$E_{x1} = E_{x2}$$

$$H_{y1} = H_{y2}$$

$$\varepsilon_1 E_{z1} = \varepsilon_2 E_{z2},$$

and under these conditions, no transverse- electric (TE) modes can exist, instead transverse-magnetic (TM) modes propagate at the interface between the dielectric-metal interface along the *x*-direction [53].

$$\Rightarrow k_{x1} = k_{x2} = k_x$$ Again,

from Maxwell's equations, $\nabla \times H_i = \varepsilon_i \frac{\partial E_i}{\partial t}$, $(i = 1,2)$ (2.37).

By applying the curl operator to the magnetic field *H*, we can decompose it into various field components using:

$$\nabla \times H = \begin{vmatrix} \hat{a}_x & \hat{a}_y & \hat{a}_z \\ \frac{\partial}{\partial x} & \frac{\partial}{\partial y} & \frac{\partial}{\partial z} \\ 0 & H_{yi} & 0 \end{vmatrix} = -\hat{a}_x \frac{\partial H_{yi}}{\partial z} + \hat{a}_z \frac{\partial H_{yi}}{\partial x}$$ (2.38).

From here, it follows that:

$$jk_{z1} H_{y1} = -j\omega\varepsilon_1 E_{x1}$$ (2.39)

and,

$$-jk_{z2} H_{y2} = -j\omega\varepsilon_2 E_{x2}$$ (2.40).

Given that $E_{x1} = E_{x2,}$ (from the boundary conditions), it can be inferred from equations (2.40) and (2.39) that:

$$\frac{k_{z1} H_{y1}}{\omega\varepsilon_1} + \frac{k_{z2} H_{y2}}{\omega\varepsilon_2} = 0$$ (2.41)

With the understanding that $H_{y1} = H_{y2}$, hence, $\frac{k_{z1}}{\varepsilon_1} + \frac{k_{z2}}{\varepsilon_2} = 0$ (2.42).

By applying the wave-vector relation, we obtain the following equations:

$$k_x^2 = \varepsilon_1(^{\omega}/_{c})^2 - k_{z1}^2 \quad (2.43),$$

$$k_x^2 = \varepsilon_2(^{\omega}/_{c})^2 - k_{z2}^2 \quad (2.44).$$

From equation (2.43), we can reformulate equation (2.44) into:

$$k_x^2 = \varepsilon_2(^{\omega}/_{c})^2 - \left(^{\varepsilon_2 k_{z1}}/_{\varepsilon_1}\right)^2 \quad (2.45),$$

Consequently, equation (2.44) can be rewritten as:

$$k_{z1}^2 = \varepsilon_1(^{\omega}/_{c})^2 - k_x^2 \quad (2.46),$$

Upon substituting equation (2.47) into equation (2.46), we arrive at the following expressions:

$$k_x^2 = (^{\omega}/_{c})^2 \left(\frac{\varepsilon_1\varepsilon_2}{\varepsilon_1+\varepsilon_2}\right) = k_x = (^{\omega}/_{c})\sqrt{\frac{\varepsilon_1\varepsilon_2}{\varepsilon_1+\varepsilon_2}} \quad \text{or} \quad k_x = (^{\omega}/_{c})\sqrt{\frac{\varepsilon_m\varepsilon_d}{\varepsilon_m+\varepsilon_d}} \quad (2.47).$$

Equation (2.48) provides a valuable insight into the dispersion relation governing the behavior of surface plasmon polariton (SPP) waves propagating across the interface of a metal and a dielectric material. In this particular context, the symbols ε_m and ε_d represent the dielectric constants for the metal and dielectric mediums, respectively, with $\varepsilon_m = \varepsilon_1$ and $\varepsilon_d = \varepsilon_2$. Additionally, $k_x = k_{sp}$ serves as the mode propagation constant.

To visualize these relationships and the dispersion behavior of plasma modes and SPPs at the boundaries between metal/dielectric and metal/air, refer to the graph depicted in Fig. 2.15.

We assume that, the dielectric constant in the metal is given by $\varepsilon(\omega) = 1 - {\omega_p^2}/{(\omega^2 - i\gamma\omega)}$, and for the dielectric medium, ε_d = 4. We assume the dielectric constant for air to be 1. The parameters $\omega_p = 5 \times 10^{15} S^{-1}$ and $\gamma = 1.075 \times 10^{14} S^{-1}$, while represents the surface plasmon frequency.

The plot illustrates an intriguing relationship: a dielectric medium with a higher dielectric constant lead to a lower ω_{SP} . Furthermore, it vividly demonstrates that the entire SPP dispersion relation lies below the light cones.

In summary, these observations shed light on the impact of dielectric constants on surface plasmon behavior and highlight the confinement of SPP dispersion within the boundaries defined by the light line (cones).

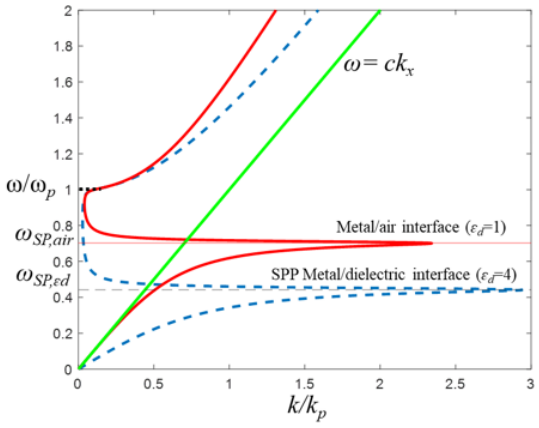

Figure.2.15. Surface plasmon polariton plots at the interface between a metal and dielectric (blue dashed lines), and metal and air (red solid line).

A surface mode refers to charges accumulating at the boundary between the metal and the dielectric. This accumulation gives rise to an electric field that originates from positive charges and terminates at negative charges, existing in both the dielectric and metal mediums as depicted in Fig. 2.16. Consequently, in the presence of surface charges, the electric field components normal to the surface must exhibit opposite charges.

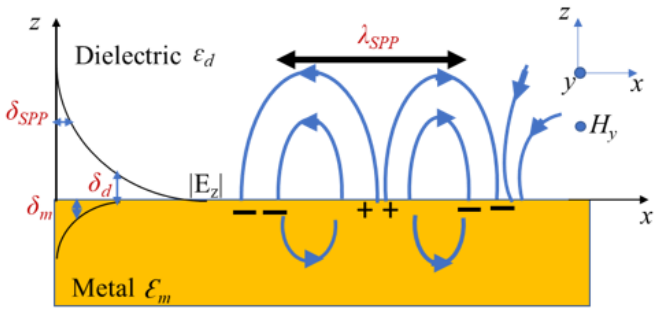

Figure.2.16. Schematic representation of an electromagnetic wave and surface charges residing at the metal-dielectric interface, which shows the strength and components of a surface plasmon polariton, accompanied by an enhancement of the local electric field component near the surface that exponentially decays with distance in a direction normal to the interface.

The electric field of the excited SPP wave decays exponentially with distance normal to the interface. The penetration depths, $\delta_d = {}^{1}/_{k_{z2}}$ and $\delta_m = {}^{1}/_{k_{z1}}$ in the dielectric and metal at which the electric fields fall to 1/e.

By referencing the dispersion relation equation (2.48), for surface plasmon polariton (SPP) waves and the wave-vector equation, we can determine the penetration depth (δ_d) of the surface plasmon polariton (SPP) wave into the dielectric as:

$$\delta_d = \frac{1}{k}\left|\frac{\varepsilon_d+\varepsilon_m}{-\varepsilon_d^2}\right|^{1/2} \qquad (2.48).$$

Similarly, utilizing equation (2.48), the penetration depth (δ_m) of the SPP wave into the metal can be expressed as:

$$\delta_m = \frac{1}{k}\left|\frac{\varepsilon_d+\varepsilon_m}{-\varepsilon_m^2}\right|^{1/2} \qquad (2.49),$$

where $k = {}^{2\pi}/_{\lambda}$ is the free space wavenumber.

Surface charges can instigate a collective oscillation, leading to the excitation of Surface Plasmon Polaritons (SPPs). The dielectric constant of the metal, denoted as ε_m, adopts the form of a free electron, is expressed as:

$$\varepsilon_1(\omega) = 1 - \frac{{\omega_p}^2}{\omega^2} \ .$$

For most metals, ω_p (bulk plasma frequency) resides in the ultraviolet wavelength regime. Beyond this frequency, the metal loses its metallic properties.

The dispersion relation uncovers an intriguing behavior of the surface mode. At low frequencies, the surface mode closely tracks the light line, exhibiting light-like characteristics. However, as the frequency increases, the mode gradually deviates from the light line and eventually reaches an asymptotic limit. This phenomenon occurs when the permittivities of both mediums possess the same magnitude but opposite signs, resulting in a pole in the dispersion equation (2.47). This relationship leads to $\varepsilon_m = -\varepsilon_d$, allowing us to express the dielectric constant of the metal as:

$$1 - \frac{\omega_p^2}{\omega^2} = -\varepsilon_2 \qquad (2.50).$$

With this, we can calculate the SPP frequency as:

$$\omega_{SPP} = \frac{\omega_p}{\sqrt{1+\varepsilon_2}} \qquad (2.51).$$

Equation (2.51) represents the upper cutoff frequency for the surface mode, and in vacuum, when $\varepsilon_2 = 1$, it simplifies to:

$$\omega_{SPP} = \frac{\omega_p}{\sqrt{2}} \qquad (2.52).$$

Notably, the SPP frequency is found to be lower than the bulk plasma frequency. As previously mentioned, the excitation of SPPs heavily relies on this fundamental premise.

We can then employ equations (2.51) and (2.52) to calculate the SPP wavelength λ_{SPP}.

In summary, this exploration of the unique optical characteristics of the electron gas in metals offers valuable insights into the behavior of plasmon polaritons, both in bulk and at interfaces. The derived expressions and dispersion relations pave the way for designing and engineering nanostructures with tailored optical properties, promising a myriad of applications in fields such as photonics, sensing, and optoelectronics.

2.7 References

[1] X. Fan, W. Zheng, & D. Singh, "Light scattering and surface plasmons on small spherical particles," Light: Science & Applications, 3, e179 (2014).

[2] L. Mascaretti, Y. Chen, O. Henrotte, O. Yesilyurt, V. M. Shalaev, A. Naldoni, & A. Boltasseva, "Designing metasurfaces for efficient solar energy conversion," ACS Photonics, 10(12), 4079–4103 (2023).

[3] I. Haddouche & L. Cherbi, "Comparison of finite element and transfer matrix methods for numerical investigation of surface plasmon waveguides," Optics Communications, 382, 132-137 (2017).

[4] Y. Zhuo, "The theoretical study of passive and active optical devices via planewave based transfer (scattering) matrix method and other approaches," United States (2011). https://doi.org/10.2172/1029601.

[5] A. Deinega, S. Belousov, & I. Valuev, "Hybrid transfer-matrix FDTD method for layered periodic structures," Optics Letters, 34(6), 860-862 (2009).

[6] J. Na & H. Noh, "Investigation of a broadband coherent perfect absorber in a multi-layer structure by using the transfer matrix method," Journal of the Korean Physical Society, 72(1), 66-70 (2018).

[7] R. R. Grote, J. B. Driscoll, C. G. Biris, N. C. Panoiu, & R. M. Osgood, Jr., "Weakly modulated silicon-dioxide-cladding gratings for silicon waveguide Fabry-Pérot cavities," Optics Express, 19(27), 26406-26415 (2011).

[8] J. Zhang & L. Zhang, "Nanostructures for surface plasmons," Advances in Optics and Photonics, 4, 157-321 (2012).

[9] A. V. Zayats, I. I. Smolyaninov, & A. A. Maradudin, "Nano-optics of surface plasmon polaritons," Physics Reports, 408(3-4), 131-314 (2005).

[10] M. Guarnieri, "The rise of light," in 2015 ICOHTEC/IEEE International History of High-Technologies and their Socio-Cultural Contexts Conference (HISTELCON), Tel-Aviv, Israel, pp. 1-14 (2015).

[11] J. Needham, Science and Civilization in China: Volume 4, Physics and Physical Technology, Part 1, Physics*, Cambridge University Press (1986).

[12] W. Gilbert, De Magnete, Peter Short (1600).

[13] B. Franklin, Experiments and Observations on Electricity, E. Cave (1751).

[14] M. Faraday, Experimental Researches in Electricity, Bernard Quaritch (1832).

[15] A. M. Ampère, Recueil d'observations électrodynamiques, Chez Crochard (1827).

16. [16] J. C. Maxwell, A Dynamical Theory of the Electromagnetic Field, Philosophical Transactions of the Royal Society of London (1865).

[17] R. P. Feynman, R. B. Leighton, & M. Sands, “The Feynman Lectures on Physics: Gravitation, Basic Books” (2011).

[18] R. G. Muncaster, “A-level Physics, Nelson Thornes” (2012).

[19] B. E. A. Saleh & M. C. Teich, “Fundamentals of Photonics (2nd ed.)”, Wiley-Interscience (2007).

[20] J. D. Jackson, “Classical Electrodynamics” (3rd ed.), John Wiley & Sons (1999).

[21] C. Kittel, “Introduction to Solid State Physics (8th ed.)”, John Wiley & Sons (2005).

[22] M. Born & K. Huang, “Dynamical Theory of Crystal Lattices”, Oxford University Press (2013).

[23] N. Engheta & R. W. Ziolkowski (Eds.), “Metamaterials: Physics and Engineering Explorations”, John Wiley & Sons (2006).

[24] Z. Wang, L. Chen, & S. W. Tsai (Eds.), “Introduction to Electromagnetic Theory: A Modern Perspective (2nd ed.)”, CRC Press (2015).

[25] M. I. Stockman, "Nanoplasmonics: The Physics Behind the Applications," Physics Today, 64(2), 39-44 (2011).

[26] V. M. Agranovich & D. L. Mills, “Surface Polaritons: Electromagnetic Waves at Surfaces and Interfaces”, North-Holland (1986).

[27] H. A. Atwater & A. Polman, "Plasmonics for improved photovoltaic devices," Nature Materials, 9(3), 205-213 (2010).

[28] M. Li, S. K. Cushing, N. Wu, & Y. Wu, "Plasmon-enhanced optical sensors: a review," Analyst, 140(2), 386-406 (2015).

[29] M. A. Noginov, G. Zhu, A. M. Belgrave, R. Bakker, V. M. Shalaev, E. E. Narimanov, & V. A. Podolskiy, "Demonstration of a spaser-based nanolaser," Nature, 460(7259), 1110-1112 (2009).

[30] T. W. Ebbesen, H. J. Lezec, H. F. Ghaemi, T. Thio, & P. A. Wolff, "Extraordinary optical transmission through sub-wavelength hole arrays," Nature, 391(6668), 667-669 (1998).

[31] A. V. Kildishev, A. Boltasseva, & V. M. Shalaev, "Planar Photonics with Metasurfaces," Science, 339(6125), 1232009 (2013).

[32] Z. Fang, Z. Liu, Y. Wang, P. M. Ajayan, & P. Nordlander, "Graphene-antenna sandwich photodetector," Nano Letters, 12(8), 3808-3813 (2013).

[33] N. Yu & F. Capasso, "Flat optics with designer metasurfaces," Nature Materials, 13(2), 139-150 (2014).

[34] M. Di Ventra, S. Evoy, & J. R. Heflin (Eds.), “Introduction to Nanoscale Science and Technology”, Springer Science & Business Media (2012).

[35] R. Weissleder, "A clearer vision for in vivo imaging," Nature Biotechnology, 19(4), 316-317 (2001).

[36] F. L. Pedrotti, L. S. Pedrotti, & L. M. Pedrotti, Introduction to Optics (3rd ed.), Cambridge University Press (2017).

[37] M. Born & E. Wolf, Principles of Optics: Electromagnetic Theory of Propagation, Interference and Diffraction of Light, Cambridge University Press (1999).

[38] R. W. Wood, "On a Remarkable case of uneven distribution of light in a diffraction grating spectrum," Philosophical Magazine, 4(21), 396-402 (1902).

[39] L. Rayleigh, "On the Remarkable Phenomenon of Wave Propagation over a Plane Surface of Unusual Wave-length," Scientific Papers, Vol. II, 431-437 (1907).

[40] U. Fano, "The Theory of Anomalous Diffraction Gratings and of Quasi-Stationary Waves on Metallic Surfaces," Journal of the Optical Society of America, 31(3), 213-222 (1941).

[41] R. H. Ritchie, "Plasma losses by fast electrons in thin films," Physical Review, 106(5), 874-881 (1957).

[42] H. E. Bennett & J. L. Stanford, "Structure-Related Optical Characteristics of Thin Metallic Films in the Visible and Ultraviolet," J Res Natl Bur Stand A Phys Chem, 80A (4), 643-658 (1976).

[43] A. Otto, "Excitation of Nonradiative Surface Plasma Waves in Silver by the Method of Frustrated Total Reflection," Zeitschrift für Physik, 216(4), 398-410 (1968).

[44] E. Kretschmann & H. Raether, "Radiative Decay of Nonradiative Surface Plasmons Excited by Light," Zeitschrift für Naturforschung A, 23(12), 2135-2136 (1968).

[45] H. Raether, "Surface-plasmons on smooth and rough surfaces and on gratings," Springer Tracts in Modern Physics, 111, 4-39 (1988).

[46] R. H. Ritchie, “Plasma losses by fast electrons in thin films”, Physical Review, 106(5), 874 (1957).

[47] S. A. Maier, “Plasmonics: Fundamentals and applications”, Springer Science+Business Media LLC (2007).

Chapter 3

Contents

3.0 Fano resonances

The interaction of light with nanostructured materials is a cornerstone of modern photonics research. This chapter explores a fascinating phenomenon called Fano resonances, which significantly impacts light-matter interactions at the nanoscale.

Fano resonances arise from the interplay between two distinct light states within a material: discrete and continuum states. Discrete states are localized light resonances confined within a small region, analogous to a "dark room" within the material. Continuum states, on the other hand, represent a vast sea of light waves constantly propagating through the material. The interaction between these states, where light bounces between the localized state and the surrounding continuum, manifests as a unique fingerprint in the light's behavior.

Fano resonances were initially discovered in the context of interacting quantum systems [1]. However, their fundamental principles extend to classical wave phenomena as well. A classic example is their observation in the absorption spectra of atomic gases, where the interaction of a continuum of propagating light waves with a localized atomic energy level creates a Fano resonance. These resonances are distinguished by their characteristically asymmetric spectral line shapes, deviating from the typical symmetric profiles of isolated resonances [2]. Additionally, Fano resonances are often accompanied by a significant shift in the phase response around the resonant frequency [3].

To gain a deeper understanding of Fano resonances, Section 3.1 employs a visual exploration using diagrams (Fig. 3.3). These diagrams illustrate the superposition of a Lorentzian line shape (characteristic of a discrete state) with a flat continuous background (representing the continuum), resulting in the asymmetric lineshape profile that defines a Fano resonance. The

Fano parameter (q) plays a crucial role in quantifying the degree of asymmetry. By analyzing the Fano resonance line-shape profile for various values of q (Fig. 3.3), we can gain insights into the interplay between the trapped and continuous light states.

Section 3.2 delves into the theoretical foundation of Fano resonances from a quantum mechanics perspective. Understanding bound (discrete) and continuum states, which are fundamental concepts for realizing Fano resonances in quantum systems, is paramount for this analysis. The example of a one-dimensional finite potential square well serves as a helpful illustration of these concepts.

Section 3.3 explores the fascinating realm of photonic nanostructures, where Fano resonances emerge when light interacts with metallic or dielectric objects at the nanoscale. This section highlights the versatility of Fano resonances and bridges the gap between classical and quantum mechanics, providing a holistic picture of light's behavior in these miniature structures.

Researchers have extensively studied Fano resonances in various nanostructures [4-7]. These resonances can occur due to the interaction between different types of light waves (broad and narrow) within the structure, ultimately affecting how light scatters. Plasmonic nanostructures, meticulously designed using metallic nanoparticles, are a prime example [8]. Within a metallic nanoparticle array, broad (bright) and narrow (dark) optical modes can interact, generating asymmetric line shapes in the scattering spectrum. The strong field enhancement observed in Fano structures holds promise for applications in molecular sensors and other optical devices [9, 10]. However, inherent metal losses in plasmonic nanostructures can limit their overall

effectiveness in certain photonic applications, particularly those requiring high sensitivity, such as optical sensors.

Recent advancements have led to the exploration of Fano resonances in non-metallic (dielectric) materials, which overcome the light absorption issue of metals [11-15]. These structures can produce extremely sharp Fano resonances, offering significant advantages for sensors and switching devices. They achieve this by utilizing a special type of light resonance called a Mie resonance [11-15].

As a final exploration, Section 3.3.1 ventures beyond purely metallic or purely dielectric nanostructures by examining the potential of hybrid plasmonic-dielectric metamaterials. By strategically combining these two material classes, we can unlock a multitude of intriguing optical processes, including Fano resonances, Rabi splitting, and bound states in the continuum (BICs). These processes can significantly enhance quality-factors (*Q*-factors), a crucial parameter for high-performance photonic applications such as sensors, lasers, and optical switches [16,17].

3.1 Theory of Fano resonances

Fano resonances are a captivating phenomenon in physics where a localized, discrete state interferes with a continuous background, leading to an asymmetric response in the observed spectrum. This insightful concept was first introduced by Italian-American physicist Ugo Fano during his studies on electron scattering by helium atoms.

Figure.3.1. Ugo Fano (July 28, 1912 – February 13, 2001): An Italian-American physicist.

The essence of Fano resonances lies in the interplay between a discrete state and a continuum of states within a wave system. When an external field excites the discrete state, it can interfere constructively or destructively with the background continuum. This intricate interference manifests as an asymmetric spectral response, characterized by the distinctive Fano lineshape.

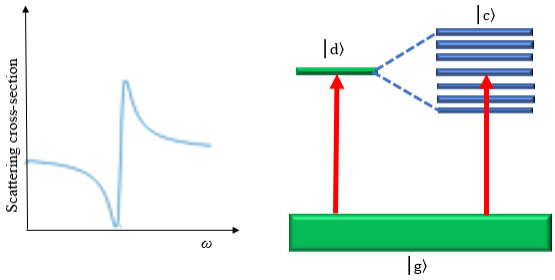

Figure. 3.2: Schematic representation of Fano resonance in a two-level quantum mechanical system. The interaction between a discrete state (|d⟩) and a continuum state |c⟩ (represented by the blue horizontal lines) leads to the asymmetric lineshape characteristic of a Fano resonance.

To illustrate this concept, consider a simplified two-level system (Fig.3.2). One level represents a localized discrete state $|d\rangle$, while the other embodies a continuum of states $|c\rangle$. An incident wave interacting with this system can either be directly scattered or absorbed and

subsequently re-emitted. The interplay between these two pathways leads to the characteristic asymmetric lineshape known as the Fano profile.

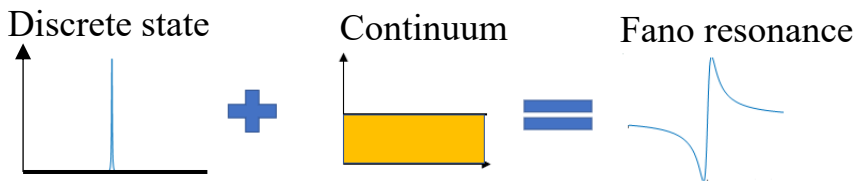

Figure. 3.3. Schematic of Fano resonance as a superposition of the Lorentzian lineshape of the discrete level with a flat continuous background.

Consider a simplified quantum mechanical system consisting of a discrete state, denoted as $|\psi_d\rangle$, and a continuum of states represented by $|\psi_c\rangle$. The system's total wavefunction can be expressed as:

$$|\Psi\rangle = a\,|\psi_d\rangle + \int b(E)\,|\psi_c(E)\rangle\,dE$$

In this equation, the coefficient *a* represents the amplitude of the discrete state, while *b(E)* denotes the amplitude of the continuum state at a specific energy *E* [18].

When an external field excites the discrete state, it can interfere with the continuum states. This interaction leads to an asymmetric spectral response profile, typically characterized by the Fano lineshape (Fig. 3.3). This phenomenon can be mathematically described using the Fano formula:

$$\sigma = \frac{(\epsilon+q)^2}{\epsilon^2+1} \qquad (3.1)$$

This equation, also known as the Fano formula, calculates the scattering cross-section. Here, ϵ represents the normalized energy detuning defined as $\epsilon = \frac{2(E-E_R)}{\gamma}$ where E is the energy of the incoming particle or wave, E_R is the resonance energy (energy of the discrete state), γ is the resonance width (characterizing the state's decay rate), and q is the Fano asymmetry parameter that determines the line shape's asymmetry [3].

Equation 3.1 effectively captures the resonance condition established by Fano and highlights the intricate interplay between discrete and continuous scattering states.

Figure 3.4 depicts the normalized scattering cross-section for Fano resonances with various asymmetry parameter (q) values. These plots represent the graphical solutions of Eq. 3.1 for different q values. When the excitation of the discrete state is minimal ($|q|$ approaches zero, e.g., q = 0.1), the profile exhibits a nearly symmetric window-type resonance (black curve in Fig. 3.4).

Conversely, when the excitation of the continuum background is negligible ($|q|$ is large, e.g., q = 10000), the profile appears as a near-perfect symmetric positive peak (magenta curve in Fig. 3.4). In this scenario, the Fano resonance can be envisioned as a quasi-bound state in the continuum (BIC).

For intermediate q values (e.g., q = -2 and q = 2), the curves display distinct asymmetric peak profiles, with the minimum dipping to zero at $\epsilon = -q$. It's important to note that when a state

couples to multiple continua, the spectrum might not necessarily reach zero, as discussed in more detail in section 4 of Fano's 1961 paper [1].

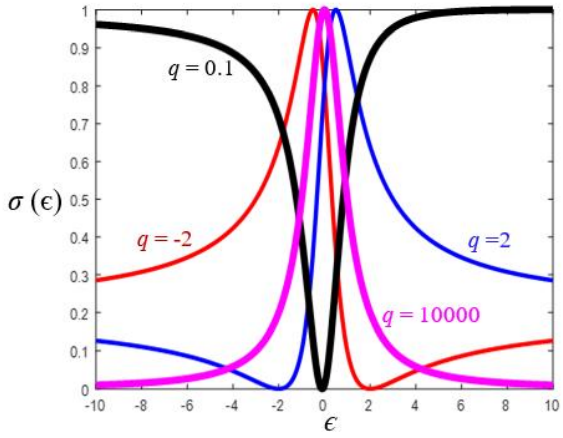

Figure.3.4. The Fano resonance line-shape profile with different values of the Fano parameter *q*.

3.2 Finite potential square well

The study of discrete and continuum states in quantum mechanics benefits from exploring a fundamental model: the one-dimensional finite potential square well (Fig. 3.4). In this system, a particle with energy *E* is confined within a region where the potential energy (V) is lower than a constant value (V_0). This confinement creates a valuable model system that embodies the characteristics of both bound and scattering states [18]. The simplicity of the finite square well makes it a ubiquitous tool for understanding various quantum systems, including atomic and molecular systems, as well as quantum dots in semiconductor devices [19, 20].

For our analysis, we focus on a one-dimensional scenario with a finite potential well defined by walls at x = -L/2 and x = L/2. The potential energy within the well is denoted by V_0 (well depth).

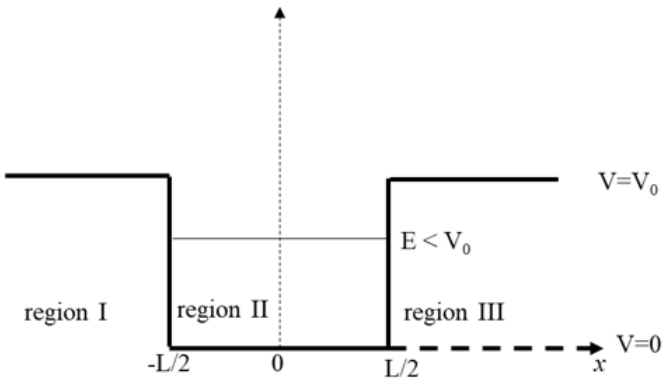

Figure.3.5. Finite potential square well with depth V_0, and width L.

Applying the time-independent Schrödinger's equation, we will dissect the behavior of a particle in a finite potential well, scrutinizing the different regions separately.

For region I, where $x \leq -\frac{L}{2}, V(x) = V_0$, we engage the time-independent Schrödinger's equation, which presents as follows:

$$-\frac{\hbar^2}{2m}\frac{d^2\psi}{dx^2} + V_0\psi = E\psi \Rightarrow \qquad \frac{d^2\psi}{dx^2} = \frac{2m}{\hbar^2}(V_0 - E)\psi$$

Here, *x* is the position variable in the one-dimensional space that the particle is moving in, *L* is the width of the potential well. The potential well is assumed to extend from -*L*/2 to *L*/2, *V*(*x*) is the potential energy function, which is dependent on the position *x*, V_0 is the potential energy

inside the potential well, E is the energy of the particle, when $E < V_0$, the particle is in a bound state and confined within the potential well.

ψ is the wave function of the particle, which contains all the information about the state of the particle, h is the Planck's constant, and $\hbar = h/2\pi$ is the reduced Planck's constant.

m is the mass of the particle, k is a constant derived from the parameters of the problem related to the wave number of the wave function., B and D are the constants of integration, which will be determined by the boundary conditions of the problem.

Thus, we derive the equation $\frac{d^2\psi}{dx^2} = \kappa^2\psi$, where $\kappa^2 = \frac{2m}{\hbar^2}(V_0 - E)$, and importantly, this is greater than zero since $E < V_0$. This confirms κ as a real number, as $\kappa = \sqrt{\frac{2m}{\hbar^2}(V_0 - E)} > 0$.

The resulting solutions to this differential equation can be written as:

$$\psi = Be^{\kappa x} + De^{-\kappa x}$$

However, considering the limit as $x \to -\infty$, and $\psi \to 0$, we deduce that $D = 0$. Thus, our derived solution in region 1 simplifies to $\psi = Be^{\kappa x}$.

In region III, $x \geq \frac{L}{2}, V(x) = V_0$, the mathematical treatment aligns closely with that of region 1. By solving the differential equation in this region, we can represent the solutions as:

$$\psi = Ae^{-\kappa x} + Ce^{\kappa x}$$

However, given that the wave function $\psi \to 0$ as $x \to +\infty$, the constant $C = 0$. This simplification results in the solution for region 3 becoming:

$$\psi = Ae^{-\kappa x}$$

This means the wave function in region III decays exponentially as we move away from the well, which is indicative of the particle's confinement within the potential well.

To analyze the scenario within region II, defined as $-L/2 \leq x \leq L/2$ where $V(x) = 0$, we employ the time-independent Schrödinger equation as follows:

$$-\frac{\hbar^2}{2m}\frac{d^2\psi}{dx^2} = E\psi,$$

which can be simplified to $\frac{d^2\psi}{dx^2} = -\frac{2m}{\hbar^2}E\psi$

This eventually leads us to:

$\frac{d^2\psi}{dx^2} = -k^2\psi$, where $k = \sqrt{\frac{2m}{\hbar^2}E}$.

The parameter *k* is real, resulting in two types of solutions based on the parity, i.e., even and odd.

For even parity, indicating symmetry about the well's center, the solution is

$$\psi = C\cos(kx).$$

Conversely, for odd parity, indicative of antisymmetric about the well's center, the solution is $\psi = D\sin(kx)$.

These solutions aptly illustrate the behavior of a particle in a symmetric potential well. These solutions represent the wave functions inside the potential well, oscillating between positive and negative values, a typical behavior of quantum particles in bounded states.

We now proceed to equate both the wave function, $\psi(x)$, and its derivative, $\frac{d\psi(x)}{dx}$, at the boundaries of the well, specified at $x = \pm\frac{L}{2}$. This process must be performed twice since we have solutions for both even and odd parities.

At $x = \frac{L}{2}$ for even parity, we equate ψ:

$$Ae^{-\kappa\frac{L}{2}} = C\cos\left(k\frac{L}{2}\right) \qquad (3.2)$$

And we equate $\frac{d\psi}{dx}$:

$$Ake^{-\kappa\frac{L}{2}} = -Ck\sin\left(k\frac{L}{2}\right) \qquad (3.3)$$

By dividing equation (3.3) by equation (3.2) to eliminate *A* and *C*, we get:

$$\tan\left(\frac{kL}{2}\right) = \frac{\kappa}{k} \qquad (3.4)$$

A similar analysis can be performed for odd parity solutions, leading to:

$$\cot\left(\frac{kL}{2}\right) = -\frac{\kappa}{k} \qquad (3.5a)$$

$$\tan\left(\frac{kL}{2} + \frac{\pi}{2}\right) = \frac{\kappa}{k} \qquad (3.5b)$$

Given that:

$\kappa = \sqrt{\frac{2m}{\hbar^2}(V_0 - E)}$ and $k = \sqrt{\frac{2m}{\hbar^2}E}$

Equations (3.4) and (3.5) only contain a single unknown variable: the energy, *E*. Both of these equations are transcendental in nature, implying that they do not have straightforward analytical solutions. However, they can be tackled using numerical methods.

For simplification, we'll express these equations using dimensionless parameters η and ζ_0. The parameter η, given by:

$$\eta = \frac{kL}{2} = \frac{L}{2}\sqrt{\frac{2m}{\hbar^2}E}$$

is of particular interest as it encapsulates the energy we're aiming to solve for. Meanwhile, ζ_0 is defined as:

$$\zeta_0 = \frac{L}{2}\sqrt{\frac{2m}{\hbar^2}V_0}$$

This parameter, known as the potential strength parameter, conveys information about the depth (given by V_0) and the width (given by L) of the potential well.

Given our earlier relations:

$$\kappa = \sqrt{\tfrac{2m}{\hbar^2}(V_0 - E)} \quad \text{and,} \quad k = \sqrt{\tfrac{2m}{\hbar^2}E}.$$

We can deduce:

$$\kappa^2 = \frac{2m}{\hbar^2}(V_0 - E) = \frac{2m}{\hbar^2}V_0 - k^2$$

From which it follows:

$$\kappa^2 = k^2\left\{\zeta_0^2\left(\frac{2}{L}\right)^2\frac{1}{k^2} - 1\right\}$$

or equivalently:

$$\frac{\kappa}{k} = \sqrt{\frac{\zeta_0^2}{\eta^2} - 1}$$

Thus, our transcendental equations (3.4) and (3.5) can be rephrased as:

$tan(\eta) = \sqrt{\left(\frac{\zeta_0}{\eta}\right)^2 - 1}$ (3.6) for even parity, and,

$-cot(\eta) = \sqrt{\left(\frac{\zeta_0}{\eta}\right)^2 - 1}$ (3.7) for odd parity. It's important to note that $-cot(\theta) = tan\left(\theta + \frac{\pi}{2}\right)$.

In summary, since $\eta = \frac{kL}{2} = \frac{L}{2}\sqrt{\frac{2m}{\hbar^2}E}$ by determining η, we can subsequently obtain the energy eigenvalues E_n for our finite potential well.

In Fig.3.5, we illustrate the plot of the function $\sqrt{\left(\frac{\zeta_0}{\eta}\right)^2 - 1}$ as a function of η. This is represented for ζ_0 values of 2, 5, and 8.

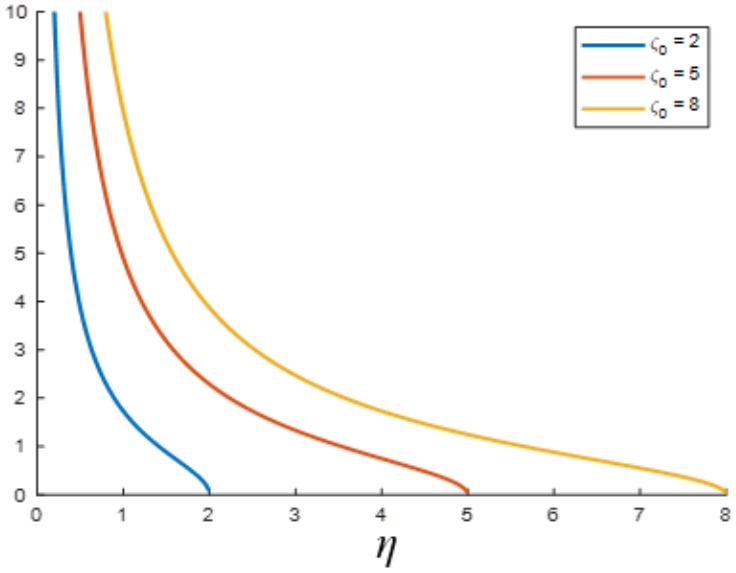

Figure.3.6. $\sqrt{\left(\frac{\zeta_0}{\eta}\right)^2 - 1}$ vs η for ζ_0= 2, 5, and 8 plots

In Fig3.6, we present the plots depicting the solutions for even and odd parity. In particular, we examine the relationship between *tan*(η) and η for even parity solutions. For odd parity solutions, we utilize the equivalent representation, -*cot*(η) = tan(η+π/2). These plots are provided for ζ_0 values of 2, 5, and 8.

(a) (b)

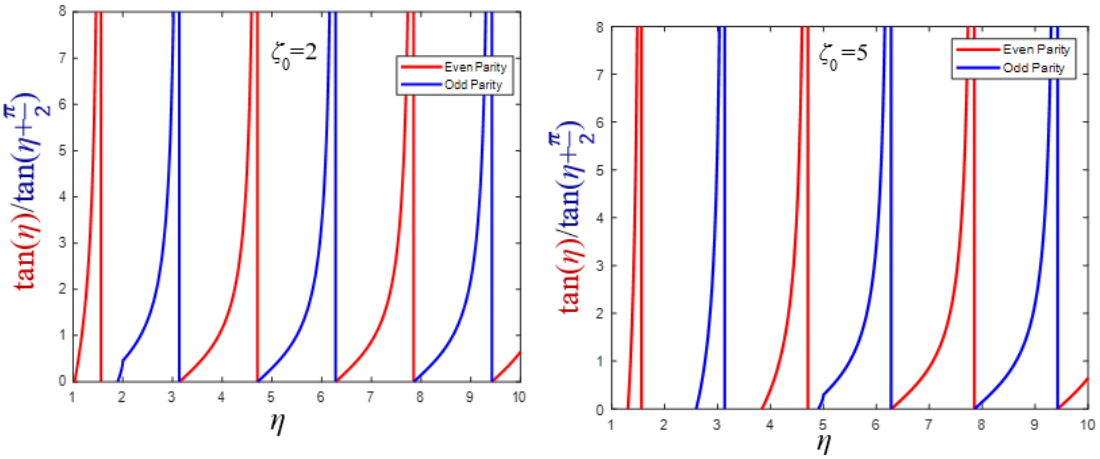

(c)

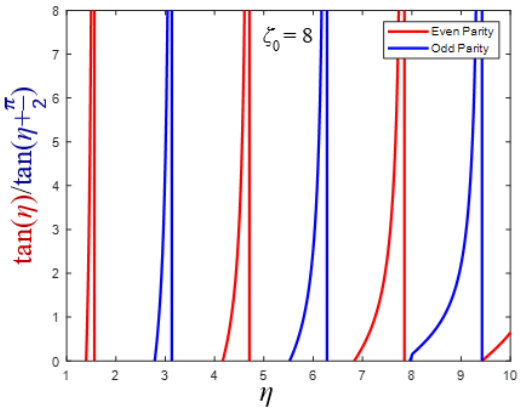

Figure. 3.7. Graphs of tan(η) for even parity solutions (shown in red) and *tan* ($\eta + \frac{\pi}{2}$) for odd parity solutions (shown in blue), plotted against η. The plots correspond to ζ_0 values of (a) 2, (b) 5& (c) 8.

In order to graphically solve the two given equations, we can overlay a plot of $\sqrt{\left(\frac{\zeta_0}{\eta}\right)^2 - 1}$ onto plots of $tan(\eta)$ and $tan\left(\eta + \frac{\pi}{2}\right)$ (the latter representing the negative cotangent function). As an illustrative example, consider an electron confined in a potential well with a width of 0.4 nm and a depth of 14eV. For these parameters, ζ_0 is computed to be

approximately 3.83. Fig.3.8 depicts the plot of $\sqrt{\left(\frac{\zeta_0}{\eta}\right)^2 - 1}$ for ζ_0 = 3.83 in conjunction with the aforementioned trigonometric functions. The points where the curves intersect, highlighted with red circles, represent the energy levels of the three bound states.

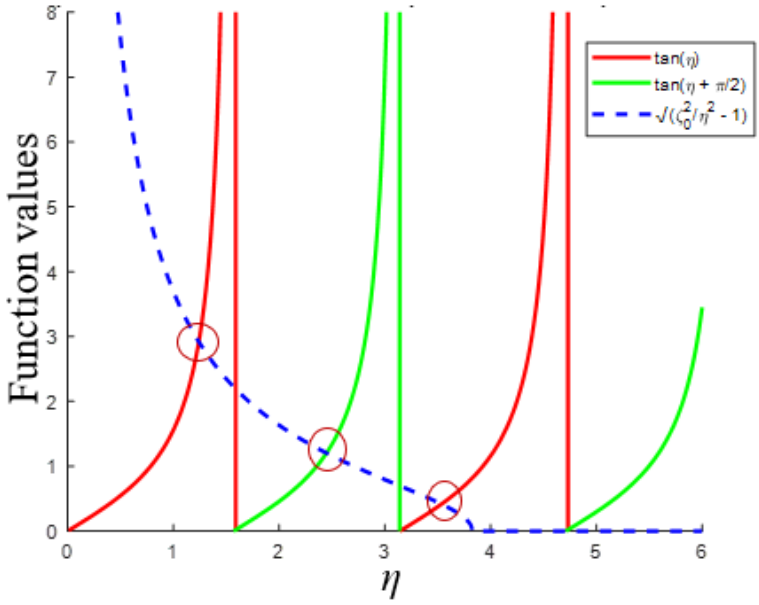

Figure.3.8. Graphical solutions of the transcendental equations for a finite potential well.

The parameter values for η are calculated based on the quantum numbers and their associated parities. The fundamental state, n = 1, exhibits even parity, resulting in η = 1.23. The first excited state, n = 2, exhibits odd parity and corresponds to η = 2.45. Lastly, the second excited state, n = 3, has even parity with η = 3.55. These η values directly correspond to specific energy eigenvalues of the quantum system. The energy eigenvalue for the fundamental state is E_1 = 1.46 eV, the first excited state has an energy eigenvalue of E_2 = 5.70 eV, and the energy eigenvalue for the second excited state is E_3 = 11.85 eV.

For a visual representation of these energy levels and their relation to the potential well, please refer to Fig.3.9.

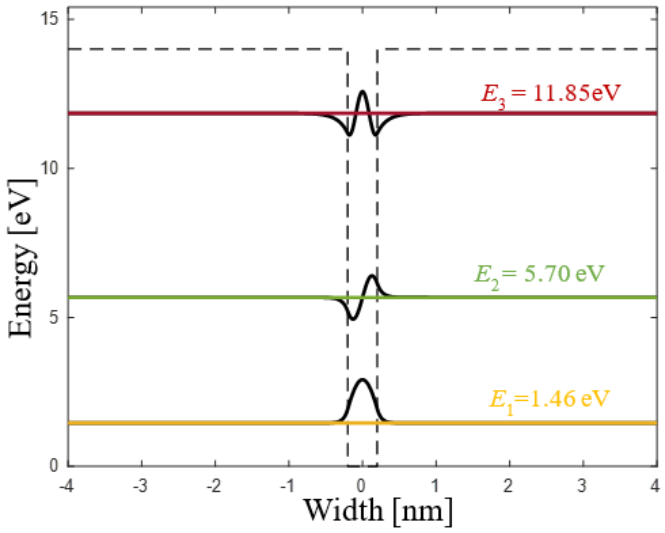

Figure.3.9. Depiction of three bound states inside a 1-dimensional finite potential well with a width of 0.4 nm and a depth of 14 eV. The wavefunctions are schematically represented in black.

An interesting feature to note is that the wavefunctions extend entirely into the regions of the potential well that are usually considered forbidden, thereby implying a non-zero probability of finding the particle even in these regions. This phenomenon is a consequence of quantum tunneling.

3.2.1 Discrete and continuum states

In quantum mechanics, particles can exist in two fundamental energy states: discrete and continuum.

Discrete states (bound states, energy eigenstates, or localized states): These states occur when a particle is confined within a potential well (e.g., an electron in an atom). The particle's energy is quantized, meaning it can only have specific allowed values. These states are represented by wave functions, which are finite sums of sine waves, with each wave corresponding to a distinct energy level. Visually, discrete state wave functions resemble standing waves with nodes and antinodes indicating the particle's probability distribution. Due to their quantized nature, discrete states play a crucial role in various fields like atomic physics (determining electron behavior) and quantum computing (manipulating qubit energy levels) [19,20,21].

Continuum states: These states are associated with unbound particles or systems with infinite energy levels. Unlike discrete states, the energy of a particle in a continuum state can take on any value within a continuous range. This is often the case for free particles (e.g., photons) that are not confined. In a finite potential well system, continuum states correspond to energies above the potential barrier where the particle is free to move. Continuum states are represented by wave functions as integrals of sine waves over all possible energies, reflecting the wide range of possible particle energies. They are often associated with unstable systems due to the potential for energy absorption or emission [19,20,21].

Fig. 3.10 illustrates the first three discrete states (n = 1, 2, 3) and the continuum in a one-dimensional potential well.

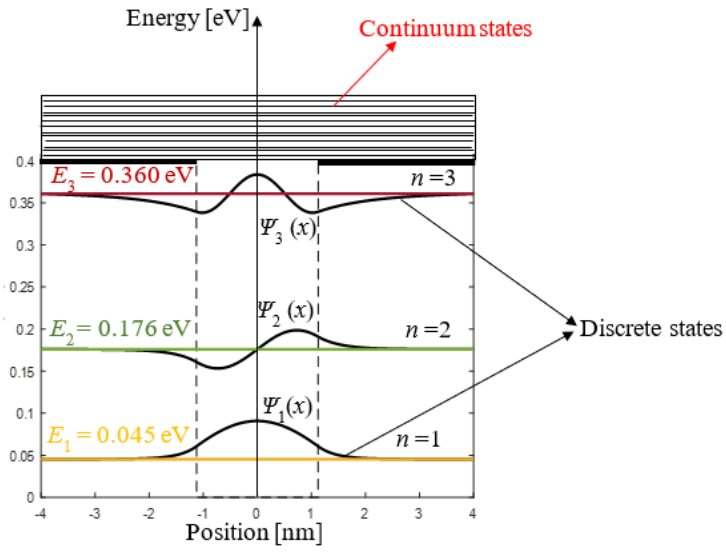

Figure.3.10. Depiction of a 1-dimensional potential well, highlighting the first three discrete states with their respective energy levels. Continuum states, represented by a continuous spectrum, are displayed above the potential well.

Understanding the distinction between discrete and continuum states is fundamental in quantum mechanics, as it underpins the behavior of particles across various physics fields.

3.3 Fano resonances of electromagnetic scattering on dielectrics or metallic objects

This section explores Fano resonances arising from the interaction of electromagnetic waves with nanostructures, contrasting them with those originating from purely quantum mechanical phenomena. We focus on deriving the scattering cross-section and examining how the Fano asymmetry parameter modulates the lineshape. In the realm of electromagnetic scattering, an object (metallic or dielectric) embedded within a dielectric medium exhibits an intriguing duality. The optical response of a material is determined by its dielectric constant. Such an object inherently possesses a non-radiative "dark mode" (discrete state) and a radiative "bright

mode" (continuum state). The theoretical framework for this investigation is based upon the methodology established by Gallinet & Martin [22].

Building upon a harmonic time dependency for the electric fields, we can express the frequency-dependent electric field *E* via the wave equation:

$$\varepsilon^{-1}(r,\omega)\nabla\times\nabla\times E(r,\omega)-\frac{\omega^2}{c^2}E(r,\omega) \qquad (3.8)$$

The Drude model furnishes pivotal insights into the scatterer's permittivity. Leveraging Maxwell's scaling law, a salient frequency-dependent differential operator, $\mathcal{M}_\omega$,can be defined:

$$\mathcal{M}_\omega E(r)=\frac{c^2}{\varepsilon(r,\omega)}\nabla\times\nabla\times E(r) \qquad (3.9)$$

Within this framework, the wave function of *E* is divided into essential bright and dark components. This division necessitates a pair of closely related equations:

$$(Q\mathcal{M}_\omega Q-\omega^2 I)Q|E=-Q\mathcal{M}_\omega P|E \qquad (3.10)$$

$$(P\mathcal{M}_\omega P-\omega^2 I)P|E=-P\mathcal{M}_\omega Q|E \qquad (3.11)$$

From this separation, a nonradiative mode, denoted $|E_d>$, is discerned, oscillating at a resonance frequency ω_d and endowed with an intrinsic damping, γ_d. Augmenting our understanding, the dyadic Green's function G_b renders a modified wave equation containing an embedded source term:

$$P|\tilde{E}\rangle=P|E_b\rangle+\frac{\langle E_d+\mathcal{M}_\omega P|\tilde{E}\rangle}{z_d^2-\omega^2}G_b P\mathcal{M}_\omega|E_d\rangle \qquad (3.12)$$

From an asymptotic perspective, the behavior of $|E>$ in remote fields corresponds seamlessly with $P|E_b\rangle$. Through a continuum, the Green's function is expanded as:

$$G_b = \frac{1}{2\pi}\int d^3\omega' \frac{|PE_b(\omega')\rangle\langle PE_b(\omega')|}{\omega'^2-\omega^2} \quad (3.14)$$

Focusing on resonance parameters, the intrinsic damping is encapsulated by:

$$\gamma_i = \frac{|\langle E_d|\mathcal{M}_\omega|PE_b|^2\gamma_d\omega_d}{\omega\left(\omega_d^2-\omega^2+\omega_d\triangle\right)^2} \quad (3.15)$$

The resonance width is subsequently characterized as:

$$\gamma = \frac{|\langle E_d|\mathcal{M}_\omega|PE_b|^2}{2\omega(1-\gamma_i)} \quad (3.16)$$

Significantly, the optical response is modulated by the interplay between bright and dark modes, encapsulated by:

$$\sigma = \frac{|\langle g|T|E\rangle|^2}{|\langle g|T|PE_b\rangle|^2} = a\frac{(\kappa+q)^2+b}{\kappa^2+1} \quad (3.17)$$

Figure 3.11 illustrates the scattering cross-section (defined by Equation (3.17)) for various values of the Fano asymmetry parameter (q) and the intrinsic loss parameter (b) that influences Fano resonances. These parameters shape spectral broadening and dampen the asymmetry.

Analogous to quantum mechanical interference, the scattering profile exhibits a symmetric resonance when the excitation of the discrete state (dark mode) is minimal (e.g., q = 0), as shown in Fig. 3.11(a). Conversely, a dominant continuous background excitation (bright mode) (e.g., q = 10000) leads to an almost perfectly symmetric peak, as depicted in Figure 3.11(c). In such cases, the Fano resonance can be interpreted as resembling a quasi-bound state in the

continuum (BIC). Notably, the screening parameter (*b*) has minimal influence on the scattering cross-section profile shape at high *q* values.

For intermediate values of *q*, such as *q* = 0.5, asymmetric peak profiles emerge, with the minimum reaching zero at $\epsilon = -q$, as demonstrated in Figure 3.11(b).

(a) (b)

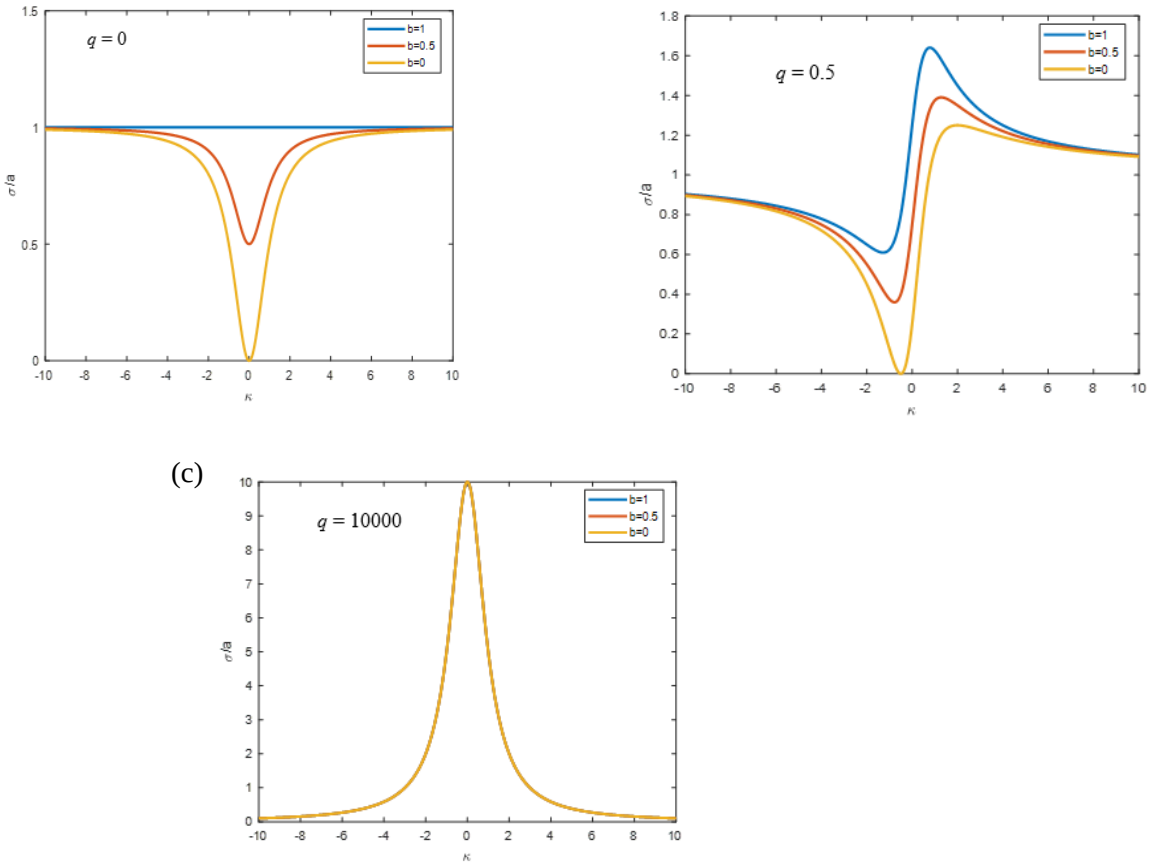

(c)

Figure.3.11. Resonance shape for the function σ/*a* as a function of the reduced frequency κ for different values of the asymmetry parameter *q* and the screening parameter *b*.

In the realm of plasmonic structures, intrinsic losses influence the resonance characteristics, whether in terms of width or contrast. These losses, combined with the overlap of the bright and dark modes,

govern the transparency and width of Fano resonances. Additionally, the transition operator, *T*, sheds light on the optical response to external excitation, providing insights into various physical processes, ranging from the local density of states to the reflectance of arrays.

3.3.1 Bright and dark modes in hybrid metasurfaces

Within the hybrid metasurface (Fig.3.12), nanopillars with mismatched radii lead to distinct resonant frequencies. Through hybridization, these collective lattice modes result in resonances that are either in-phase or out-of-phase with respect to each other or the incident wave [23, 24, 25]. The out-of-phase field configuration forms a subradiant (dark) mode, while the in-phase configuration leads to a superradiant (bright) mode.

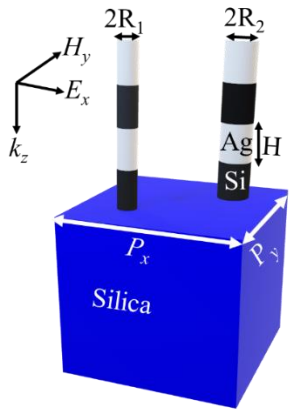

Figure.3.12. Schematic of the proposed hybrid metasurface under consideration, where the unit cell consists of two elements (nanopillars). Each element has four nanodisks: two plasmonic made of silver and two made of high-refractive-index material, silicon. The nanodisks are of height H = 120 nm and radii R_1 = 50 nm (fixed) and R_2, varied from 30 to 70 nm. The pairs are arranged in periodic array with periods $P_x = P_y = P$ = 550 nm

In the dark mode, electric fields in the two elements oscillate in opposite directions, resulting in a null net dipole moment (cancellation) and an extended lifetime. This configuration leads to destructive interference of radiated fields in the far-field zone, preventing coupling to free space radiation. Consequently, the dark mode becomes a "trapped" mode within the metasurface locality.

Conversely, the in-phase collective mode features oscillations in the same or opposite direction as the incident light wave for both elements. This leads to constructive interference in the far-field zone, forming a superradiant (bright) mode [25, 26].

The overlap of these out-of-phase and in-phase collective modes creates the sharp asymmetric Fano lineshapes observed in the wavelength-dependent characteristics of the array lattice scattering parameters, particularly near Rayleigh anomalies [24, 27].

To understand Fano resonance formation, we identify the subradiant and superradiant modes associated with Fano resonances in the absorption spectrum shown in Figure 4a for the binary array with radii R_1 = 50 nm and R_2 = 46 nm. Figures 3.13(b)–(g) illustrate the electromagnetic field distributions within the nanodisk cross-sections, providing insights into the Fano-resonance features. We plot the x-component of the electric field (E_x) distribution across the centers of the nanoantennas (z = 240 nm) for the unit cell containing two particles in the array (Figure 3.13).

First, we examine the electric field distributions at wavelengths of 900 nm and 883 nm around the nanoantennas of radii R_2 = 46 nm and R_1 = 50 nm. Figures 3.13(b), (c) show bright (superradiant) modes arising from constructive interference of the radiated fields from the two nanoantennas in the far field. Figure 3.13(d) illustrates the electric field distribution at a

wavelength of 889 nm, corresponding to the excitation of the out-of-phase field configuration, where the particles oscillate in opposite directions. Here, destructive interference of radiated fields in the far field leads to dark (subradiant) mode formation and a significant reduction in absorption.

As discussed, the overlap of superradiant and subradiant modes results in the formation of a sharp asymmetric Fano lineshape in the spectral absorption of the nanoantenna array. Figures 3.13(e)–(g) demonstrate the distributions of the *y*-components of the magnetic field at wavelengths of 889 nm, 900 nm, and 883 nm. We observe that the field remains unperturbed in this binary array, which agrees with the weak magnetic response typically associated with these nanostructures [23]

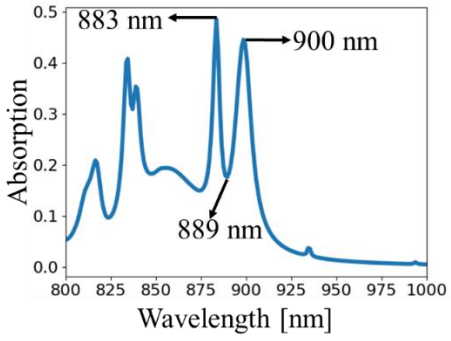

(a)

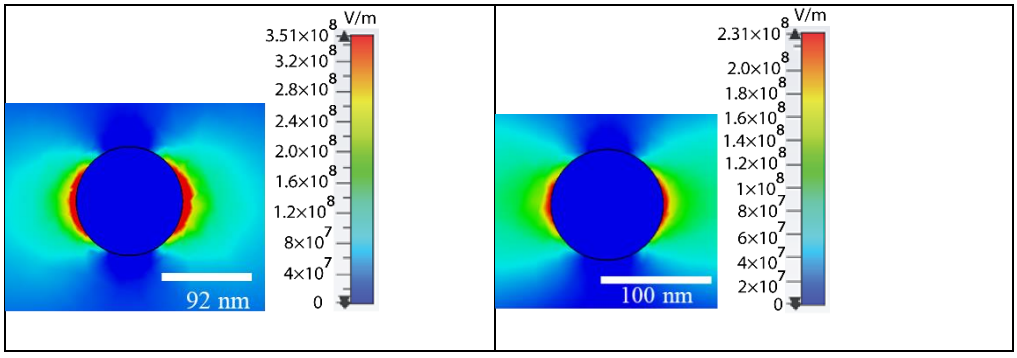

(b) (c)

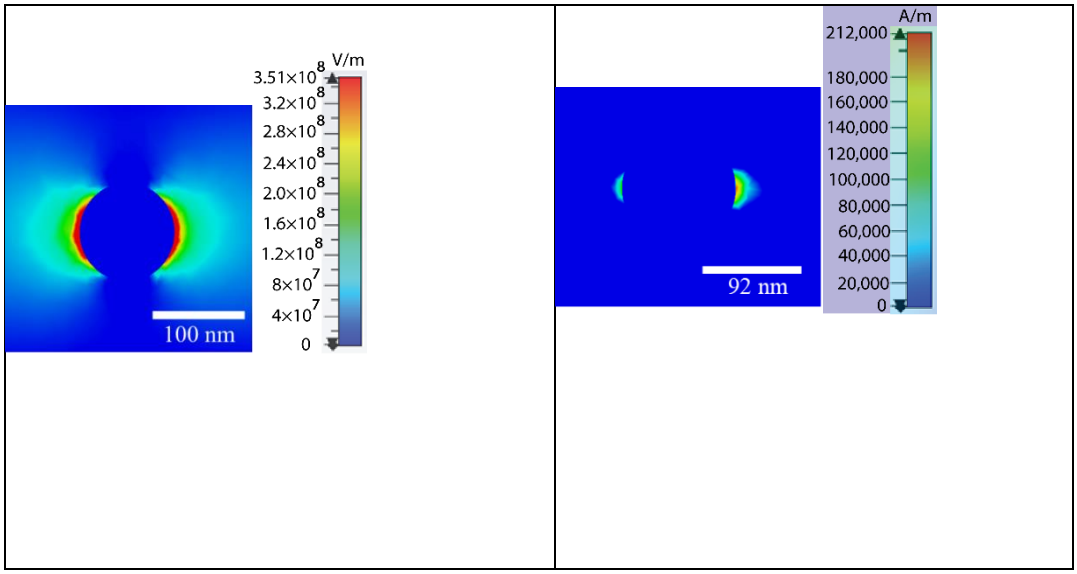

(d) (e)

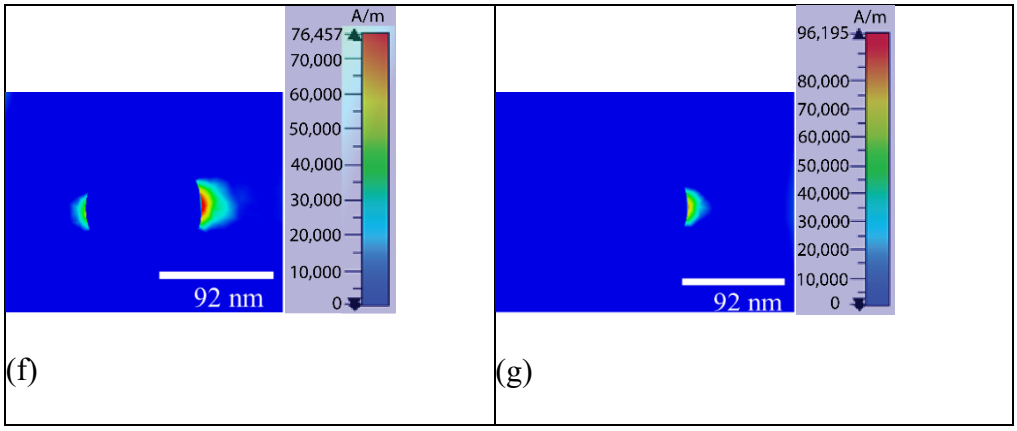

(f) (g)

Figure.3.13**.** Electric (E_x) and magnetic (H_y) field distributions outside the nanodisks with radii R_1 = 50 nm and R_2 = 46 nm. (**a**) Absorption spectra of nanoantenna with radius R_2 = 46 nm. (**b**) E_x ≅ at λ = 900 nm, z = 240 nm, in element #2. (**c**) E_x at λ = 883 nm, z = 240 nm, in element #1. (**d**) E_x at λ = 889 nm, z = 240 nm, in element #1. (**e**) H_y at λ = 889 nm, z = 240 nm, in element #2. (**f**) H_y at λ = 900 nm, z = 240 nm, in element #2. (**g**) H_y at λ = 883 nm, z = 240 nm, in element #2.

3.3.2 Mode coupling and Rabi splitting in hybrid metasurfaces

The unique properties of the metal interfaces with nanoscale light confinement enable new and exciting opportunities for fundamental studies and practical applications. High field localization and strong enhancement in plasmonic nanostructures can enhance light-matter interaction and their nonlinear response. The interaction of light with metals in nanostructures generates plasmonic excitations, which can be used in various nanophotonic applications, including more efficient sensing [28], nonlinear response [29], as well as photovoltaic and photocatalytic devices [30,31].

Two-dimensional optical nanostructures (metasurfaces) with subwavelength characteristic dimensions in both in- and out-of-plane directions have been shown to provide an exceptional ability to manipulate light and produce unique scattering features in spectral profiles. These properties have been employed as new platforms to control, confine, and enhance light-matter interactions in the nanostructures at the subwavelength level.

Metamaterial nanostructures that display Fano resonances have generated a considerable amount of growing interest by researchers in recent years [32-34]. Examples of such nanostructures include the ultrathin direct and Babinet-inverted metasurfaces made up of asymmetric split-ring nanoantennas or apertures fabricated in a metal plate, which produces high quality factor (high-*Q*) Fano resonances. The ability of Fano resonances to exhibit strong sensitivity to the local environment and their sharp asymmetric spectral profile play a very important role in designing and realizing photonic applications such as filters, sensors, modulators, lasers, optical switches, broadband reflectors, and various other devices [35,36].

Plasmonic metasurfaces, which are two-dimensional (2D), optically thin arrays of nanoantennas with subwavelength sizes distributed on a substrate, have shown to have an exceptional ability to manipulate light and produce unique scattering features in spectral profiles. The recent growing interest in plasmonic metasurfaces has been mainly driven by their small size, compared to their three-dimensional (3D) metamaterials counterparts, and their ability to control, confine, and enhance processes of light-matter interactions at the nanoscale.

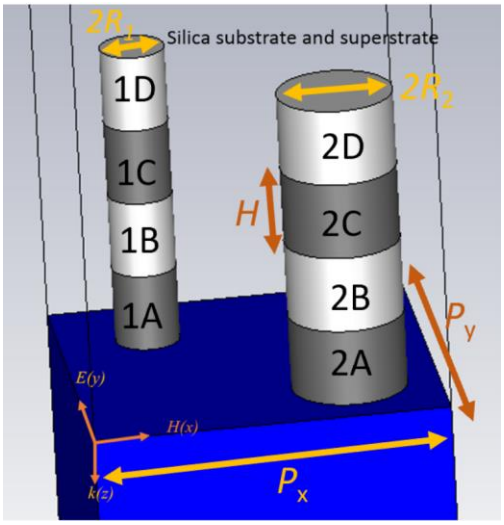

Figure 3.14. The geometry of structures under consideration, where the unit cell contains two nanoantennas, each consisting of four segments composed of alternating metal (silver) and semiconductor (silicon). The segment thickness is fixed at 120 nm. The array period in both *x* and *y* in-plane directions (unit cell size) is $P_x = P_y = 550$ nm. The dark grey shading on the sketch represents silicon, and the light grey represents silver. The nanoantennas have different radii R_1 and R_2, which allows for separate control of modes excited in each nanoantenna.

Figure 3.14 illustrates the transdimensional photonic lattice considered in this paper. Each nanopillar in the photonic lattice is engineered to support required resonances, including electric and magnetic dipoles, quadrupoles, and higher orders. It has been shown that the periodic arrangement of nanoantennas in the lattice results in significant changes in the array resonances compared to ones in a single nanopillar and is often associated with the excitation of additional

resonances, known as lattice resonances [37-39]. The resonances are mainly controlled by the nanopillar size, shape, inter-pillar distance, and material which requires three-dimensional engineering aiming at efficient excitation of nanopillar multipole resonances (Fig. 2).

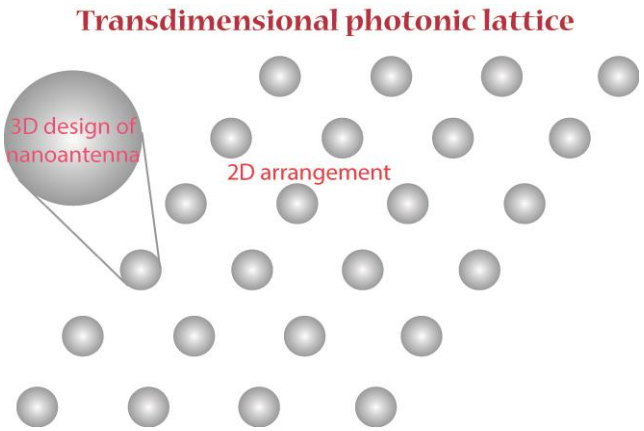

Figure 3.15 Top view of ultra-thin optical elements engineered based on transdimensional photonic lattices that include 3D-designed nanoantennas supporting multipole resonances and arranged in 2D arrays to enhance collective effects in the nanostructure.

Similar to the transdimensional lattices considered earlier [40,41], the nanoantennas investigated in this paper are arranged periodically on a common substrate. The metal and semiconductor elements are made of silver and silicon, and the nanoantenna array is placed over a silica substrate, with a silica superstrate cover. We use data from [15] to obtain the complex refractive indices of silver, silicon, and silica. The dimensions of the unit cell along the *x*- and *y*-directions are chosen to be $P_x = P_y = 550$ nm. Each segment of the considered nanostructures has the same thickness $H = 120$ nm, but with different nanopillar radii R_1 and R_2. Parameters of the structure and array can be scaled, and the effects of interest can be observed in another spectral range. However, the magnitude of the real part of metal permittivity should be comparable to the value of semiconductor permittivity, which is a common requirement for observation of plasmonic resonances. For this reason, we operate at the wavelength range $\lambda \approx$

800 – 900 nm, where $\mathrm{Re}[\varepsilon_{Ag}] \approx -40 \ldots -30$ and $\varepsilon_{Si} \approx 13.5$. That imposes limitations on the lattice period $P \leq \lambda/n_{sur} \approx 550$ nm. Numerical optimization of array parameters has shown that nanoantennas with radii $R = 30 – 80$ nm and segment thickness of 120 nm exhibit plasmonic resonances in the spectral range of 800 – 900 nm, and we choose these geometrical parameters for further analysis of the metasurfaces.

Full-wave numerical simulations have been carried out using the CST Microwave Studio software package with periodic boundary conditions set in the *x*- and *y*-directions. The multi-segment silver- and silicon- hybrid metasurface structure is illuminated by a plane wave polarized in the *y*-direction (electric field *E* along the *y*-axis), as shown in Fig. 3.14. Analysis of mode excitations in the multi-segment nanostructure shows that the transdimensional photonic lattices consisting of resonant nanoantennas in the engineered arrays have great potential to serve as functional elements in ultra-thin optical components and photonic devices, because of the strong coupling of modes facilitated by the lattice.

We design the transdimensional photonic lattice and study the different mode excitations in the multi-segment silver-silicon nanoantenna metasurfaces (Fig. 3.16). Plasmonic metasurfaces of various designs have been extensively studied both experimentally and theoretically, as these ultra-thin designs can support strong excitations of various multipole resonances at the nanoscale. For instance, Fano resonances in binary nanoparticle arrays (with two nanoantennas in the unit cell) have attracted a lot of attention and have been experimentally realized in the visible region. The nanostructures of complex shapes, such as dolmens and oligomers of nanoparticles as well as plasmonic clusters, have shown to exhibit Fano resonances in the optical spectral range, and therefore we choose the design of multi-segment nanoantennas

arranged into the periodic array and resonances excited at the wavelength comparable to lattice period.

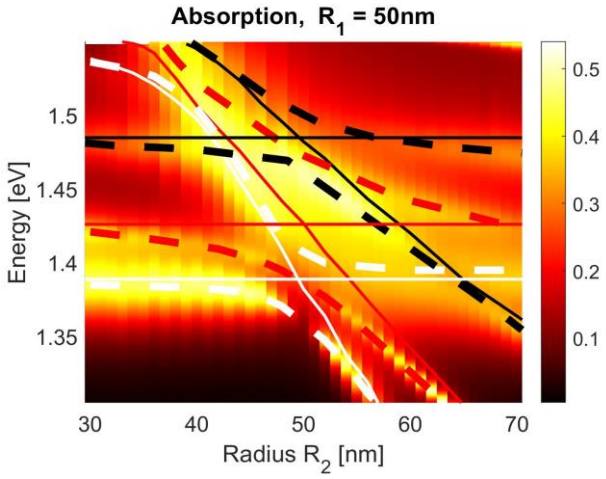

Figure 3.16. Modes in the nanostructure: absorption in the entire structure is analyzed to track mode positions and their strength upon changes of the nanoantenna coupling. The radius of one nanoantenna is fixed to R_1 = 50 nm, and the radius of the second nanoantenna is varied as shown in the plot. The color map indicates absorption in the structure. Solid and dashed lines indicate modes excited in the array without and with nanoantenna coupling through the lattice, respectively.

Rabi splitting occurs upon strong interaction between nanostructure modes. In particular, the coupling strength between two nanoresonators needs to exceed the system dissipation with the coherent energy exchange between coupled elements. Comparing solid and dashed lines in Fig. 3.16, one can see that in the case of interacting nanoantennas coupled through the lattice, modes do not cross but rather are split by about 0.05 eV. We also notice the destructive interference of the modes when the radii of the nanoantennas are the same and kept at 50 nm. Outside of this range (when R_1 is fixed at 50 nm, while R_2 is varied), resonant excitations are observed due to the constructive coupling between resonant dark and bright modes.

Fano resonances observed in the nanostructures under consideration arise from the interaction of resonant dark modes and the corresponding bright modes of the multiple metal-dielectric interfaces in the nanostructures (Fig. 3.16). We observe the resonant response of plasmonic-semiconductor hybrid metasurface using full-wave modeling of mode coupling facilitated by the interaction of nanoantennas in the array and their coherent lattice scattering. We analyze field enhancement inside each segment in the nanostructure to identify the origin of the modes and their energy change with variations of the nanoantenna radius. From Fig. 3.17, one can see that the field enhancement in silver is several times larger than in silicon. Furthermore, comparing changes of mode energy in different nanoantennas (radius R_1 or R_2, Fig. 3.19), we see that field enhancement in the nanoantenna with R_2 is larger and mode shifts to lower energy with the increase of the radius R_2.

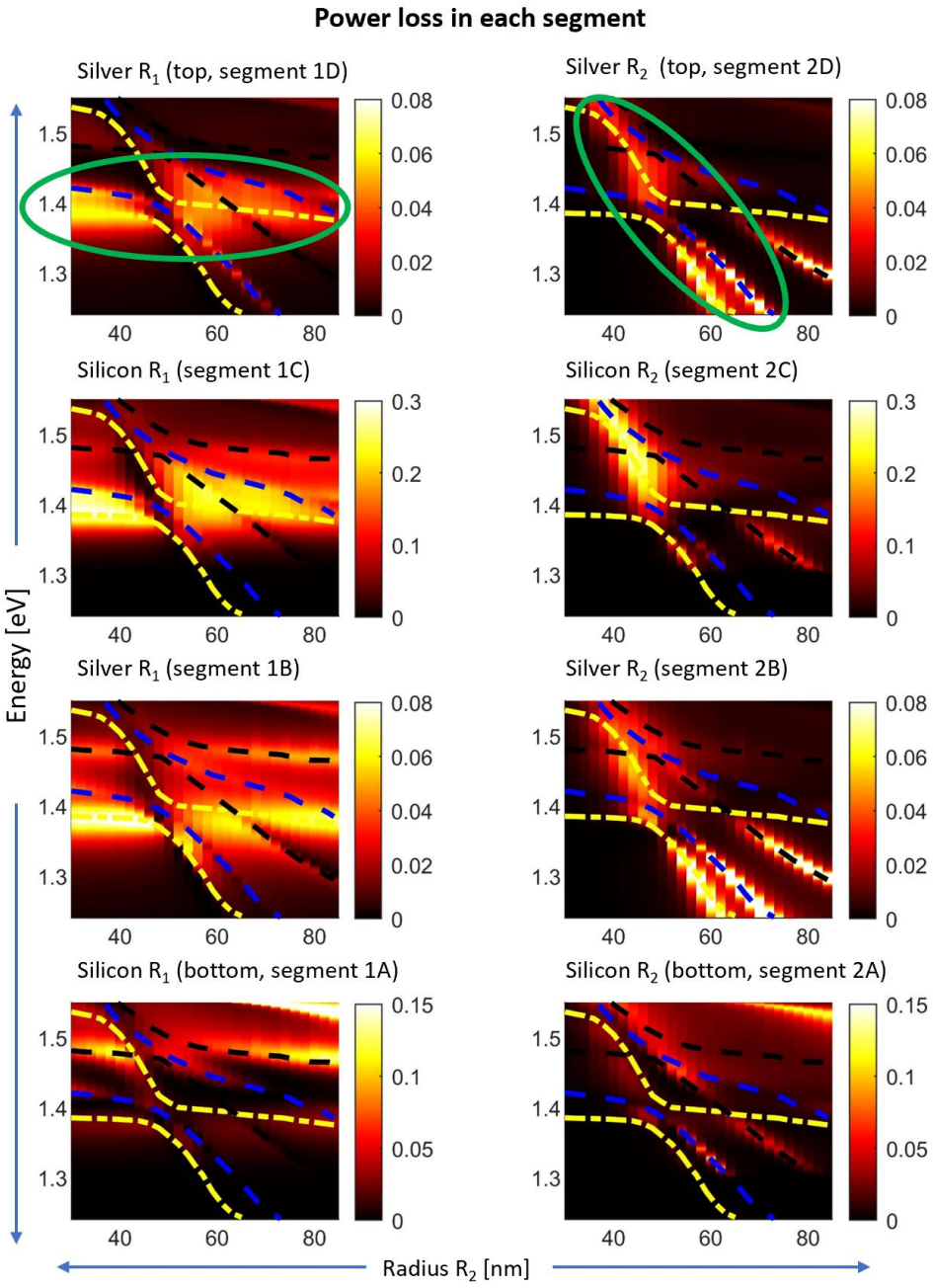

Figure 3.17. Excitation of different nanostructure modes with respect to power loss in each segment: (left row) segments in the nanoantennas with radius R_1, (right row) segments in the nanoantennas with radius R_2. We analyze the nanostructure modes, resonances, and field enhancement in the photonic lattice with $P_x = P_y = 550$ nm, $H = 120$ nm, $R_1 = 50$ nm, and R_2 varied from 30 to 84 nm. The color map indicates the magnitude of power loss in each structure element. The dashed lines indicate modes excited in the array with nanoantenna coupling through the lattice. The energy of maximum power loss in the segments corresponding to R_1 remains approximately the same (green oval on the left-hand side). In contrast, as R_2 changes, the excitations in the nanoantenna with radius R_2 also shift (green oval on the right-hand side).

In summary, we have considered plasmonic-semiconductor hybrid metasurfaces with a tunable resonant response. We designed scattering elements out of multi-segment metal-semiconductor nanostructures, and we studied periodic arrays of such scatterers. We aimed at designing efficient directional scatterers and their arrays for ultra-thin optical components, such as metasurfaces and transdimensional photonic lattices. The Fano resonances in our metasurfaces originate from the interaction of bright modes and dark modes that give rise to asymmetric linewidth profiles in the scattering characteristics, such as absorption or reflection spectra. We show that a slight mismatch in the resonance positions controlled by the scatterers' size results in Rabi splitting, observed as changes in peak positions and characteristic asymmetric spectral profiles. Our structure will enable the excitation of multi-resonances in the visible and near-infrared regimes, with tunable resonances originating from plasmonic nanopillars and their periodic structuring.

(a)

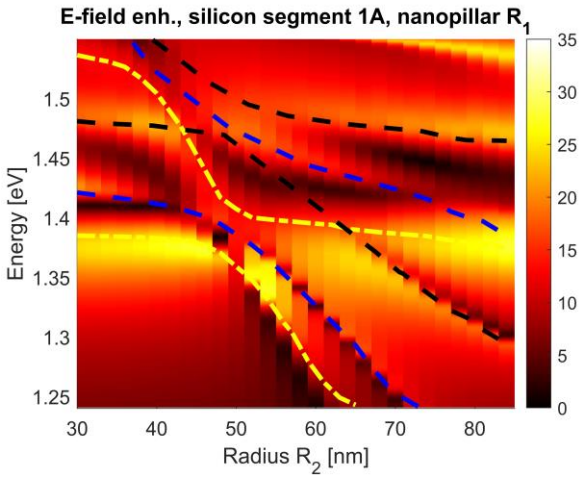

(b)

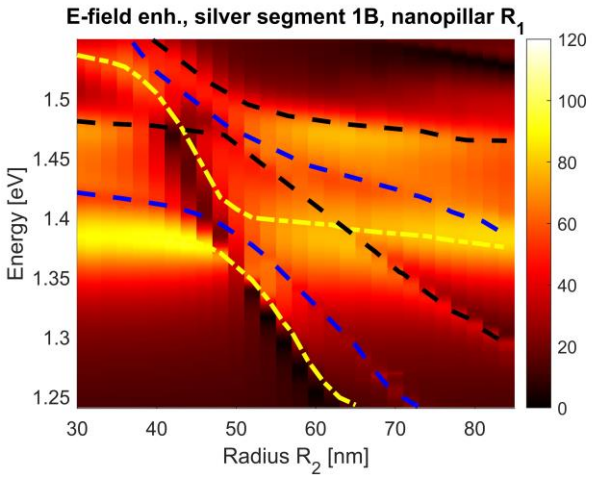

Figure 3.18 Field enhancement in (a) silicon 1A and (b) silver 1B segments of the nanopillar with radius R_1. The radius of one nanoantenna is fixed at R_1 = 50 nm, and the radius of the second nanoantenna is varied, as shown in the plot. The *E*-field probes are positioned in the bottom segment. Color map indicates field enhancement at the central point of each element in the structure. Dashed lines indicate modes excited in the array, with nanoantenna coupling through the lattice.

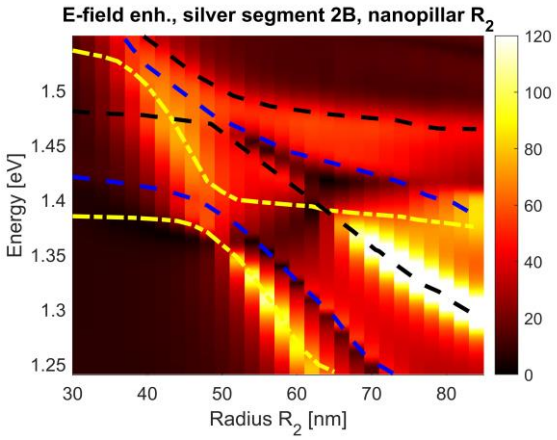

Figure 3.19. Field enhancement in the silver segment 2B of the nanopillar with radius R_2. The radius of one nanoantenna is fixed at R_1 = 50 nm, and the radius of the second nanoantenna is varied, as shown in the plot. The *E*-field probe is positioned in the bottom segment 2B. One can see a strong excitation of modes at the lower energy and their shift corresponding to varying R_2.

3.4 References

[1] U. Fano, "Effects of configuration interaction on intensities and phase shifts," Physical Review, 124(6), 1866–1878 (1961).

[2] Y. S. Joe, A. M. Satanin, & C. S. Kim, "Classical analogy of Fano resonances," *Physica Scripta*, 74(2), 259–266 (2006).

[3] A. E. Miroshnichenko, S. Flach, & Y. S. Kivshar, "Fano resonances in nanoscale structures," Reviews of Modern Physics, 82(3), 2257–2298 (2010).

[4] B. Luk'yanchuk et al., "The Fano resonance in plasmonic nanostructures and metamaterials," Nature Materials, 9(9), 707–715 (2010).

[5] W. Park, "Optical interactions in plasmonic nanostructures," Nano Convergence, 1(1), 2 (2014).

[6] A. B. Khanikaev, C. Wu, & G. Shvets, "Fano-resonant metamaterials and their applications," Nanophotonics, 2(4), 247–264 (2013).

[7] W. Zhou et al., "Progress in 2D photonic crystal Fano resonance photonics," Progress in Quantum Electronics, 38(1), 1–74 (2014).

[8] F. Le et al., "Metallic nanoparticle arrays: a common substrate for both surface-enhanced Raman scattering and surface-enhanced infrared absorption," ACS Nano, 2(4), 707–718 (2008).

[9] A. A. Yanik et al., "Seeing protein monolayers with naked eye through plasmonic Fano resonances," Proceedings of the National Academy of Sciences of the United States of America, 108(29), 11784–11789 (2011).

[10] E. Semouchkina et al., "Sensing based on Fano-type resonance response of all-dielectric metamaterials," Sensors, 15(4), 9344–9359 (2015).

[11] A. E. Miroshnichenko & Y. S. Kivshar, "Fano resonances in all-dielectric oligomers," Nano Letters, 12(12), 6459–6463 (2012).

[12] M. Pu et al., "Fano resonance induced by mode coupling in all-dielectric nanorod array," Applied Physics Express, 7(3), 032002 (2014).

[13] M. Song et al., "Sharp Fano resonance induced by a single layer of nanorods with perturbed periodicity," Optics Express, 23(3), 2895–2903 (2015).

[14] J. Zhang, K. F. MacDonald, & N. I. Zheludev, "Near-infrared trapped mode magnetic resonance in an all-dielectric metamaterial," Optics Express, 21(22), 26721–26728 (2013).

[15] F. Zhang et al., "Fano resonance of an asymmetric dielectric wire pair," Applied Physics Letters, 105(17), 172901 (2014).

[16] D. R. Abujetas et al., "Spectral and temporal evidence of robust photonic bound states in the continuum on terahertz metasurfaces," Optica, 6, 996-1001 (2019).

[17] Y. Wang et al., "Efficient excitation and tuning of multi-Fano resonances with high Q-factor in all-dielectric metasurfaces," Nanomaterials (Basel), 12(13), 2292 (2022).

[18] N. Zettili, “Quantum Mechanics: Concepts and Applications (2nd ed.)”, John Wiley & Sons.

[19] D. J. Griffiths, “Introduction to quantum mechanics”, Pearson Education Limited (2012).

[20] B. H. Bransden & C. J. Joachain, “Physics of atoms and molecules”, Longman (2003).

[21] R. Shankar, “Principles of quantum mechanics”, Springer (2008).

[22] B. Gallinet & O. J. F. Martin, "Ab initio theory of Fano resonances in plasmonic nanostructures and metamaterials," Physical Review B, 83(23), 235427 (2011).

[23] W. Zhao, X. Leng, & Y. Jiang, "Fano resonance in all-dielectric binary nanodisk array realizing optical filter with efficient linewidth tuning," Optics Express, 23, 6858-6866 (2015).

[24] D. E. Gómez et al., "The dark side of plasmonics," Nano Letters, 13, 3722–3728 (2013).

[25] W. Zhao et al., "Fano resonance based optical modulator reaching 85% modulation depth," Applied Physics Letters, 107, 171109 (2015).

[26] W. Zhao et al., "Dipole and quadrupole trapped modes within bi-periodic silicon particle array realizing three-channel refractive sensing," Optics Express, 22, 31277–31285 (2014).

[27] D. Bosomtwi, M. Osiński, & V. E. Babicheva, "Lattice effect for enhanced hot-electron generation in nanoelectrodes," Optical Materials Express, 11, 3232–3244 (2021).

[28] A. B. Evlyukhin et al., "Detuned electrical dipoles for plasmonic sensing," Nano Letters, 10, 4571–4577 (2010).

[29] A. Han et al., "Second harmonic generation in metasurfaces with multipole resonant coupling," Nanophotonics, Advance online publication (2020).

[30] H. A. Atwater & A. Polman, "Plasmonics for improved photovoltaic devices," Nature Materials, 9, 205–213 (2010).

[31] S. V. Zhukovsky et al., "Giant photogalvanic effect in noncentrosymmetric plasmonic nanoparticles," Physical Review X, 4, 031038 (2014).

[32] M. F. Limonov et al., "Fano resonances in photonics," Nature Photonics, 11, 543–554 (2017).

[33] W. Y. Zhao, D. Q. Ju, & Y. Y. Jiang, "Sharp Fano resonance within bi-periodic silver particle array and its application as plasmonic sensor with ultra-high figure of merit," Plasmonics, 10, 469–474 (2015).

[34] A. A. Bogdanov et al., "Bound states in the continuum and Fano resonances in the strong mode coupling regime," Advanced Photonics, 1, 016001 (2019).

[35] Z. G. Liu et al., "Fano resonance Rabi splitting of surface plasmons," Scientific Reports, 7, 8010 (2017).

[36] A. B. Evlyukhin et al., "Collective resonances in metal nanoparticle arrays with dipole-quadrupole interactions," Physical Review B, 85, 245411 (2012).

[37] S. Baur, S. Sanders, & A. Manjavacas, "Hybridization of lattice resonances," ACS Nano, 12, 1618-1629 (2018).

[38] V. E. Babicheva & J. V. Moloney, "Lattice Zenneck modes on subwavelength antennas," Laser & Photonics Reviews, 13, 1800267 (2019).

[39] V. E. Babicheva, "Multipole resonances in transdimensional lattices of plasmonic and silicon nanoparticles," MRS Advances, 4, 713-722 (2019).

[40] H. Ahmed & V. E. Babicheva, "Nanostructured tungsten disulfide WS2 as Mie scatterers and nanoantennas," MRS Advances, Advance online publication (2020).

41. Refractive Index Database. (n.d.). Retrieved from https://refractiveindex.info/

Chapter 4

Contents

4.0 Bound states in the continuum (BICs)

The confinement and propagation of waves, from electrons orbiting atoms to light transmission in optical fibers, are fundamental principles governing a vast array of phenomena in both natural and engineered systems [1-4]. A captivating concept at this crossroads is the phenomenon known as Bound States in the Continuum (BICs). BICs defy conventional wisdom by representing wave modes that remain localized and non-radiative, even while existing within a continuous frequency spectrum where radiation would normally occur [5-8]. This counterintuitive behavior arises primarily from destructive interference. When waves within a system overlap in a specific manner, they can either amplify or cancel each other out. In BICs, precise cancellations – governed by factors like system geometry, material properties, and boundary conditions – ensure that what should radiate remains perfectly confined. This confinement is so pronounced that BICs often exhibit infinitely high Q-factors, a measure of resonance quality, further highlighting their unique and powerful nature in wave-based applications [9, 10].

Introduced by von Neumann and Wigner in 1929 within the realm of quantum mechanics, BICs initially remained a theoretical curiosity [11]. However, scientific advancements have led to their observation across various wave systems, encompassing acoustics, optics, and even electronics. The field of optics, in particular, has witnessed significant breakthroughs driven by BICs. Harnessing these perfectly confined wave modes with their exceptional Q-factors has paved the way for advancements in lasers, sensors, and communication technologies, ushering in a new era of innovation [12-16].

This chapter delves into potential engineering of BICs in section 4.1, as originally proposed by von Neumann and Wigner and further elaborated by Stillinger and Herrick [11, 17]. We begin by exploring the transition from the principles of quantum mechanics to the realm of optics and photonics, highlighting the parallels between these two domains. By emphasizing how concepts developed in quantum physics have found profound applications in optics, this comparative analysis underscores the impact of BICs on advanced optical devices and bridges the gap between theoretical concepts and their practical applications in cutting-edge technologies [17].

The chapter then focuses on photonic BICs within periodic photonic structures. We discuss their properties and applications in photonics, including an overview of one-dimensional photonic crystal structures and their operating regimes as depicted in dispersion relation plots (Section 4.2.1). Furthermore, Section 4.2.2 delves into the theory and analysis of the Friedrich and Wintgen (FW) BIC model, a significant framework for understanding accidental BICs in photonic systems.

Section 4.3 explores the concept of BICs in dielectric gratings and their implications for wave manipulation, leading to the formation of symmetry-protected (SP) BICs.

Finally, the chapter concludes by exploring the observation of multiple quasi-BICs in hybrid photonic structures resulting from strong coupling between hybridized quasi-BICs (Section 4.4).

4.1 Bound states in the continuum (BICs) through potential engineering: the von Neumann-Wigner method

The phenomenon of bound states in the continuum (BICs) presents a captivating anomaly in quantum mechanics. These localized states exist within a continuous spectrum, defying the norm by remaining confined despite having energies that fall within the continuum of extended states [5, 6, 7].

The theoretical concept of BICs was first introduced by John von Neumann and Eugene Wigner in 1929. Their investigation explored the possibility of discrete eigenvalues (quantized energy levels) existing within the continuous energy spectrum, without the usual decay characteristics associated with such energies.

von Neumann and Wigner demonstrated that BICs could be formed through careful manipulation of the potential energy landscape. Specifically, they showed that certain potentials, even if they decay at infinity, can lead to the formation of BICs [7]. This theoretical exploration is based upon the methodologies established by Stillinger and Herrick [7], as well as the work of Hsu *et al*. [5, 9].

The existence of BICs hinges on the condition:

$V(r) \to 0$ as $r \to \infty$, where, r signifies the radial distance.

The governing equation for a single-particle system in quantum mechanics is the Schrödinger equation, written as:

$$\left(-\frac{\hbar^2}{2m}\nabla^2 + V(r)\right)\psi(r) = E\psi(r) \qquad (4.1)$$

On translating to reduced units, equation (4.1) becomes:

$$\left(-\frac{1}{2}\nabla^2 + V\right)\psi = E\psi \qquad (4.2)$$

This equation can be further expressed as:

$$V = E + \frac{\nabla^2\psi}{2\psi} \qquad (4.3),$$

Here, V represents a confining potential that remains finite as the radial distance (r) approaches infinity, while ψ denotes the wavefunction of the target bound state in the continuum (BIC). It's important to note that the energy (E) for scattering states lies within the positive domain (E > 0).

To realize the desired BIC, careful optimization of the potential V(r) and energy E is crucial. This ensures that the potential approaches zero as the radial distance tends to infinity (lim V(r) $\rightarrow$ 0 as r $\rightarrow \infty$). The specific solution to equation (4.3) proposed by von Neumann and Wigner [5, 9] for BIC formation is given by:

$$\psi(\boldsymbol{r}) = f(r)sin(kr)/kr \qquad (4.4), \text{ with } \quad f(r) = \{A^2 + [2kr - \sin(2kr)]^2\}^{-1}.$$

In this context, *A* is a distinct non-zero constant, and the associated energy eigenvalue is defined as $E=\frac{1}{2}k^2$. This energy is embedded within the continuous spectrum $E \geq 0$, and that $V = 0$.

Adopting the parameters, $A = 25$, $k = \sqrt{8}$, and $E = 4$, and utilizing equations (4.3) and (4.4), we showcase the potential V(r) alongside the bound wave function $\psi(\boldsymbol{r})$ in Fig. 4.1

(a) (b)

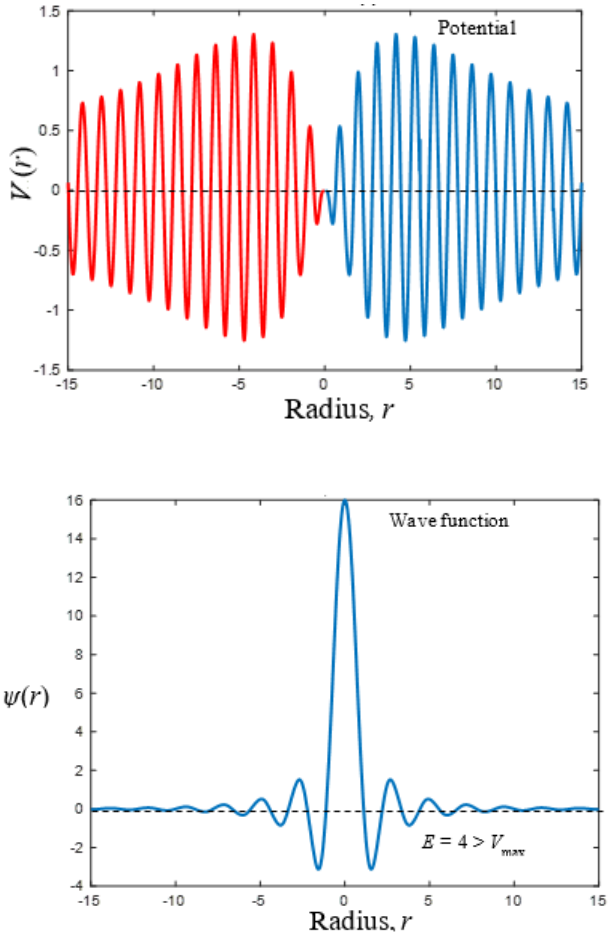

Figure .4.1. Illustration of the Bound State in the Continuum (BIC) as introduced by von Neumann and Wigner. (a) A potential-energy function. (b) Wave function (BIC) having its energy embedded within the continuous spectrum of extended states.

This section explores the critical conditions for engineering bound states in the continuum (BICs) through potential manipulation. A key requirement is that the potential energy, V(r), approaches zero as the radial distance (r) tends to infinity (lim V(r) → 0 as $r \to \infty$). Consider

an energy level E = 4 residing within the continuous spectrum, exceeding the peak potential value (V_{max}). By carefully manipulating the potential, we can successfully create a bound state within this continuum, characterized by a narrow resonance and a high *Q*-factor (Fig. 4.1(b)) [9].

The concept of BICs can be approached from a reconstruction perspective, focusing on specific wavefunctions. A BIC mode represents the confinement of a wave even when its energy surpasses that of the surrounding medium (background potential). This confinement implies that the wave's amplitude diminishes to zero in specific directions as it extends towards infinity, while remaining free to propagate in other directions. For example, a BIC present in the *z*-direction signifies that $\psi(z)$ approaches zero as z approaches positive or negative infinity ($\psi(z) \rightarrow 0$ as $z \rightarrow \pm\infty$), given that $\omega > ck_0$ (where k_0 is the free-space wavevector).

To qualify as a BIC mode, several criteria must be met:

Finite Extent: The structure containing the BIC mode must possess a finite extent in the direction where the BIC is confined.

High Energy: The energy of the BIC mode should exceed the potential of the background medium ($\omega > ck_0$).

Zero Amplitude at Infinity: In the direction of BIC confinement, the wave's amplitude needs to tend towards zero at infinity. Mathematically, for all real values of k_z, $\psi(z)$ approaches zero as *z* approaches positive or negative infinity ($\psi(r) \rightarrow 0$ as $r \rightarrow \pm\infty$).

In essence, a BIC mode requires a structure with a confined boundary, an energy higher than the background potential, and a wave amplitude that diminishes as it extends infinitely in the

confinement direction. This collective framework defines the unique nature of BICs within various physical systems [9, 18].

4.2 Bridging the gap: quantum mechanics and photonic BICs

This section draws parallels between the formulation of photonic BICs and the foundational principles of quantum mechanics. We will explore this connection through the lens of a one-dimensional quantum well. A quantum well exhibits translational symmetry along the *z*-direction, meaning its properties remain consistent in that direction while potentially varying in others (e.g., *x* and *y*). This uniformity in *z* is depicted in Figure 4.2 (left panel). An analogous optical system is a parallel-plate dielectric waveguide, showcased in the right panel of Figure 4.2. This analysis aligns with the work presented by [17].

By adapting the Helmholtz equation into the format of the stationary Schrödinger equation, we can demonstrate that the permittivity ε(x) (see Equation 4.5) has an analogous role to the quantum mechanical potential, $U(x)$ (see Equation 4.8). Modes of the optical waveguide situated below the light line ($\omega < ck_z$) correspond to discrete states, while those above ($\omega > ck_z$) span the continuum (see the right side of Figure 4.2). In structures with translational symmetry or periodicity along a specific axis, BICs are confined strictly to orthogonal directions. The comparison between quantum systems and their photonic counterparts offers a valuable conceptual framework, although it is not a perfect analogy.

To illustrate this concept, we consider a planar dielectric waveguide oriented along the x-axis, characterized by permittivity $\varepsilon(x)$. We will derive the Helmholtz equation into the format of the stationary Schrödinger equation (see Equation 4.8). It is important to note that the waveguide can support both transverse electric (TE) and transverse magnetic (TM) modes.

However, for brevity, we will primarily focus on TE modes. For TE modes, the electric field (*E*) has a single component along the *y*-axis and is influenced by both *x* and *z* (representing the propagation direction) [19]. The temporal oscillations of the fields are conventionally described using harmonic modes with a phase factor $e^{-i\omega t}$ [11]. Therefore, our examination will primarily focus on the spatial fluctuations of the fields. Drawing from Maxwell's equations, the relevant equations for TE modes include:

1. $\frac{\partial H_z}{\partial x} = -i\omega\varepsilon E_y$

2. $\frac{\partial E_y}{\partial x} = i\omega\mu H_z$

From the second equation:

$$H_z = -\frac{i}{\omega\mu}\frac{\partial E_y}{\partial x}$$

Substituting this into the first equation gives:

$$\frac{\partial^2 E_y}{\partial x^2} = \omega^2\mu\varepsilon E_y$$

Now, since ε is a function of *x*, we can write it as $\varepsilon = \varepsilon_0 + \triangle\,\varepsilon(x)$ where ε_0 is the average permittivity and $\triangle\,\varepsilon(x)$ is the variation about this average.

Using this in the above equation, we get:

$$\frac{\partial^2 E_y}{\partial x^2} = \omega^2\mu\varepsilon_0 E_y + \omega^2\mu\,\triangle\,\varepsilon(x)E_y$$

The propagation constant β is related to ω as $\beta = \omega\sqrt{\mu\varepsilon_0} = {}^{\omega}/_{c}$ where c is the light speed in the medium (free space) defined by ε_0 .

This can be further written as:

$$\frac{\partial^2 E_y}{\partial x^2} + \beta^2 E_y = \omega^2 \mu \triangle \varepsilon(x) E_y$$

Given that the mode propagates in the *z*-direction with k_z, the total wavevector *k* in the material is given by $k^2 = \beta^2 + k_z^2$. For a guided wave, k_z is real and $k_z^2 = {\omega^2}/{c^2} - \beta^2$.

Thus, the equation can be written as:

$$\nabla^2 E_y + \left({\omega^2}/{c^2}\right) E_y = \left({\omega^2}/{c^2}\right)[1 + \mu \triangle \varepsilon(x)/\varepsilon_0] E_y$$

Rearranging and focusing on the *x*-dependence gives:

$$-\frac{\partial^2 E_y}{\partial x^2} + \left({\omega^2}/{c^2}\right)[1 - \varepsilon(x)] E_y = \left({\omega^2}/{c^2} - k_z^2\right) E_y \qquad (4.5).$$

We will now analyze to derive an analogous expression for a 1-D quantum well with translational symmetry along the z-axis, replacing the Helmholtz wave equation with the Schrödinger equation.

1. We consider a 1-D quantum well along the *x*-direction, with the system exhibiting translational symmetry along the z-axis.

2. The well features a periodic potential denoted by *U*(*x*), dependent solely on the *x*-coordinate.

3. The particle under consideration possesses mass *m*.

For a system with translational symmetry along the *z*-axis, we define the domain of the continuum spectrum [17] as:

$$E_c = E - \frac{\hbar^2 k_z^2}{2m} \qquad (4.6).$$

Where $E_c = E - \frac{\hbar^2 k_z^2}{2m} > 0$ and $E_z = \frac{\hbar^2 k_z^2}{2m}$ represents the kinetic energy of the particle in the z-direction.

The basic time-independent Schrödinger equation in one dimension for such a system is given by [17,20]:

$$-\frac{\hbar^2}{2m}\frac{d^2\psi}{dx^2} + U(x)\psi = E_c\psi \qquad (4.7)$$

Reformulating equation (4.7) using equation (4.6), we get:

$$-\frac{\hbar^2}{2m}\frac{d^2\psi}{dx^2} + U(x)\psi = \left(E - \frac{\hbar^2 k_z^2}{2m}\right)\psi \qquad (4.8)$$

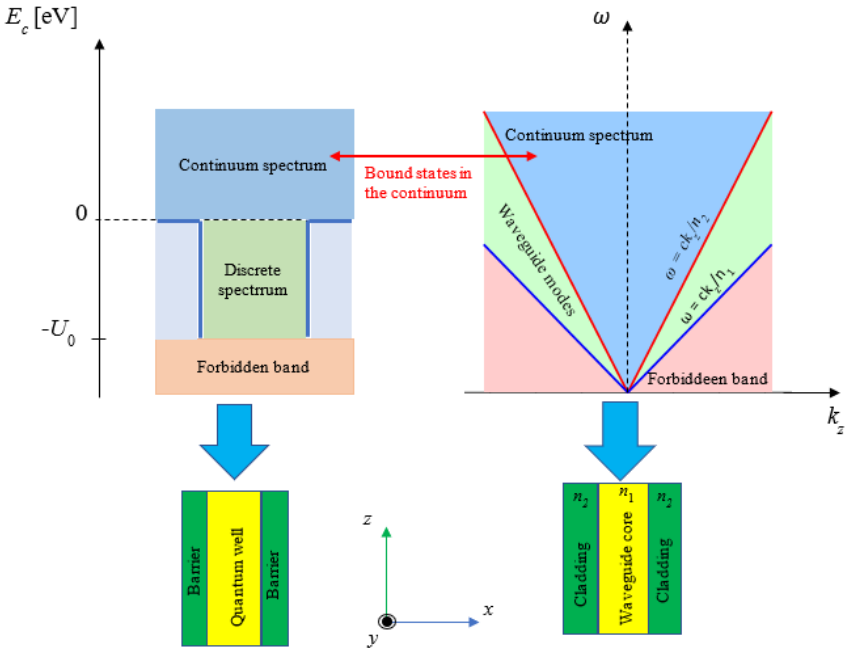

Fig.4.2. An equivalence exists between quantum mechanical and electromagnetic phenomena for a one-dimensional potential with translational symmetry along the z-axis. At the top, we have the Schrodinger equation for a 1D quantum well and the Helmholtz equation for a planar dielectric waveguide illustrated. The middle

sections demonstrate the potential well (to the left) and the dispersion diagram (to the right). The bottom visuals represent the potential well (seen on the left) and the planar waveguide (on the right) in relation to the coordinate space.

4.3. Classifications of photonic bound states in the continuum (BICs)

Introduced in 1929, BICs are localized light states within the continuum spectrum, exhibiting an ideal infinite quality factor (*Q*) due to destructive interference. They have revolutionized wave studies. Drawing from the formation process, the BICs that relevant to photonics can be classified into four unique types [21].

Single-Resonance Parametric BICs: These arise from a single resonant mode where light from its components cancels out destructively, preventing radiation [9, 21].

Symmetry-Protected BICs (SP-BICs): Prevalent in structures with a specific symmetry, SP-BICs exploit a mismatch between radiating and resonant states. Their unique configuration prohibits coupling with light waves that can escape, often manifesting at the center of the band structure (Γ-point) [9, 17, 21].

Accidental BICs (FW-BICs): Emerging from the interaction of various optical system states, these BICs appear when specific structural parameters lead to destructive interference, effectively silencing a resonant mode [9, 21].

Fabry-Perot (FP) BICs: Light becomes trapped between perfect reflectors, resonating perfectly due to complete destructive interference, maximizing light-matter interaction [9, 21].

In real-world applications, ideal BICs are rare due to limitations in size. However, "quasi-BICs" with very high *Q*-factors can be achieved, offering a practical alternative. Additionally, the "near-BIC" regime exhibits high *Q*-factors near the ideal BIC and can be excited by freely propagating light waves, making it more robust to manufacturing variations [14, 15, 16, 17].

BICs have been explored in various systems, from purely dielectric to metallic and hybrid configurations. Dielectric BICs are prominent in photonic crystal structures and metasurfaces [11, 14, 17]. Combining them with layered materials or high-index crystals can lead to complex optical behaviors. Metallic BICs involve the interaction between light and surface plasmon polaritons (SPPs). Hybrid BICs, combining photonic and plasmonic elements, offer exceptional light confinement despite challenges at visible and near-infrared wavelengths due to plasmonic losses [22, 23].

Since the first experimental observation in 2011 [15], BIC research has gained significant momentum. The potential for manipulating light within the continuum opens doors for innovative photonic devices. Enhanced *Q*-factors in nano-optical systems can lead to stronger light-matter interactions, with applications from nanocavities to advanced imaging [24]. Minimized losses due to BIC mode confinement have the potential to revolutionize on-chip communication [25]. Additionally, quasi-BICs in nonlinear mediums might enable harmonic generation, while systems with high chirality could advance circular dichroism and chiral sensing [25].

4.3.1 Bound States in the continuum (BICs): Friedrich and Wintgen (FW) model

In our study, we have extensively reviewed the 1929 proposition postulated by von Neumann and Wigner. They suggested that, under the influence of a specific oscillating bounded potential, the single-particle Schrödinger equation could produce localized solutions associated with discrete eigenvalues embedded within the continuum of positive energy states. This premise was further refined by Stillinger and Herrick, who studied various instances where

spherically symmetric local potentials could support BICs of scattering states, notably relating to potential BICs in atomic and molecular structures [5]. For a considerable duration, such phenomena were largely regarded as a mathematical curiosity, even though its core principles closely aligned with the Anderson localization approach [7,27]. BICs, understood as localized states, emerge due to the exact destructive interference of waves diffused by the constrained potential, ensuring that beyond a set boundary, no wave extends outward. This mechanism underpinning BICs was further illuminated through Friedrich and Wintgen's seminal work [6], offering a holistic perspective on realizing BICs in quantum frameworks.

BICs arise as a result destructive interference between two leaky waves. In this discussion, we explore how FW BICs come about from the interaction of different vibrations.

At its core, the FW BICs model draws inspiration from the foundational principles of the temporal coupled-mode theory for an open system. This theory centers around the coupling of 'n' modes using a time-dependent formalism specifically tailored for optical resonators. Our analysis here is guided by the work of Suh *et al*. [27], Hsu *et al*. [9], and Koshelev *et al*. [17]. The dynamic resonance amplitude equations can be represented as:

$$\frac{da}{dt} = j\Omega a$$

Here, Ω is a $n \times n$ matrix representing resonance frequencies and mode couplings, with a symbolizing the complex amplitude vector described as $a = (a_1, \quad a_{2,} \quad \cdots \; a_n)^T$.

Considering an open construct such as a resonator with two leaky modes, represented as $|\psi_s >$ (where s can be 1 or 2), these modes possess nearly, or even matching, eigenfrequencies given by $\Omega_s = \omega_s + i\gamma_{\,s}$ for both s values. When these resonances overlap spatially, radiation

interference can facilitate the emergence of a BIC, culminating in either a true BIC or its approximation, known as a *quasi*-BIC. Examining this through a two-mode approximation lens, framed by the temporal coupled-mode theory, $a = (a_1, \ a_2)^T$ conveys the complex amplitudes of states$|\psi_1>$ and $|\psi_2>$,evolving overtime as:

$$\frac{da}{dt} = Ha,$$

Here, the Hamiltonian is given by:

$$H = \begin{pmatrix} \omega_1 & \kappa \\ \kappa & \omega_2 \end{pmatrix} - i \begin{pmatrix} \gamma_1 & \sqrt{\gamma_1 \gamma_2} \\ \sqrt{\gamma_1 \gamma_2} & \gamma_2 \end{pmatrix}.$$

The parameter κ signifies the internal resonance coupling, with frequencies $\omega_{1,2}$ and varying radiation rates $\gamma_{1,2}$. Both resonances share a radiative channel, prompting interference, marked by the term $\sqrt{\gamma_1 \gamma_2}$. Such interference leads to a specific condition, as dictated by:

$$\kappa(\gamma_1 - \gamma_2) = \sqrt{\gamma_1 \gamma_2}(\omega_1 - \omega_2)$$

This condition, when met, transforms one eigenvalue into a purely real form, culminating in a BIC, while its counterpart becomes considerably more lossy. This BIC equation is a testament to Friedrich and Wintgen's contributions.

Further exploration reveals that the onset of Friedrich–Wintgen BICs is observed near the frequency crossings of the uncoupled resonances, especially when κ is approximately zero or when γ_1 is nearly equal to γ_2 . Thus, the desired conditions can be achieved by adjusting the parameters associated with the two interconnected resonances.

4.4 Overview of one-dimensional photonic crystal structure

Before discussing the potential formation of BICs in periodic optical structures using the proposed FW model, it is important to provide a concise overview of the design and modeling principles for a simple one-dimensional (1-D) photonic crystal structure, such as the one illustrated in Fig.4.3.

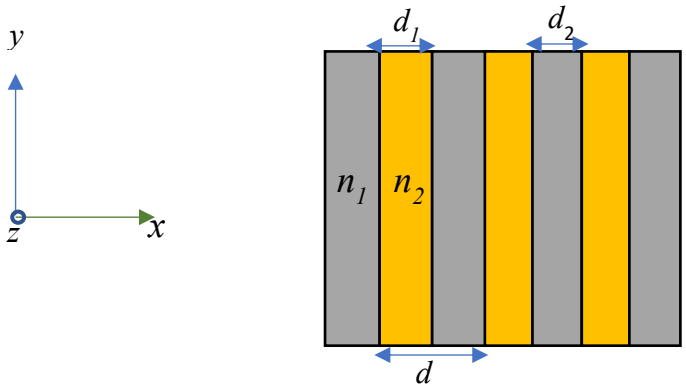

Fig. 4.3. Illustration of a one-dimensional photonic crystal slab. The slab demonstrates a period *d* in the *x*-direction and comprises alternating layers with different properties. The layers possess refractive indices n_1 and n_2, each with corresponding thicknesses d_1 and d_2.

In the field of nanophotonics, 1D photonic crystals can be realized through periodic strip structures, as shown in Fig.4.3. These strip configurations consist mainly of a high-index crystal layer, which serves as the core layer for optical waveguides. This high-index layer is combined with materials of lower refractive indices, such as air, silicon oxide, or polymer, resulting in a periodically modulated refractive index distribution. In our study, the selected refractive indices for the low and high-index crystals are $n_1 = 1.5$ and $n_2 = \sqrt{12}$ respectively. The thickness of the low-index layer is defined as $d_1 = 0.6$ and the thickness of the high-index

layer is $d_2 = 0.4$, giving $d = d_1 + d_2$, as the periodicity. In our analysis, we use normalized units due to the scale invariance of the Maxwell's equations.

Light can propagate in any direction relative to these photonic crystals, but two commonly employed cases are [29]:

(a) when light propagates across the 1D photonic crystal (along the *y*- or *z*-axis in Fig.4.3), and (b) when light propagates along the length of the 1D photonic crystal (along the *x*-axis). Here we will primarily focus on lengthwise periodic structures because they can be easily integrated with sub-micrometer silicon waveguides for example when designing and modelling silicon photonics, and offer more flexibility compared to crosswise periodic structures.

A lengthwise 1D photonic crystal, as shown in Fig.4.3, generally operates in three regimes based on the ratio between the structure's period (d) and the operating free space wavelength (λ):

(i) Diffraction regime: In this regime, the incoming beam scatters into different orders.

(ii) Bragg reflection regime: Here, the incoming beam is reflected backward.

(iii). Sub-wavelength regime: In this regime, the diffraction and reflection effects caused by the periodicity of the structure are minimized.

In Fig. 4.4, we present the plot of k-ω diagram (band diagram) of the 1-D periodic structure depicted in Fig. 4.3. The Γ point (0,0), highlighted in red, represents one of the highly symmetric points within the first Brillouin zone.

It is evident that, for a given periodic structure, the operating regime strongly depends on the free-space operating wavelength (λ) or operating frequency (ω). When ω exceeds 1.70 (above

the first photonic bandgap), the waveguide becomes lossy for Bloch mode, leading to the radiation of light out of the waveguide. This characteristic has been utilized in the design of fiber-to-chip surface couplers (grating couplers).

In the frequency range of $1.03 < \omega < 1.70$ (the first photonic bandgap), light cannot propagate through the periodic structure and is reflected, which corresponds to the Bragg reflection regime.

In this particular regime, the propagation constant, denoted as k_B, retains a constant value given by $k_B = \pi/d$. Given that $d = 1$ in our study, this directly translates to $k_B = \pi$, as depicted in Fig.4.4.

This specific bandgap property has been extensively utilized to create distributed Bragg reflectors (DBRs) on different photonic platforms. The final phase occurs below the initial photonic bandgap, where the operating frequency is lower than 1.03. As illustrated in Fig.4.4, it can be observed that the propagation constant, k_x, increases progressively as the operating frequency increases, indicating that the periodic waveguide functions similarly to a conventional

waveguide. As a result, in the sub-wavelength regime, these periodic configurations function as homogenous or uniform mediums (for instance, dielectric slab waveguide).

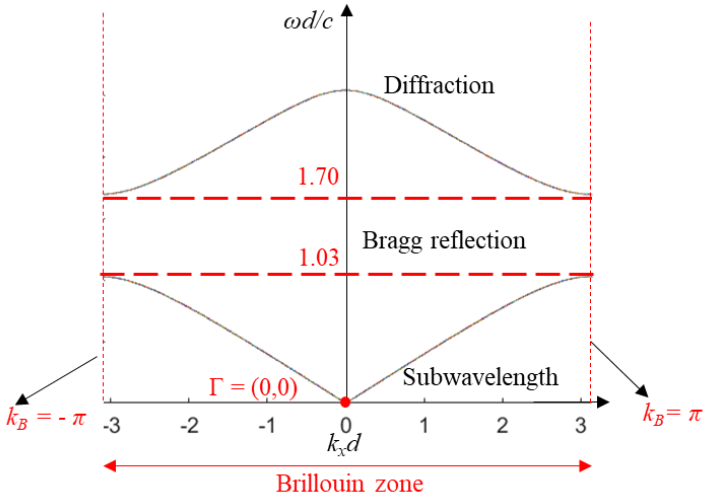

Fig.4.4. Dispersion relation plot for a one-dimensional photonic crystal slab, with the boundary of the first Brillouin zone indicated by two vertical red dashed lines at Bloch wavenumbers $k_B = \pi$ and $k_B = -\pi$.

We will now focus on using the FW model to generate potential BICs in periodic structures. To demonstrate our desired outcomes, we will modify the structure illustrated in Fig.4.3 and transform it into a periodic potential with a negligible amplitude. This concept aligns with the notion of an empty lattice commonly referenced in solid-state physics. Essentially, the structure maintains a regular, repetitive pattern, but the variations within this pattern are so minuscule that they are nearly non-existent. Moreover, the layers comprising the structure in Fig.4.3 possess identical dielectric constants, indicating a uniform medium in all directions, representing a homogeneous medium where $n_1 = n_2$. In this medium, the speed of light is reduced by the index of refraction, and the modes align with the light line as described by $\omega(k) = ck/\sqrt{\varepsilon}$. A classic example of such a structure is a homogeneous, non-dispersive dielectric slab waveguide.

As a result, the band diagram plot reveals that the second bandgap remains closed, and the eigenstates at the Γ-point display degeneracy, characterized by opposing leaky waves, as

shown in Fig.4.5(a). Consequently, the bands at the Γ-point (which represent the center of the Brillouin zone) exhibit the same energy value.

On the other hand, transforming the slab waveguide into a grating waveguide while light propagates through the 1D photonic crystal structure along the *x*-axis with a period of *d*, as illustrated in Fig.4.5(b), introduces a non-zero amplitude to the periodic potential. Consequently, this disrupts the degeneracy and gives rise to a noticeable bandgap. If the periodic potential maintains symmetry with respect to the transformation $x \rightarrow -x$, new states or bands emerge at the edges of the second bandgap. These states or bands include a bound state in the continuum (BIC) formed through the anti-symmetric combination of the leaky modes, as well as a state with superradiance formed through the symmetric blend of the leaky modes, as depicted in Fig.4.5(b).

As a result, the grating waveguide exhibits both radiative (leaky) modes and guided (non-leaky) modes. If the grating waveguide is precisely designed, these modes can interfere in such a manner that the outgoing radiation from one mode precisely cancels out that of another mode, resulting in a non-radiating mode or BIC.

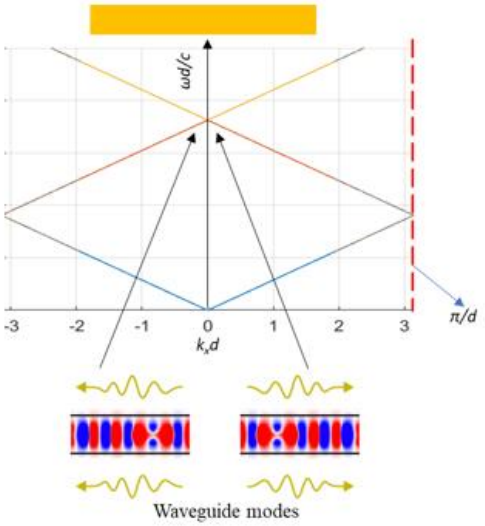

(a) homogenous slab waveguide

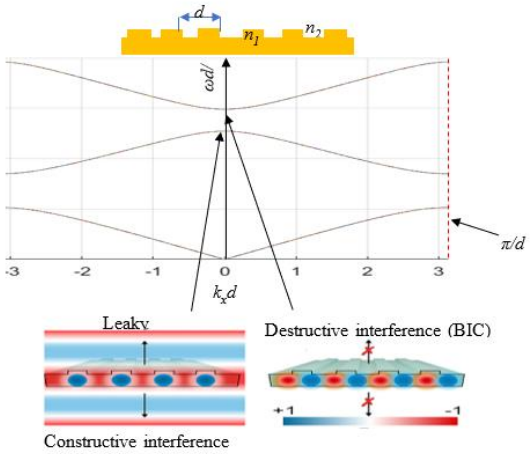

(b) Grating waveguide with period *d*

Fig. 4.5: (a) Illustrates the band structure and mode profiles for a homogeneous slab waveguide, highlighting guided modes propagating to both the left and right. (b) Depicts the band structure and mode profiles of a grating waveguide with a period of '*d*'. In this configuration, the periodicity facilitates mode interactions, leading to the formation of two distinct states. These states result from constructive (leaky mode) and destructive (Bound State in the Continuum, BIC) interference patterns.

4.5 Bound states in the continuum in periodic gratings structures

Section 4.3 established that light confined within individual cavities or waveguides does not interact with the continuous spectrum modes of free space. This implies that optical system eigenstates can only be localized when their energies fall below the light line in the surrounding medium [30]. Conversely, modes within the continuous spectrum, known as leaky modes, exhibit low-quality factors due to radiation losses [31].

However, Bound States in the Continuum (BICs) can be realized using periodic structures such as dielectric gratings or photonic crystals [32, 33]. This section delves deeper into the mechanisms underlying BIC formation in these structures. We will explore this concept using the example of a dielectric grating or a one-dimensional photonic crystal structure with a period *d*, as depicted in Figure 4.6a.

Within a photonic crystal, any eigenmode can be characterized by its wavevector *k.* The electric field resonance can be expressed as follows [34]:

$$E(x, y, z) = U_{N,k_x}(x, z) \cdot e^{ik_x x + ik_y y} \qquad (4.9).$$

In this context, *z* represents the direction perpendicular to the slab, while $U_{N,k_x}(x, z)$ is a function periodic in *x*, satisfying $U_{N,k_x}(x + d, z) = U_{N,k_x}(x, z)$, k_y is a wavenumber corresponding to the direction of the translation symmetry, k_x is the Bloch wavenumber, and *N* is the index of the band.

If the structure under consideration (Fig. 4.6a) is periodic, with dielectric variation in the *x*-direction, then equation (4.9) becomes a Bloch function, and limiting our analysis to the case of TE polarized modes $\left[E = \left(0, E_{y,}0\right)\right]$ [33], equation (4.9) can be expressed as:

$$E_y(x, z) = U_{k_x}(x, z) \cdot e^{ik_x x + ik_y y} \qquad (4.10),$$

and if k_y= 0, for a TE polarized mode, then equation (4.10) can be written as:

$$E_y(x, z) = U_{k_x}(x, z) \cdot e^{ik_x x} \qquad (4.11).$$

In a periodic structure such as a photonic crystal slab, electromagnetic fields exhibit a consistent and repetitive pattern because of the slab's periodic structure. However, when these

fields leave the slab, they can either freely propagate as plane waves that do not diminish in intensity, or in specific circumstances, they appear as evanescent waves that rapidly decrease in intensity as they move away from the surface of the slab.

Therefore, BICs in these structures appear only if either $k_x = 0$, or $k_y = 0$.

Hence, the periodic Bloch amplitude, $U_{k_x}(x, z)$, which is a periodic function with respect to the *x* variable can be decomposed into a Fourier series as:

$$U_{N,k_x}(x, z) = \sum_m C_{m,k_x}(z) e^{\frac{i2\pi mx}{d}} \quad (4.12).$$

In this analysis, m is an integer that denotes a diffraction channel. The coefficients $C_{m,k_x}(z)$ are functions dependent on the vertical variable *z* and exhibit asymptotic behavior akin to exponential functions. These coefficients symbolize far-field or near-field behaviors for open or closed channels, respectively. Closed channels, or near fields, correspond to those eigenstates situated below the light line [32], as depicted in Fig.4.6c. In this region, characterized by the absence of open channels, only waveguide modes prevail, preventing wave radiation into the far field, as shown in the figure.

When a diffraction channel m is open, $C_{m,k_x}(z)$ simplifies to a plane wave with complex amplitudes along the *z*-direction. To realize a Bound State in the Continuum (BIC), it is essential to nullify the complex amplitudes of these open diffraction channels $C_{m,k_x}(z)$. Our goal is to minimize radiation

losses to enhance the *Q*-factor, and hence BIC appear when leakage into all open diffraction channels are forbidden. Therefore, we focus on the sub-diffractive regime, where there is only one open channel — predominantly normal to the surface plane. By this approach, all other

open channels are canceled out, focusing exclusively on the open channel corresponding to m =0, where the amplitude of the outgoing leaky wave is defined by the zeroth Fourier coefficient $C_{0,k_x}(z)$.

However, it is important to note that $C_{0,k_x}(z)$ essentially the average value of the periodic function $U_{0,k_x}(x,z)$.

We can now determine the expansion coefficient C_0 (z) for the diffraction channel m =0, as well as the Bloch wavevector, since it has previously been stated that the region on the dispersion band diagram, which yields a (BIC) corresponds to the open channel with m = 0. Specifically, a resonance evolves into a BIC when the outgoing power becomes zero. This condition is met when $C_{0,k_x}(z)$ = 0. Therefore, in our study, the primary objective is to nullify $C_0(z)$. To achieve this, we calculate the zeroth Fourier coefficient from the expansion presented in equation (4.12). Consequently, for m = 0, equation (4.12) is reformulated as follows:

$$U_{0,k_B} = \sum_0 C_{0,k_x}(z)\ e^{ik_B x} \qquad (4.13)$$

Hence, the complex coefficients for the zeroth-order (m = 0) in the Fourier series are given by:

$$C_{0,k_x}(z) = \int_{\frac{-d}{2}}^{\frac{d}{2}} U_{0,k_B}(x,z) \cdot e^{-ik_B x} dx \qquad (4.14)$$

Equation (3.29) depicts the average value of the periodic function $U_{k_B}(x,z)$ for a state located at the center of the Brillouin zone, where $k_x = k_B = 0$. Therefore, equation (4.14) can also be expressed as follows:

$$C_{0,k_x}(z) = \int_{\frac{-d}{2}}^{\frac{d}{2}} U_{0,k_B}(x,z)dx = \langle U_{0,k_x}(x,z)\rangle_x \qquad (4.15)$$

We recognize that for a periodic structure with a unit cell symmetric along the *x*-direction—characterized by time-reversal and 180° rotational symmetries under the operation $C_2^z T$ —the coefficient $C_{0,k_x}(z)$ becomes purely real [35]. Here, C_2^z denotes a 180° rotation around the *z*-axis, and *T* represents the time-reversal operator. Consequently, at the *Γ*-point (the center of the Brillouin zone), all eigenstate solutions, denoted as $\langle U_{0,k_x}(x,z)\rangle_x$, can be classified into symmetric (even) and antisymmetric (odd) functions with respect to *x*. This classification leads to the realization that for antisymmetric (sine) solutions, the mean (average) value of $\langle U_{0,k_x}(x,z)\rangle_x$ = 0, resulting in $C_{0,k_x}(z)$ = 0 according to equation (4.15).

Therefore, at the *Γ*-point, the appearance of a BIC necessitates that the *x*-averaged field be zero. This prerequisite ensures that all antisymmetric states decouple at the *Γ*-point, one of the most symmetric points in the Brillouin zone, where the Bloch wavenumber k_B = 0. Fundamentally, a resonance evolves into a BIC when the outgoing power is eliminated, achievable only if $C_{0,k_x}(z)$ = 0, causing the *Q*-factor to diverge and, theoretically, becomes infinite at the *Γ*-point. Consequently, all such states—resonances above the light line and wavelengths below the diffraction limit—are classified as BICs. These are identified as symmetry-protected BICs, highlighting that the radiation cancellation is ensured by the structure's symmetry. Since these BICs emerge at the *Γ*-point, they are occasionally referred to as 'at-*Γ* BICs'.

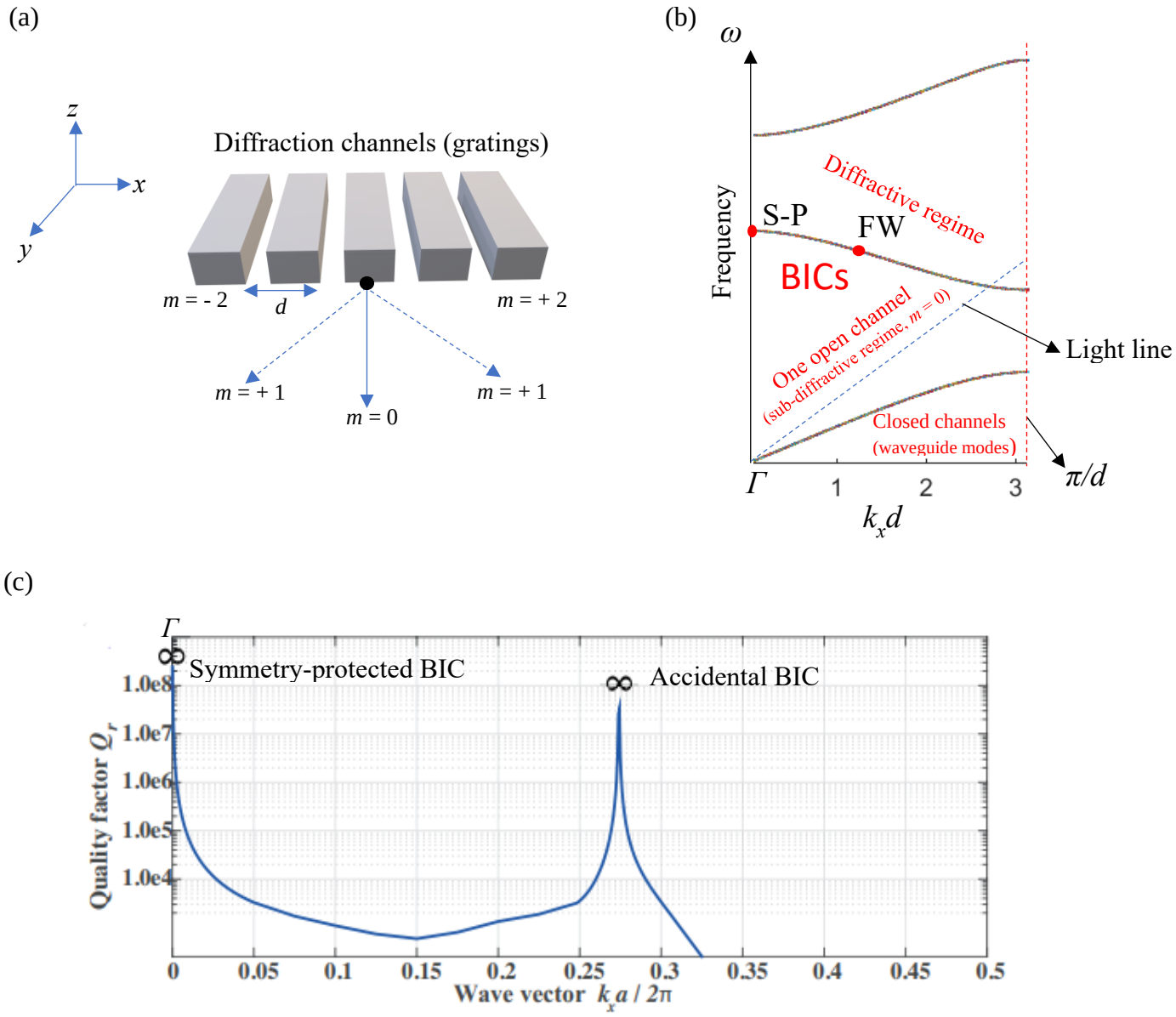

Figure. 4.6 Bound States in the Continuum within a dielectric grating: (a) provides a schematic of the grating structure, characterized by one-dimensional periodicity along the x-direction; (b) illustrates the band diagram for a structure similar to that depicted in (a); (c) presents the *Q*-factor for a structure resembling the one in (a), adapted from [32].

Regarding the symmetric (even) solutions, the average value of the eigenstate, $\langle U_{0,k_x}(x,z)\rangle_x$, can be nullified at a specific point in the Brillouin zone. This phenomenon is not solely due to symmetry considerations but also through the fine-tuning of the system's parameters, such as

period, radius, and permittivity, leading to the emergence of a BIC. This type of BIC is commonly referred to as an *accidental*, *parametric*, or *tunable* BIC (Friedrich-Wintgen BIC), necessitating precise structural adjustments to achieve $\langle U_{0,k_x}(x,z)\rangle_x = 0$. These BICs are also known as 'off-Γ BICs,' distinguishing them from those that occur at the Γ-point

Fig.4.6 presents various aspects of the structure under examination: (a) illustrates its schematic representation, (b) depicts its band structure, and (c) demonstrates the *Q*-factor, highlighting both symmetry-protected and accidental Bound States in the Continuum (BICs).

4.5.1 Engineering bound states in the continuum (BIC) for enhanced light-matter interaction in hybrid metasurfaces

This section explores the emergence of Bound States in the Continuum (BIC) within the proposed hybrid metasurface. Strong mode confinement in the elements leads to multiple quasi-BIC points due to destructive interference and the collapse of the Fano lineshape width.

The proposed hybrid metasurface under consideration consists of a periodic array of unit cells, each containing two nanopillars (see Fig.4.7a, for detailed unit cell description). Each nanopillar is composed of four nanodisks: two plasmonic, fabricated from silver, and two made from high-refractive-index silicon. The nanodisks share a uniform height (H = 120 nm). One radius (R_1) is fixed at 50 nm, while the other radius (R_2) varies between 30 nm and 70 nm. The pairs are arranged periodically with a lattice constant (*P*) of 550 nm ($P_x = P_y = P$) in both *x* and *y* directions. The entire array is illuminated with *x*-polarized light at normal incidence. Both the substrate and the superstrate surrounding the array are composed of silica.

(a) (b)

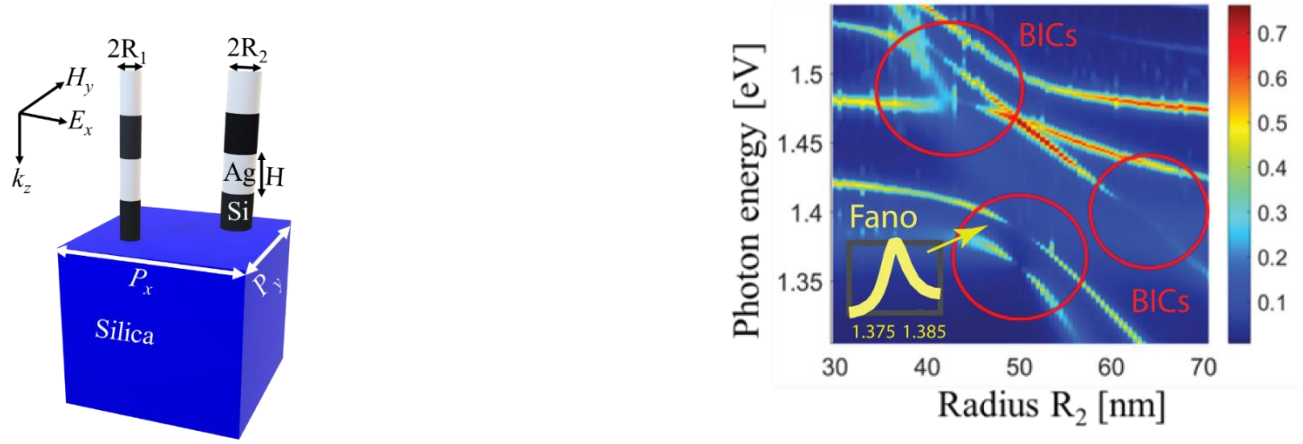

Figure 4.7. (a) Schematic of the proposed hybrid metasurface under consideration, where the unit cell consists of two elements (nanopillars). Each element has four nanodisks: two plasmonic made of silver and two made of high-refractive-index material, silicon. The nanodisks are of height H = 120 nm and radii R_1 = 50 nm (fixed) and R_2, varied from 30 to 70 nm. The pairs are arranged in periodic array with periods $P_x = P_y = P$ = 550 nm. The array is illuminated with the *x*-polarized light at the normal angle. The substrate and superstrate materials are silica. Considering the center of the unit cell has coordinates (0, 0), the first element has coordinates ($-P_x/4$, $-P_y/4$), and the second element has coordinates ($P_x/4$, $P_y/4$). (**b**) Numerical results and mode contours are for modeling the proposed nanostructure: The simulated absorption spectra versus radius of nanoantenna showing sextuple Fano resonances and triple Rabi splitting. It shows quintuple BICs in the nanostructure. Bound states in the continuum are shown in red circles due to the collapse of the widths of Fano resonances observed in the nanostructure. Inset: Fano profile of the mode at ~1.38 eV for R_2 = 48 nm.

Considering the center of the unit cell at coordinates (0, 0), the first element has coordinates ($-P_x/4$, $-P_y/4$), and the second element has coordinates ($P_x/4$, $P_y/4$). The BIC-based hybrid metasurface exhibits high sensitivity and selectivity because a small parameter mismatch in the binary array can create a BIC within the bandgap of the coupled modes.

The identification of spectral features near BIC points is achieved by analyzing the resonance linewidth. At the BIC point, the linewidth becomes very narrow due to destructive interference between discrete and continuum modes. Additionally, analyzing the electromagnetic field intensity and polarization patterns near the resonance can provide valuable information for identifying BICs.

In binary nanoparticle arrays, BICs are achieved by tailoring the geometric parameters of individual elements to create destructive interference between modes, leading to unique optical properties with potential applications in sensing. A small parameter mismatch in the binary array can create a BIC within the bandgap of the coupled modes, enhancing light-matter interaction within the metasurface region for highly sensitive and selective sensing. The presence of the BIC also leads to a sharp resonant peak in the transmission or reflection spectrum, facilitating the detection of changes in the surrounding environment, such as biomolecule adsorption or gas presence. Furthermore, BIC-based plasmonic sensors exhibit high robustness against fabrication imperfections and environmental changes due to the highly localized nature of the BIC, enabling highly reproducible sensing with minimal drift over time [36].

Figure 1b shows discontinuities in the nanostructure modes (around the anticrossings marked by red circles in the absorption colormap) that occur due to suppressed radiative losses from destructive interference and BIC formation. These discontinuities indicate singularities in the Fano parameter, leading to the collapse of the Fano lineshapes and trapping of electromagnetic modes within the nanostructure. This phenomenon results in a rapid increase in the *Q*-factor until it reaches a maximum value due to finite size effects [36].

4.6 References

[1] F. Riboli et al., "Engineering of light confinement in strongly scattering disordered media," Nature Materials, 13(7), 720-725 (2014).

[2] Z. Li et al., "Controlling propagation and coupling of waveguide modes using phase-gradient metasurfaces," Nature Nanotechnology, 12(7), 675-683 (2017).

[3] B. E. A. Saleh & M. C. Teich, “Fundamentals of Photonics (2nd ed., p.1072),” Wiley-Interscience (2007).

[4] A. Yariv & P. Yeh, Photonics: Optical Electronics in Modern Communications (6th ed.), Oxford University Press (2007).

[5] F. H. Stillinger & D. R. Herrick, "Bound states in the continuum," Physical Review A, 11(2), 446 (1975).

[6] H. Friedrich & D. Wintgen, "Physical realization of bound States in the continuum," Physical Review A, 31(6),3964 (1985).

[7] F. Capasso et al., "Observation of an electronic bound state above a potential well," Nature, 358, 565–567 (1992).

[8] M. Robnik, "A simple separable Hamiltonian having bound states in the continuum," J. Phys. A: Math. Gen., 19, 3845 (1986).

[9] C. W. Hsu et al., "Bound states in the continuum," Nature Reviews Materials, 1, 16048 (2016).

[10] A. F. Sadreev et al., "Bound states in the continuum in open quantum billiards with a variable shape," Phys. Rev. B, 73, 235342 (2006).

[11] J. von Neumann & E. Wigner, "Über merkwürdige diskrete Eigenwerte: Über das Verhalten von Eigenwerten bei adiabatischen Prozessen," Physikalische Zeitschrift, 30, 465-467 (1929).

[12] I. Deriy et al., "Bound States in the Continuum in Compact Acoustic Resonators," Physical Review Letters, 128(8), 084301 (2022).

[13] D. C. Marinica et al., "Bound States in the Continuum in Photonics," Physical Review Letters, 100(18), 183902 (2008).

[14] C. Hsu et al., "Observation of trapped light within the radiation continuum," Nature, 499, 188–191 (2013).

[15] Y. Plotnik et al., "Experimental observation of optical bound states in the continuum," Physical Review Letters, 107(18), 183901 (2011).

[16] A. Kodigala et al., "Lasing action from photonic bound states in continuum," Nature, 541(7636), 196-199 (2017).

[17] K. L. Koshelev et al., "Bound states in the continuum in photonic structures," Physics - Uspekhi, 66(5), 494-517 (2023).

[18] Y. Peng & S. Liao, "Bound states in continuum and zero-index metamaterials: A Review," arXiv preprint arXiv:2007.01361.

[19] K. Okamoto, “Fundamentals of Optical Waveguides (2nd ed.),” CRC Press (2006).

20. [20] S. V. Gaponenko, “Introduction to Nanophotonics,” Cambridge University Press (2010).

[21] P. Hu et al., "Global phase diagram of bound states in the continuum," Optica, 9(12), 1353 (2022).

[22] H. Zhong et al., "Photonic Bound States in the Continuum in Nanostructures," Materials, 16, 7112 (2023).

[23] Y. Liang et al., "Bound States in the Continuum in Anisotropic Plasmonic Metasurfaces," Nano Letters, 20(9), 6351-6356 (2020).

[24] N. J. J. van Hoof et al., "Unveiling the Symmetry Protection of Bound States in the Continuum with Terahertz Near-Field Imaging," ACS Photonics, 8(10), 3010-3016 (2021).

[25] I. S. Chung, S. Tandukar, & A. Taghizadeh, "Silicon-on-chip laser based on bound states in the continuum," The 23rd OptoElectronics and Communications Conference (OECC 2018) Technical Digest, Jeju, Korea.

[26] Z. Liu et al., "High-Q Quasi-bound States in the Continuum for Nonlinear Metasurfaces," Physical Review Letters, 123(25), 253901 (2019).

[27] Y. X. Xiao et al., "A band of bound states in the continuum induced by disorder," Scientific Reports, 8, 5160 (2018).

[28] W. Suh, Z. Wang, & S. Fan, "Temporal Coupled-Mode Theory and the Presence of Non-Orthogonal Modes in Lossless Multimode Cavities," IEEE Journal of Quantum Electronics, 40(10), 1511 (2004).

[29] A. Vakhrushev (Ed.), “Theoretical Foundations and Application of Photonic Crystals,” InTech, https://doi.org/10.5772/intechopen.69145 (2018).

[30] Z. Yu et al., "Photonic integrated circuits with bound states in the continuum," Optica, 6(11), 1342–1348 (2019).

[31] J. Hu & C. R. Menyuk, "Understanding leaky modes: Slab waveguide revisited," Advances in Optics and Photonics, 1(1), 58–106 (2009).

[32] Z. F. Sadrieva & A. A. Bogdanov, "Bound state in the continuum in the one-dimensional photonic crystal slab," Journal of Physics: Conference Series, 741, 012122 (2016).

[33] E. E. Maslova et al., "Bound states in the continuum in periodic structures with structural disorder," Nanophotonics, 10(17), 4313-4321 (2021).

[34] K. Sakoda, “Optical Properties of Photonic Crystals (2nd ed.),” Springer (2004).

[35] B. Zhen et al., "Topological nature of optical bound states in the continuum," Physical Review Letters, 113(25), 257401 (2014).

[36] L. Lin et al., "Photoswitchable Rabi splitting in hybrid plasmon-waveguide modes," Nano Letters, 16, 7655–7663 (2016).

Chapter 5

Contents

5.0 Rabi Splitting: a hallmark of strong light-matter interaction

The interaction between light and matter is a cornerstone of quantum optics, driving a wide range of phenomena with profound implications for quantum technologies. Among these, Rabi

splitting stands out as a signature of strong coupling between a quantum emitter and a photonic cavity mode [1].

Rabi splitting arises from the quantum mechanical description of light-matter interaction, particularly the Rabi model. This model depicts the oscillation of an atomic state under an oscillating electric field, leading to a periodic energy exchange between the atom and the field, known as Rabi oscillations [2,3]. When a quantum emitter (atom or quantum dot) resides within a resonant cavity, the coupling strength between them can reach a regime where the energy exchange surpasses the individual decay rates. In this strong coupling regime, the system's eigenstates hybridize into light-matter states, manifesting as a doublet in the system's emission or absorption spectrum, corresponding to the energy difference between the hybridized states [4].

A more comprehensive theoretical description of Rabi splitting comes from quantum electrodynamics (QED), specifically the Jaynes-Cummings model. It extends the Rabi model by including the quantization of the electromagnetic field within the cavity [5,6]. This quantization is crucial for understanding the discrete nature of the interaction and the conditions for Rabi splitting. The Jaynes-Cummings model predicts that the visibility of Rabi splitting depends on the coupling strength, the damping rates of the emitter and cavity, and the detuning between the emitter's transition frequency and the cavity resonance [7].

Experimental evidence for Rabi splitting exists in various systems, including atoms in optical cavities, semiconductor quantum dots in microcavities, and molecules coupled to plasmonic structures [8, 9, 10]. These experiments not only validate theoretical predictions but also showcase the diverse platforms where Rabi splitting can be observed and harnessed. The

ability to engineer and control these hybridized states opens doors to novel devices based on quantum light-matter interactions, such as quantum dots for quantum computing, single-photon sources for quantum cryptography, and ultra-sensitive sensors.

Beyond the quantum realm, strong coupling can also occur in classical photonic systems. An example is the observed avoided crossing of resonances between surface plasmon polaritons and photonic modes in hybrid plasmonic-photonic structures [11]. Additionally, strong coupling can arise between two Fano resonances that share the same continuum state. In this scenario, manipulating the discrete state of one Fano resonance can induce significant interaction between them [12].

This chapter introduces the concept of Rabi splitting through quantum mechanical modeling of a two-level quantum system interacting with a photonic cavity. We then explore classical analogs of Rabi splitting, demonstrating the potential for strong coupling between Fano resonances in a photonic nanostructure system, distinct from the quantum mechanical approach.

Following this, we present nanostructure designs featuring layered hybrid plasmonic-dielectric nanoantennas. By adjusting the dimensions of one nanoantenna, this design facilitates strong mode coupling and the formation of multiple *quasi*-BICs with high-quality factors. These dimensional variations lead to interactions between multiple Fano resonances, and under strong coupling conditions, this results in the hybridization of the interacting Fano resonances, observable as multiple anti-crossings (Rabi splitting) in the energy dispersion plots.

In conclusion, Rabi splitting epitomizes a fundamental phenomenon in quantum optics, capturing the essence of strong coupling interactions between light and matter. Its exploration

not only deepens our understanding of quantum mechanics but also paves the way for groundbreaking quantum technologies.

5.1 Theoretical Foundations of Rabi Splitting

Rabi splitting, a hallmark of strong coupling between a quantum system and a quantized electromagnetic field, is frequently observed in atom-cavity, exciton-photon, and spin-boson configurations. It manifests as the splitting of the energy levels in the quantum system due to its interaction with a resonant driving field (Fig. 5.1). This phenomenon occurs when the emitter's atomic transition frequency (ω_a) aligns with the resonant frequency of the cavity mode (ω_c). This alignment leads to the hybridization of the two states, resulting in their splitting into two new energy levels. These hybridized states are known as the lower polariton ($|L_1\rangle$) and upper polariton ($|L_2\rangle$), separated by the Rabi splitting energy ($\hbar\Omega_R$), where $\hbar$ is the reduced Planck constant and Ω_R represents the Rabi frequency. The splitting of the energy levels is reflected in the peaks of the scattering parameters (reflection, transmission, absorption) spectra, highlighting the significant impact of Rabi splitting on the system's optical properties.

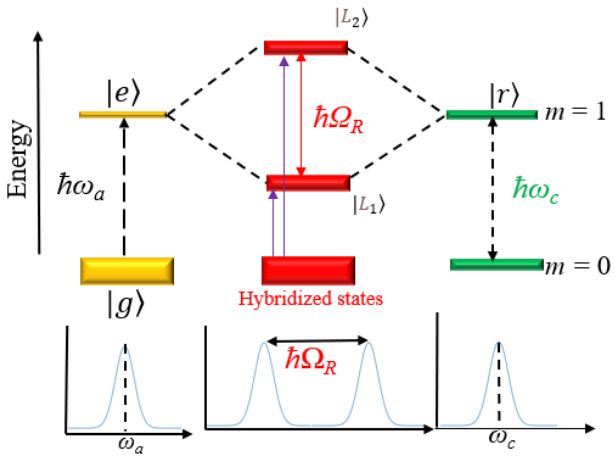

Fig. 5.1: Schematic Illustration of Rabi Splitting (Strong Coupling) in a Quantum System. The figure depicts the interaction between a two-level quantum emitter undergoing a transition from the ground state $|g\rangle$ (n=0) to the excited state $|e\rangle$ (n=1), and an optical cavity mode transitioning from m=0 to m =1. Here, $|r\rangle$ represents the resonance of the cavity, illustrating the precise moment of strong coupling between the quantum emitter and the cavity mode.

At the heart of Rabi splitting is the interaction between a two-level atom (or, equivalently, a molecule or quantum emitter) and the discrete modes of an electromagnetic field within a photonic cavity. When the excited state ($|e\rangle$) of an atom strongly couples with a resonance state ($|r\rangle$) of a photonic cavity, the two states hybridize. This leads to the formation of two new states: the upper ($|S_2\rangle$) and lower (($|S_1\rangle$)) polariton states, as illustrated in Fig. 5.2(a). This energy splitting is reflected by the anticrossing feature in the energy dispersion plot, as shown in Fig. 5.2(c). The presence of an atom within an optical cavity is represented by a red dot in Fig. 5.2(b) of the illustration. In the circle located at the lower right, we illustrate the atom's energy levels — the ground ($|g\rangle$) state and the excited ($|e\rangle$) state — interacting with the field mode inside the cavity. The emission or absorption of photons by the atom, corresponding to transitions between these two states, contributes to the field mode within the cavity.

This interaction, indicative of strong coupling, necessitates a quantum mechanical framework for accurately modeling both the atom and the cavity. The Jaynes-Cummings model, a fundamental theory in quantum optics, effectively describes this interaction when an atom is coupled with a single-mode electromagnetic field. The Hamiltonian for this interaction is outlined below [13]:

$$H = H_0 + H_1 = \frac{1}{2}\hbar\omega_a\sigma_z + \hbar\omega_c\alpha^\dagger\alpha + \hbar g(\sigma^+\alpha + \sigma^-\alpha^\dagger) \qquad (5.1)$$

Where, H_0 represents the free Hamiltonian of the atom and the electromagnetic field, featuring the first two terms, $H_1 = \hbar g(\sigma^+\alpha + \sigma^-\alpha^\dagger)$ denotes the interaction Hamiltonian between the atom and the field, $\hbar$ is the reduced Planck's constant, ω_a is the atomic transition frequency, ω_c is the cavity mode frequency, σ_z is the Pauli operator reflecting the two-level atom's energy states, $\alpha^\dagger$ and α are the creation and annihilation operators for the cavity photons, σ^+ and σ^- are the raising and lowering operators for the atom's energy states, g is the coupling strength between the atom and the cavity mode.

(a)

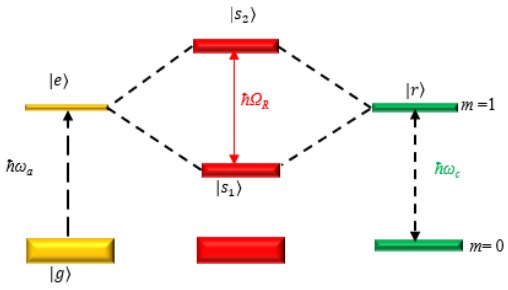

(b)

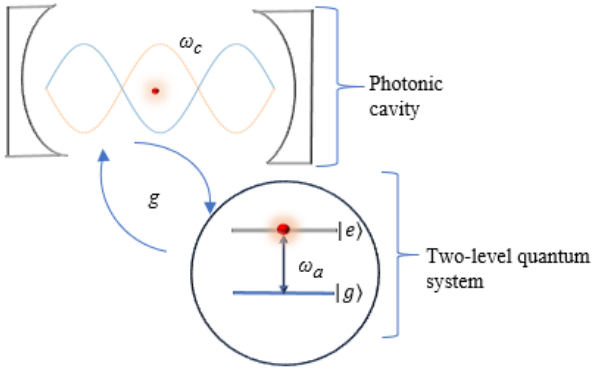

(c)

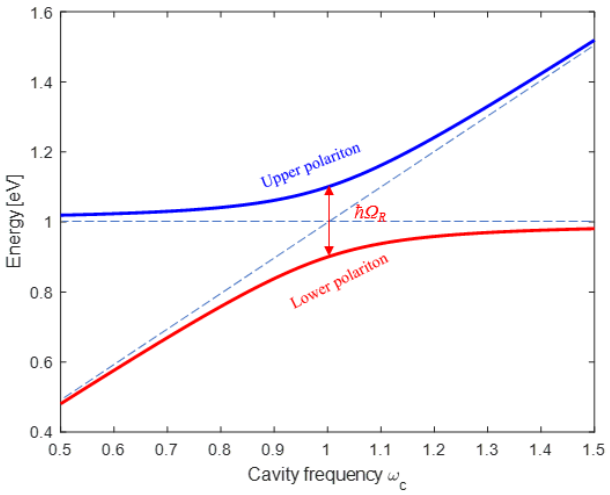

Figure. 5.2: Schematic Representation of Strong Coupling and Anti-Crossing in an Atom-Optical Field Interaction System. (a)Visualization of energy level splitting in a single atom interacting with an optical field, showcasing the atomic transition frequency ω_a and the resonance frequency of the optical field ω_c. This panel illustrates the transition of optical (photonic) cavity modes from m = 0 to m = 1. (b) Depiction based on the Jaynes-Cummings model of the interaction between an atom and a cavity. An atom within an optical field is represented by a red dot situated in the photonic cavity. The energy levels of the atom, forming a two-level quantum system that couples with the field mode inside the photonic cavity, are indicated by black circle. The coupling strength between the atom and the cavity is denoted by g. (c) Demonstration of the anti-crossing phenomenon, leading to Rabi splitting at the convergence point of ω_a and ω_c, highlighting the essential features of strong coupling between the atom and the optical field.

The Hamiltonian, H, encapsulates the quantum mechanical interaction responsible for Rabi splitting, underscoring the crucial roles of the coupling strength, g , and the resonance between the atom's transition frequency and the cavity mode frequency.

In the regime of strong coupling between the atom (or emitter) and the optical field mode, the coupling strength, g , can be characterized by the emitter's dipole moment, μ, and the vacuum electromagnetic field strength, E_{vac}, as follows:

$g = \frac{1}{\hbar}|\mu \cdot E_{vac}|$ [14], with g expressed in units of frequency. For *N* number of dipoles, g can be expressed as $g = \sqrt{N}\mu E_{vac}$.

For the system to achieve strong coupling, g must surpass all decay rates, symbolized by the condition $g >> \kappa, \gamma$, where κ, and γ denote the cavity's loss rate and the atom's (or emitter's) dissipation rate, respectively.

This state of strong coupling necessitates that the interaction strength not only dominates over the intrinsic decay mechanisms of the system but also ensures the coherent exchange of energy between the atom and the cavity mode, a prerequisite for observing Rabi splitting.

The vacuum electric field, E_{vac}, is inversely proportional to the square root of the effective cavity volume, V_{eff}, represented as $E_{vac} \propto 1/\sqrt{V_{eff}}$. For a single electromagnetic mode, the magnitude of E_{vac}can be determined by equating its energy with the zero-point energy of the mode:

$$E_{vac}^2 V_{eff} = \frac{1}{2}\hbar\omega_c.$$

Here, it is assumed that the emitter is located at the maximum of the field associated with this mode. This assumption leads to the expression for $g = \mu/\hbar\sqrt{\frac{\hbar\omega_0}{2V_{eff}}}$, where ω_0 is the resonant frequency, with $\omega_a = \omega_c$.

In Fig. 5.3, we utilize a simplified model resembling the one shown in Fig.5.2. This model consists of a single two-level system, such as an atom, and a single-mode electromagnetic field, like a photon. By solving the Jaynes-Cummings Hamiltonian, which characterizes the interaction between light and matter, we are able to calculate the eigenvalues of the

Hamiltonian for various coupling strengths, denoted by g, and plot the resulting data. The obtained results exhibit the distinct "avoided crossing" phenomenon, which serves as an indicator of Rabi splitting. We assume that the atom and cavity are not in resonance and therefore manipulate the detuning, which represents the difference between the frequencies of the atom and the cavity. Through this manipulation, we are able to observe Rabi splitting, with the lower and upper polaritons each displaying anticrossings, as depicted in Fig. 5.3 (a) with g = 0.1. The energy of Rabi splitting, which is given by $\hbar\Omega_R$, is evident in the plots.

The plots effectively illustrate the occurrence of Rabi splitting as an "avoided crossing" in the energy spectrum. As the coupling strength, g, increases, the splitting becomes more prominent. To demonstrate this, we vary the frequency of the cavity while keeping the atom's frequency fixed. The difference between these two frequencies creates a detuning, which in turn leads to Rabi splitting.

This splitting manifest as two distinct curves, representing the lower and upper polaritons, which notably avoid crossing each other. This avoidance signifies the presence of Rabi splitting. The magnitude of the splitting is directly influenced by the coupling strength, g, as illustrated in Fig. 5.3(b). By employing values of g such as 0.01, 0.1, 0.2, and 0.5, we can clearly demonstrate the varying degrees of Rabi splitting strength.

(a)

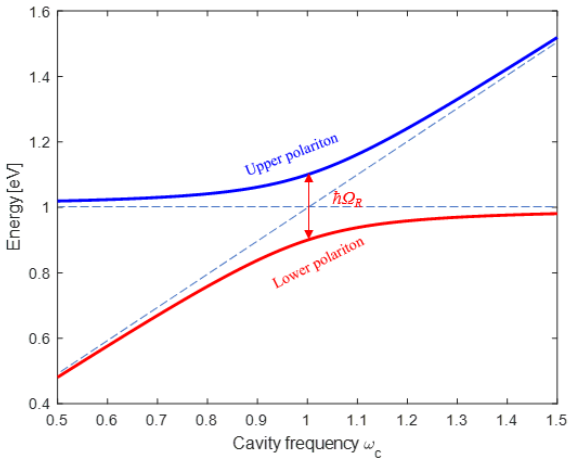

(b)

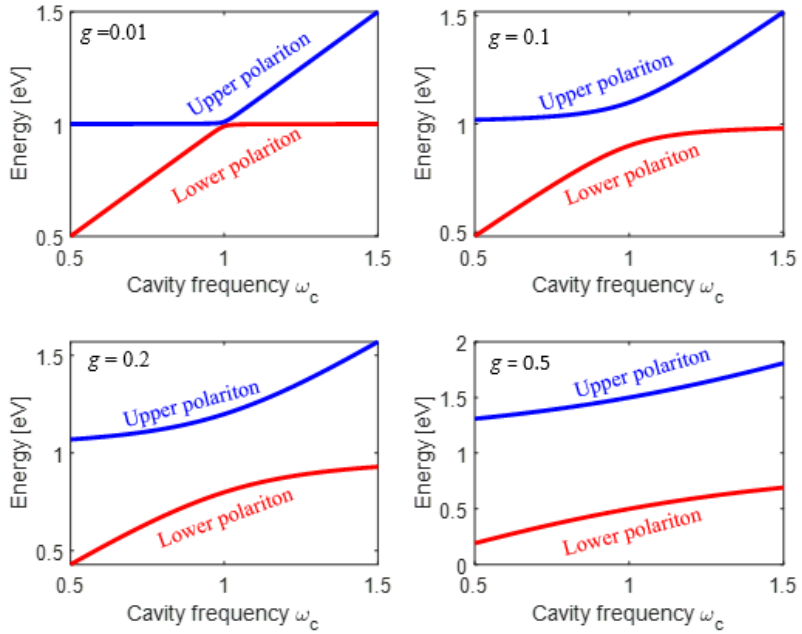

Figure.5.3 Rabi splitting (eigenvalues of the Hamiltonian) plots corresponding to (a) a two-level atom interacting with a single mode of the electromagnetic field. The states are |*g*, *n*=0> and |*e*, n=1>, where |g> and |e> are the

ground and excited states of the atom. (b) same as Fig.(a), but different values of coupling strength, g = 0.01,0.1,0.2, and 0.5.

It is worth noting that this is a simple model and does not account for many factors such as decay, or multi-level systems.

5.2 Strong Coupling via Fano Resonances

While our previous analysis of Rabi splitting focused on the quantum mechanical interaction between a two-level atomic system and a photonic cavity, a classical analog of strong coupling can also be observed in interacting photonic nanostructures. This phenomenon arises from the interplay of two Fano resonances.

Fano resonances occur due to interference between a narrow, discrete resonance and a broader spectral continuum. This interaction manifests as characteristic asymmetric line shapes in the scattering parameter spectra. When two or more Fano resonances experience strong coupling, the system can exhibit Rabi splitting. This happens when the energy exchange rate between the resonances, or between the resonances and an external field, becomes faster than the individual resonance decay rates.

In a scenario where two Fano resonances share the same continuum state (Fig. 5.4), a strong interaction can be observed by continuously varying the discrete state of one resonance (R_2, red-dashed circle) while keeping the other (R_1) constant [12]. This manipulation can lead to the hybridization of the system's energy levels, forming new eigenstates. This hybridization manifests as the splitting of the original resonance peak into two distinct peaks, signifying the emergence of new eigenstates (Rabi splitting).

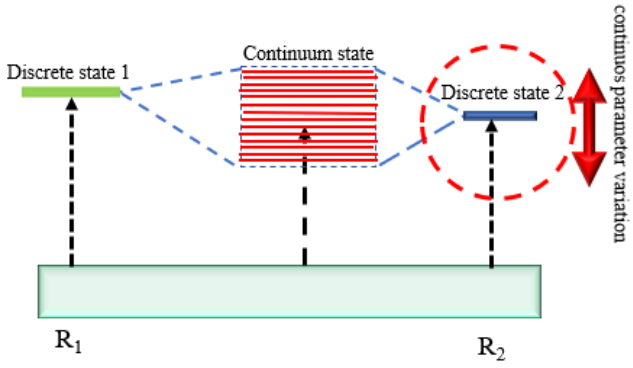

Fig. 5.4. Schematic illustration of the potential for strong coupling between two Fano resonances sharing the same continuum state.

Following the approach outlined in Ref. [15], we can describe the anti-crossing behavior (strong coupling) observed in the energy dispersion plot when two resonances interact with a radiation continuum. Similar to the quantum mechanical case, we can model this interaction using a non-Hermitian Hamiltonian for coupled optical resonances, neglecting nonradiative damping terms [16, 17]. The rigorous theoretical framework for this approach was established by Friedrich and Wintgen [18].

$$H = \begin{pmatrix} E_1 & k \\ k & E_2 \end{pmatrix} - \mathrm{i}\begin{pmatrix} \gamma_1 & e^{i\psi}\sqrt{\gamma_1\gamma_2} \\ e^{i\psi}\sqrt{\gamma_1\gamma_2} & \gamma_2 \end{pmatrix} = \begin{pmatrix} E_1 - i\gamma_1 & k - \mathrm{i}e^{i\psi}\sqrt{\gamma_1\gamma_2} \\ k - \mathrm{i}e^{i\psi}\sqrt{\gamma_1\gamma_2} & E_2 - i\gamma_2 \end{pmatrix} \qquad (5.2)$$

In this Hamiltonian, E_1 and E_2 represent the resonance energy levels of the two coupled modes, γ_1 and γ_2 are the corresponding radiative damping rates, characterizing the energy loss of each mode due to radiation, k signifies the internal coupling strength between the modes, quantifying their near-field interaction. The term $\sqrt{\gamma_1\gamma_2}$ represents the radiative coupling between the modes, arising from their far-field interaction. ψ denotes the phase difference

between the two modes' radiating waves. The parameter $e^{i\psi}\sqrt{\gamma_1\gamma_2}$ captures the critical concept of interference between the radiating waves due to far-field coupling [19].

The eigenvalues of the non-Hermitian Hamiltonian (Eq. 5.2) are obtained by solving the secular equation, leading to the following solutions:

$$\bar{E}=\frac{E_1+E_2}{2}-\mathrm{i}\frac{\gamma_1-\gamma_2}{2}\pm\frac{1}{2}\sqrt{\left(\frac{E_1-E_2}{2}-\mathrm{i}\frac{\gamma_1-\gamma_2}{2}\right)^2+(k-\mathrm{i}e^{i\psi}\sqrt{\gamma_1\gamma_2})^2} \qquad (5.3)$$

Equation (5.3), as established by Friedrich and Wintgen [24], represents two avoided photonic bands within the parameter space. It yields two distinct energy solutions for E_1 and E_2. Fixing one energy value (e.g., E_1 = 1.5) and continuously varying the other (E_2) in the energy dispersion plots reveals an avoided-crossing behavior (characteristic of strong coupling) due to the formation of hybridized states, often referred to as upper and lower polaritons.

Figure 5.5 visualizes these avoided crossings for different coupling strengths (k = 0.01, 0.1, 0.2, and 0.5) when E_1 is held constant at 1.5 (arbitrary units), with γ_1 = 0.1 and γ_2 = 0.2.

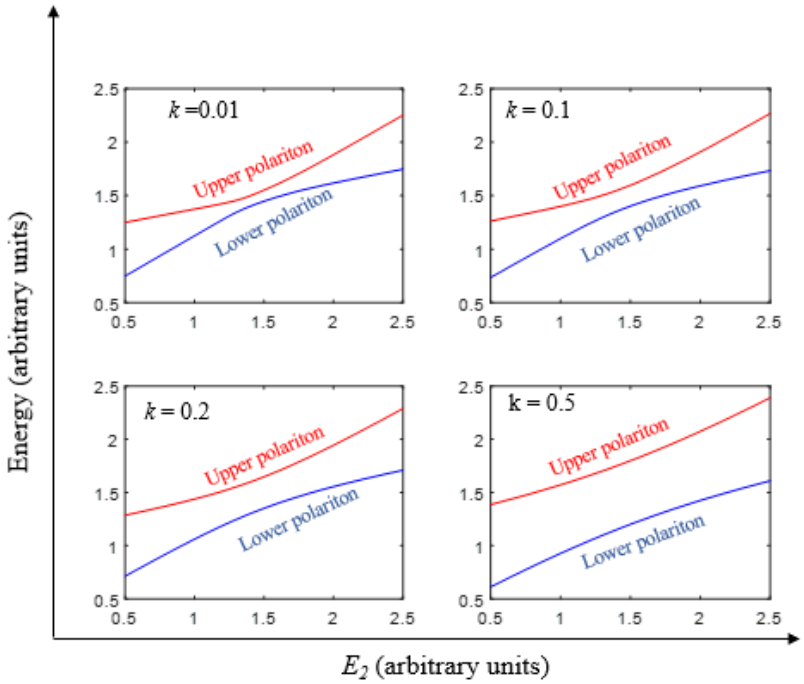

Figure 5.5: Anti-crossings due to strong coupling in energy dispersion plots. This figure shows the anti-crossings arising from strong coupling between two energy resonance states. These anti-crossings manifest as the splitting of the original resonance into upper and lower polariton branches. The splitting is visualized through the eigenvalues (E_1 and E_2) obtained from the non-Hermitian Hamiltonian. These eigenvalues correspond to the resonance energy levels of the two coupled modes. The plots illustrate the behavior for different coupling strengths (k) of 0.01, 0.1, 0.2, and 0.5. Here, E_1 is held constant at 1.5 (arbitrary units), while E_2 is continuously varied. The values of the radiative damping rates are $\gamma_1 = 0.1$ & $\gamma_2 = 0.2$.

5.3. Refractive index tuning for mode coupling and Rabi Splitting in hybrid metasurfaces

Three-dimensional (3D) megastructures, typically composed of metals and dielectrics, offer versatile light manipulation capabilities at the subwavelength scale. However, their complex

design and fabrication challenges make them less favorable for integration into photonic devices. Metasurfaces, their two-dimensional (2D) counterparts, offer a simpler and more practical alternative. They achieve comparable light manipulation at the subwavelength scale with established fabrication techniques and easier integration.

Fano resonances and Rabi splitting observed in photonic and metamaterial nanostructures have attracted significant interest due to their potential applications in sensing, quantum information storage, and processing. Fano resonances arise from the interaction of a discrete quantum state with a continuum band state, resulting in an asymmetric linewidth in the spectral response [20]. Rabi splitting, on the other hand, occurs when the coupling between an excitation state and a resonance state causes their energy levels to repel, leading to their splitting [20-22].

All-dielectric metasurfaces composed of high-refractive-index nanostructures can exhibit Fano resonances. These structures have been explored for various applications, both experimentally and theoretically [22]. They can excite both electric dipoles (EDs) and magnetic dipoles (MDs) at the nanoscale due to their dimensions. The observed Fano resonances arise from the interaction of these EDs and MDs originating from the metasurface structures. This interaction, similar to that in high-index dielectric nanostructures, involves resonant dark and corresponding bright modes [21]. An example is the experimentally realized Fano resonance in a binary silicon nanodisk array within the visible range [21]. Additionally, Xu et al. investigated strongly directional Fano resonance in an individual silicon nanorod using numerical simulations [22].

Several studies have explored the simultaneous realization of both Fano resonance and Rabi splitting. Liu et al. theoretically and experimentally investigated both phenomena using 3D

asymmetric split-ring resonators (aSRRs) made of gold [23]. Similarly, Zhang et al. achieved both Fano resonance and Rabi splitting numerically using a metal-dielectric-metal (MDM) plasmonic waveguide with stub resonators [24].

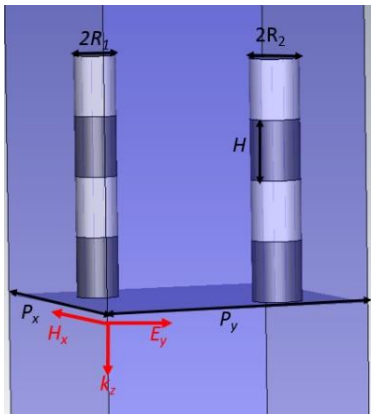

Figure 5.6. Schematic of a single unit cell. The unit period is 550 nm in *x*- and *y*-directions ($p_x = 550$ nm and $p_y = 550$ nm). Dark grey layers are dielectric segments, and light grey layers are silver. The height of each layer is fixed to H = 120 nm, R_1 = 30 nm, R_2 = 50 nm. We vary the refractive index of the dielectric segments. The structure has silica as substrate and index-matching oil superstrate

This work presents the resonant response of plasmonic-dielectric hybrid metasurfaces obtained using CST full-wave simulation modeling with electric field polarization in the *y*-direction. We design scattering elements out of multilayer silver-dielectric nanostructures and study periodic arrays of such scatterers (Fig. 5.6). These multi-segment nanostructures enable subwavelength light confinement [25]. Unit cells (lattice units) contain either one or two scattering elements. We demonstrate that the dielectric scatterer's refractive index determines whether identical or mismatched resonances are excited in the array. A slight mismatch in the

resonance positions, controlled by the dielectric scatterer refractive index, leads to the excitation of Fano resonances observed as peak splitting and characteristic asymmetric spectral profiles.

Our structure consists of a paired periodic array of silver-dielectric nanodisk metasurfaces. We observe Rabi splitting in the scattering parameters' spectral response due to the interaction between different Fano resonances, resulting in strong coupling and the observation of Rabi splitting within the nanostructure array. Figure 5.6 shows the schematic of the unit cell of the structure under study with the corresponding parameters used in the numerical simulations.

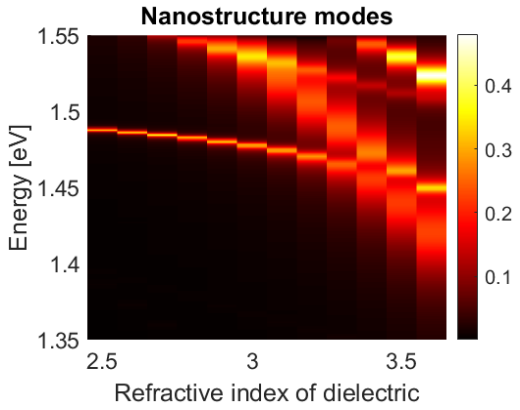

Figure. 5.7. Mode contours and their splitting due to significant coupling in the nanostructure. We show the comparison between the modes excited by nanoantennas made up of multilayer silver-dielectric with strong absorption in the unit cell of the nanostructure.

We investigate the electric field enhancement due to Fano resonances in the nanoantenna caused by changing the refractive index of the dielectric segments. This analysis demonstrates that the refractive index of the dielectric scatterer is responsible for the enhancement by tuning the refractive index of dielectric segments (Fig. 5.7). We observe the splitting of the modes due to significant coupling (Rabi splitting) as the dielectric refractive index is varied.

To sum up, we designed a hybrid Ag/dielectric nanopillar metasurface and observed Fano resonances and Rabi splitting in its spectral response. Surface plasmon polaritons, excited at the interface between Ag and dielectric structures, interact destructively with localized surface plasmon resonances and surface plasmon polariton modes, giving rise to the observed Fano resonances in the proposed metal-dielectric hybrid metasurface. The significant coupling between excitation states of plasmonic resonances leads to Rabi splitting in the nanostructure. This strong coupling, possible due to the interaction between nanopillar resonances and surface plasmon polaritons in the nanostructure arrays, leads to the anti-crossing behavior of the resonances. Finally, we observed that the spectral peaks of the Fano resonances can be effectively tuned by varying structural parameters like the refractive index of the dielectric scatterers.

5.4 Radius-dependent Rabi Splitting in plasmonic-dielectric metasurfaces

We investigate the emergence of Rabi splitting in the proposed hybrid plasmonic-dielectric metasurface (Figure 5.8(a)) due to the strong interaction between its nanostructure modes. This interaction arises from the constructive coupling between resonant dark and bright modes within the nanostructure.

The unit cell of the metasurface comprises two nanopillars, each containing four nanodisks (Figure 5.8(a)). Two of these nanodisks are plasmonic, fabricated from silver, while the other two utilize high-refractive-index silicon. All nanodisks possess a uniform height (H = 120 nm). One radius (R_1) is fixed at 50 nm, while the other radius (R_2) varies between 30 nm and 70 nm. The pairs are arranged periodically with a lattice constant (P) of 550 nm ($P_x = P_y = P$) in both x and y directions. The entire array is illuminated with x-polarized light at normal incidence.

Both the substrate and the superstrate surrounding the array are composed of silica. Since the elements are arranged in a periodic array, the metasurface supports collective resonances. These resonances are excited within periodic structures, with their properties heavily influenced by the periodicity of the array itself [26-29].

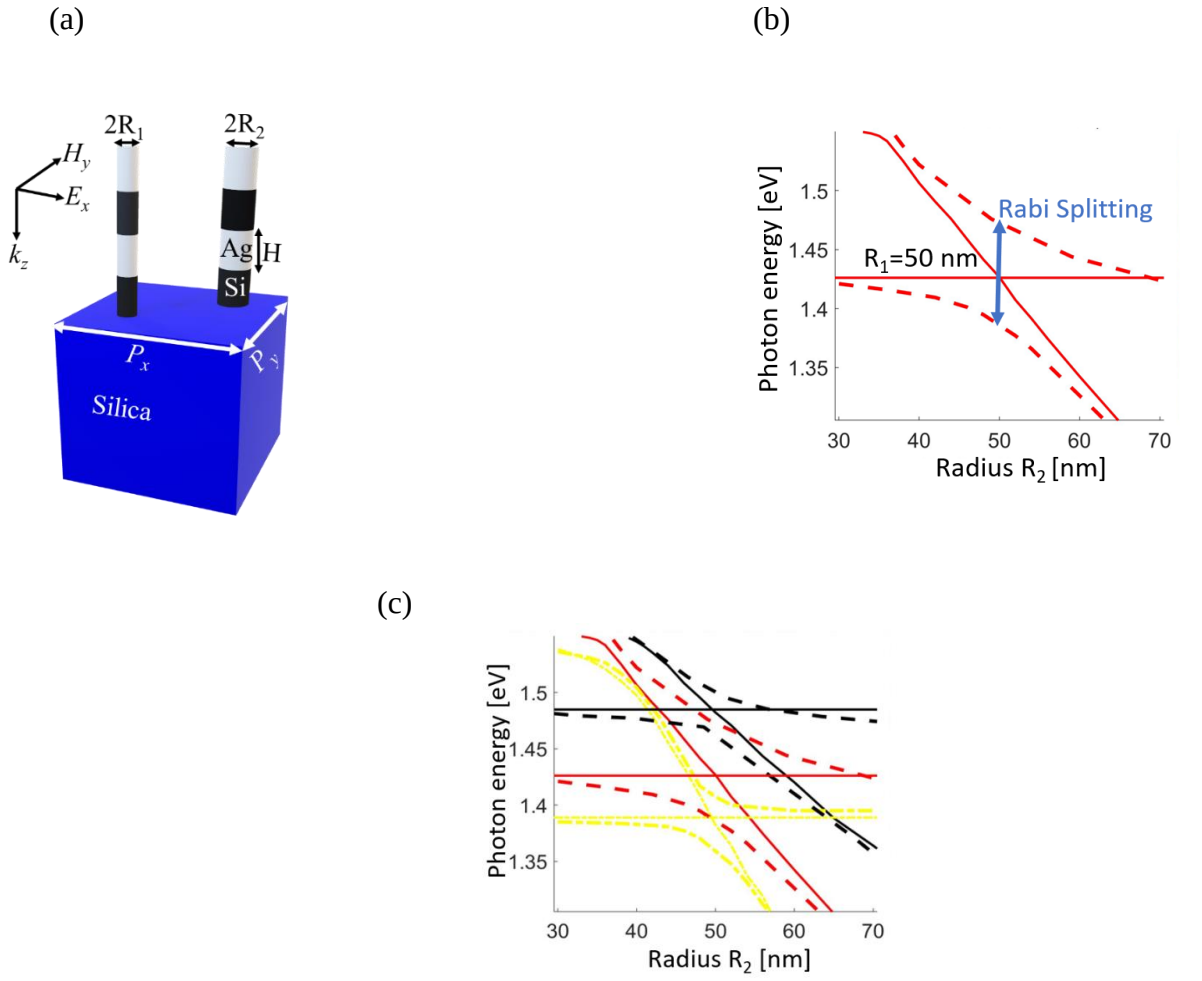

Figure 5.8. (a) Schematic of the proposed hybrid metasurface under consideration, where the unit cell consists of two elements (nanopillars). Each element has four nanodisks: two plasmonic made of silver and two made of high-refractive-index material, silicon. The nanodisks are of height H = 120 nm and radii R_1 = 50 nm (fixed) and R_2, varied from 30 to 70 nm. The pairs are arranged in periodic array with periods $P_x = P_y = P$ = 550 nm. The array is illuminated with the x-polarized light at the normal angle. The substrate and superstrate materials are silica. Considering the center of the unit cell has coordinates (0, 0), the first element has coordinates ($-P_x/4$, $-P_y/4$), and

the second element has coordinates (P_x/4, P_y/4). (**b**) Contours of one mode pair. The horizontal line corresponds to the mode in Element #1 (unchanged due to the constant R_1 = 50 nm), and the diagonal line corresponds to the mode in Element #2 that changes along with R_2. The solid lines are the results for a single element in the unit cell, while the dashed lines are the results of modeling two elements. (**c**) Contours of three pairs of the nanostructure modes. To better understand the nature of mode excitation, we utilize a nanostructure with only one element in the array's unit cell, as shown in Figure 5.8.

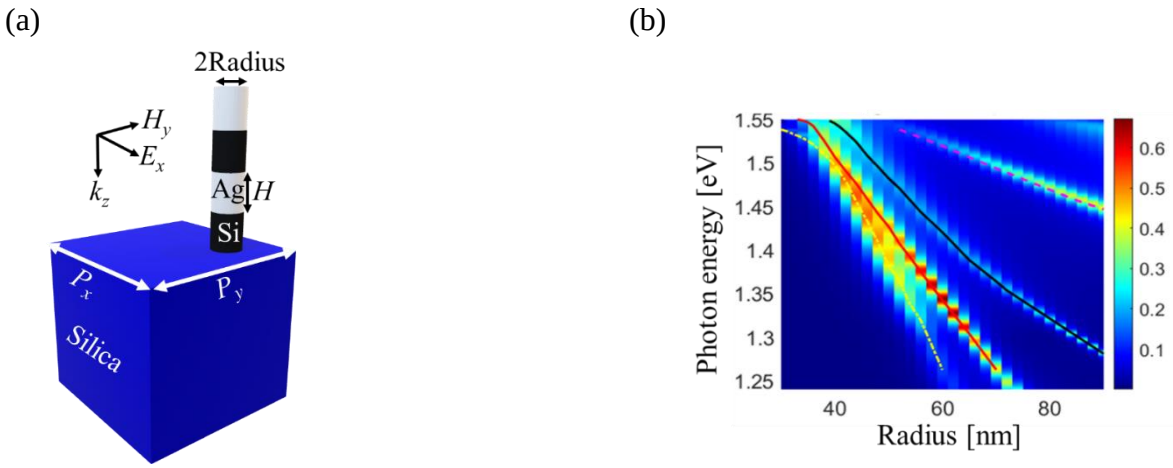

Figure 5.9. Nanostructure with one element. (**a**) Schematics of a single element in the unit cell. The element radius is *R*. Other geometrical parameters, materials, and illumination are the same as in the binary array. (**b**) Absorption for different radii. We perform calculations for a single element to aid in analyzing mode excitations in the binary array. Dot-dash yellow, solid red, and solid black lines are eyeball fit. They are subsequently transferred to Figure 1b,c to interpret the absorption mode maps.

By varying the element radius R and tracing the resulting modes that manifest as peaks in the absorption spectra, we are able to identify a consistent trend. Using a visual eyeball fit, we draw lines to represent the excited modes, with dot-dash yellow, solid red, and solid black lines indicating a nearly linear change in the mode position with changes in the element radius. These lines correspond to the solid diagonal lines in the figures for a binary array (Figure 5.8b,c), while the solid horizontal lines correspond to the case of a fixed radius R1 of 50 nm. Thus, the diagonal and horizontal solid lines in Figure 5.8b,c represent the results of the

calculations for an array with only one element in the unit cell. We performed a similar analysis of the absorption maxima for a binary array, akin to the case of a unit cell with only one element. Using an eyeball fit, we identified the excited modes, which are represented by dashed yellow, red, and black lines in Figure5.8 c. A key observation is an excellent agreement between the results obtained for a unit cell with only one element and those obtained for the binary array, which highlights the robustness of our analysis method. While the solid and dashed lines in Figure 5.8c come from two different types of simulations, we see that the dashed lines are the modes experiencing Rabi splitting because of the binary nature of the array. This observation is significant as it highlights the effects of lattice coupling on mode excitation and behavior. Figure 5.8b,c show mode energy maps with one mode pair only and three mode pairs, respectively. One can observe mode anticrossing as a result of the Rabi splitting due to the coupling of nanostructure modes. For instance, in Figure 5.8c, the Rabi splitting energy (shown in blue double-head arrows) is due to the strong coupling between nanostructure modes. One can observe triple anticrossings indicated in the dashed lines due to the splitting of the resonant modes in the nanostructure as a result of the strong coupling between different Fano resonances. Figure 5.8c illustrates three anticrossings in yellow, red, and black lines corresponding to triple Rabi splittings with energies 0.055, 0.08, and 0.025 eV, respectively.

5.5 References

[1] P. Forn-Díaz, L. Lamata, E. Rico, J. Kono, & E. Solano, "Ultrastrong coupling regimes of light-matter interaction," Reviews of Modern Physics, 91, 025005 (2019).

[2] D. Braak, "Integrability of the Rabi model," Physical Review Letters, 107, 100401 (2011).

[3] I. I. Rabi, "On the process of space quantization," Physical Review, 49(4), 324 (1936).

[4] D. S. Dovzhenko, S. V. Ryabchuk, Yu. P. Rakovich, & I. R. Nabiev, "Light–matter interaction in the strong coupling regime: Configurations, conditions, and applications," Nanoscale, 10, 3589-3605 (2018).

[5] Y. Wang & J. Y. Haw, "Bridging the gap between the Jaynes–Cummings and Rabi models using an intermediate rotating wave approximation," Physics Letters A, 379(8), 779-786 (2015).

[6] J. Koch, G. R. Hunanyan, T. Ockenfels, E. Rico, E. Solano, & M. Weitz, "Quantum Rabi dynamics of trapped atoms far in the deep strong coupling regime," Nature Communications, 14, Article 954 (2023).

[7] P. Törmä & W. L. Barnes, "Strong coupling between surface plasmon polaritons and emitters: a review," Reports on Progress in Physics, 78, 013901 (2015).

[8] K. Santhosh, O. Bitton, L. Chuntonov, & G. Haran, "Vacuum Rabi splitting in a plasmonic cavity at the single quantum emitter limit," Nature Communications, 7, Article ncomms11823 (2016).

[9] O. Bitton & G. Haran, "Plasmonic cavities and individual quantum emitters in the strong coupling limit," Accounts of Chemical Research, 55(12), 1659–1668 (2022).

[10] L. Lin et al., "Photoswitchable Rabi splitting in hybrid plasmon–waveguide modes," Nano Letters, 16(12), 7655-7663 (2016).

[11] Y. Shi et al., "Strong coupling between plasmonic surface lattice resonance and photonic microcavity modes," Photonics, 9(2), 84 (2022).

[12] Z. Liu et al., "Fano resonance Rabi splitting of surface plasmons," Scientific Reports, 7, Article 8010 (2017).

[13] B. Wang, X.-Z. Zeng, & Z.-Y. Li, "Quantum versus optical interaction contribution to giant spectral splitting in a strongly coupled plasmon–molecules system," Photonics Research, 8, 343-351 (2020).

[14] M. Pelton, “Introduction to metal-nanoparticle plasmonics,” John Wiley & Sons (2013).

[15] I. C. Seo et al., "Fourier-plane investigation of plasmonic bound states in the continuum and molecular emission coupling," Nanophotonics, 9, 4565–4577 (2020).

[16] C. W. Hsu et al., "Bound states in the continuum," Nature Reviews Materials, 1, 1–13 (2016).

[17] K. Koshelev et al., "Nonradiating photonics with resonant dielectric nanostructures," Nanophotonics, 8, 725-745 (2019).

[18] H. Friedrich & D. Wintgen, "Interfering resonances and bound states in the continuum," Physical Review A, 32, 3231 (1985).

[19] S. G. Lee, S. H. Kim, & C. S. Kee, "Bound states in the continuum (BIC) accompanied by avoided crossings in leaky-mode photonic lattices," Nanophotonics, 9, 4373-4380 (2020).

[20] M. F. Limonov, M. V. Rybin, A. N. Poddubny, & Y. S. Kivshar, "Fano resonances in photonics," Nature Photonics, 11, pp. 543-554 (2017).

21. [21] W. Zhao, X. Leng, & Y. Jiang, "Fano resonance in all-dielectric binary nanodisk array realizing optical filter with efficient linewidth tuning," Optics Express, 23(5), pp. 6858-6866 (2015).

[22] H. Xu et al., "Strongly Directional Fano Resonance in an Individual Silicon Nanorod," J. Phys. Chem. C, 124(48), pp. 26486-26492 (2020).

[23] Z. Liu et al., "Fano resonance Rabi splitting of surface plasmons," Scientific Reports, 7, Art. 8010 (2017).

[24] L. Zhang et al., "Fano resonance and Rabi splitting in MDM side-coupled cavities systems," Opt. Commun., 421, pp. 66-72 (2018).

[25] D. Bosomtwi, M. Osiński, & V. E. Babicheva, "Mode Coupling and Rabi Splitting in Transdimensional Photonic Lattices," 2020 IEEE 20th International Conference on Nanotechnology, pp. 107-110 (2020).

[26] V. E. Babicheva & A. B. Evlyukhin, "Resonant suppression of light transmission in high-refractive-index nanoparticle metasurfaces," Optics Letters, 43, 5186–5189 (2018).

[27] V. E. Babicheva, "Lattice effect in Mie-resonant dielectric nanoparticle array under the oblique light incidence," MRS Communications, 8, 1455–1462 (2018).

[28] V. E. Babicheva & A. B. Evlyukhin, "Interplay and coupling of electric and magnetic multipole resonances in plasmonic nanoparticle lattices," MRS Communications, 8, 712–717 (2018).

[29] A. Han, J. V. Moloney, & V. E. Babicheva, "Applicability of multipole decomposition to plasmonic- and dielectric-lattice resonances," The Journal of Chemical Physics, 156, 114104 (2022).

Chapter 6

Contents

6.0 Hot electron generation in plasmonics

This chapter examines the phenomenon of hot electron generation within the realm of plasmonics. The discovery of the photoelectric effect and its explanation by Einstein laid the groundwork for exploring how light interacts with matter at the quantum level, including the generation of hot electrons through plasmon excitation in metallic nanostructures [1]. This phenomenon lies at the intersection of quantum physics and materials science, involving the complex interaction between light and electrons on the nanoscale. Hot electron generation holds promise for technological advancements in various domains.

Surface plasmon polaritons (SPPs) are electromagnetic waves that propagate along the interface between a metal and a dielectric or air, typically in the infrared or visible light spectrum. These waves combine the properties of surface plasmons (charge density oscillations in the metal) and polaritons (electromagnetic waves in the dielectric) [2].

When light interacts with metallic nanostructures whose dimensions are comparable to or smaller than the incident light's wavelength, localized surface plasmon (LSPR) resonance is induced (Fig. 1(b)). Light absorption is enhanced when the light's frequency matches the LSPR resonance, which is characterized by the collective oscillation of the nanostructure's free electrons in response to the light. This creates a significant, time-varying dipole moment that interacts strongly with the incoming light's electric field. LSPs can decay radiatively, emitting photons, or non-radiatively through Landau damping, generating hot electrons (energetic electron-hole pairs) (Fig. 2(a)). These hot carriers play a crucial role in applications ranging from photocatalysis to photodetection [4].

Plasmonic nanostructures are captivating due to their ability to exhibit optical extinction cross-sections significantly larger than their physical size and generate exceptionally strong local electric fields under resonant conditions [5]. The resonant excitation and subsequent decay of localized surface plasmons (LSPs) lead to unique optical properties that have expanded applications in spectroscopy, photovoltaics, imaging, sensing, and photothermal therapy [6,7,8]. Notably, the generation of hot carriers through non-radiative decay processes, particularly via Landau damping, highlights the vast potential of these metallic nanostructures to drive progress in diverse fields. The high energy of these carriers allows them to overcome material interfaces, making them valuable for developing electronic devices and sensors [9].

Recent research has focused on enhancing hot-electron generation efficiency and utilization by designing novel materials and nanostructures. This includes efforts to gain a deeper theoretical understanding of the dynamics underlying hot electron phenomena induced by plasmons, encompassing their generation, transport, and decay [10,11].

Optimizing hot electron generation efficiency can be achieved through various strategies, such as modifying the nanostructure's shape, size, material composition, and the surrounding medium's refractive index [12,13]. Section 6.1 reviews the processes responsible for hot electron generation in plasmonic nanostructures.

Section 6.2 explores nanostructure designs that promote efficient hot electron generation from plasmonic effects. Here, we focus on periodically arranged gold nanoelectrodes that exploit surface lattice resonances (SLRs). SLRs enable the excitation of strong electric fields localized near the Rayleigh anomaly of the nanoelectrode array. Prior research has demonstrated that SLRs significantly enhance the extinction cross section of plasmonic nanostructures [14]. This

translates to a pronounced increase in light absorption at the nanoelectrode surface, thereby promoting hot electron generation into the surrounding aqueous environment.

6.1 Process of hot-electron Generation

Hot electron generation through plasmon excitation is a multi-step quantum mechanical process initiated by light absorption in metallic nanostructures [15]. When light interacts with these structures, it can excite surface plasmons (SPs) – collective oscillations of free electrons at the metal-dielectric interface (Fig. 1(a)) [16]. The energy and momentum of the incident light must match specific plasmon modes, which are influenced by the nanostructure's geometry and material properties [17].

Following light absorption, localized surface plasmon resonances (LSPRs) are excited (Fig. 1(b)). LSPRs concentrate light into sub-wavelength volumes, significantly enhancing the local electric field. This enhancement is crucial as it increases the probability of photon absorption, effectively converting light into plasmon oscillations [18]. Here, we adopt the process breakdown outlined by César Clavero [19] and utilize diagrams for clarity.

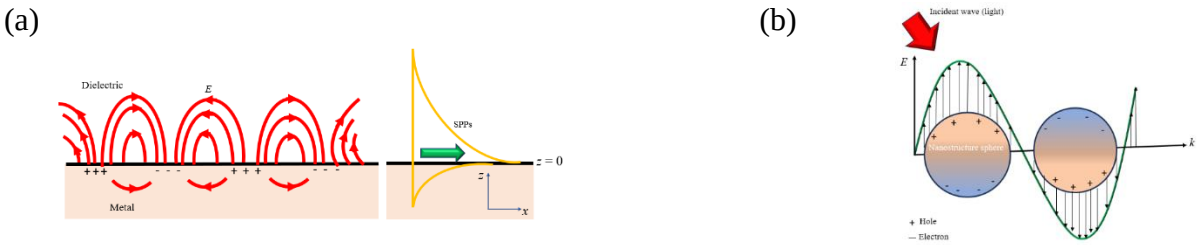

Figure 6.1. Surface plasmon polaritons (SPPs) and localized surface plasmon resonance (LSPR) **(a) Surface Plasmon Polaritons (SPPs):** This schematic depicts an evanescent electron density wave propagating at the interface between a metal and a dielectric medium. The collective motion of electrons generates an associated electromagnetic field (*E*), whose intensity decays exponentially with increasing distance from the interface. SPPs can be efficiently excited by visible light.

(b) Localized Surface Plasmon Resonance (LSPR): This illustration shows an LSPR occurring within a metallic nanoparticle induced by an external electric field. The electric field drives the coherent oscillation of delocalized electrons at the particle's surface, creating a localized resonance.

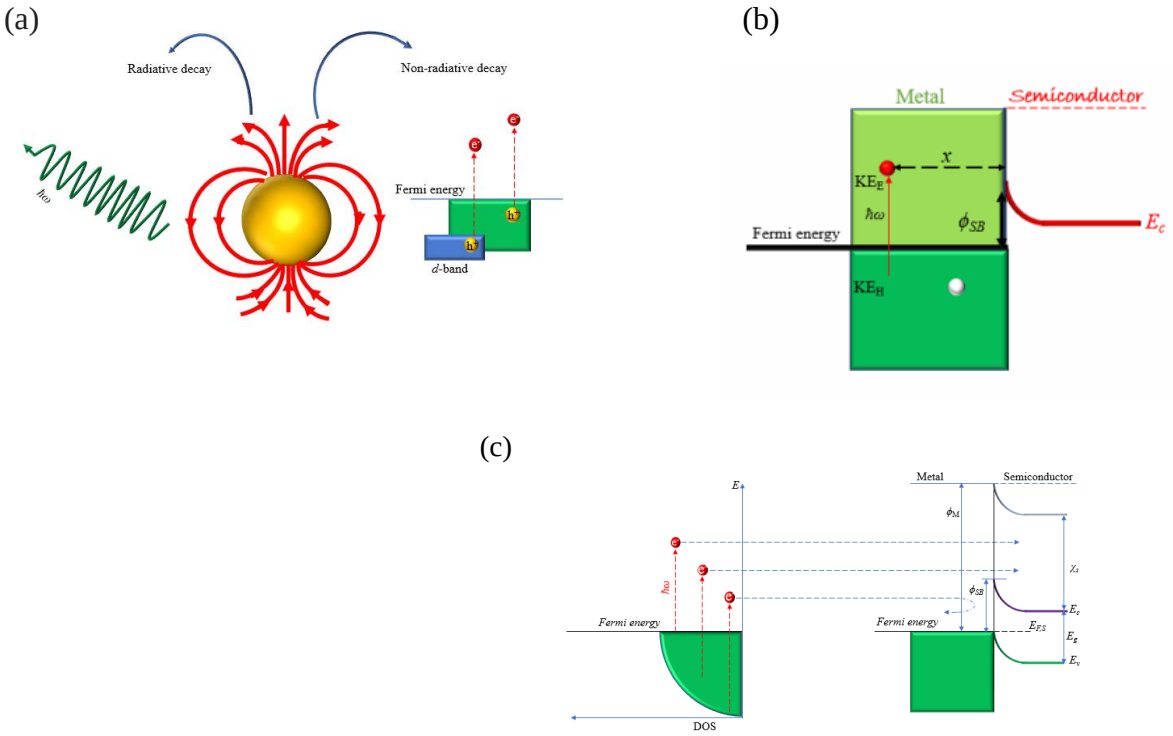

Figure 6.2: Surface Plasmon Decay and Hot-Electron Generation (a) Decay Mechanisms of Localized Surface Plasmons: Localized surface plasmons can decay through two primary mechanisms: radiative and non-

radiative. Radiative decay involves the re-emission of light (photons). In contrast, non-radiative decay occurs through energy transfer to electrons within the metallic nanostructure, generating "hot electrons." These hot electrons possess high kinetic energies exceeding the average thermal energy of the surrounding electrons. In noble-metal nanostructures, non-radiative decay can proceed via two main pathways: **Intraband Excitations:** Electrons are excited to higher energy states within the conduction band of the metal. **Interband Excitations:** Electrons undergo transitions from other occupied bands (such as *d*-bands) to the conduction band. (b) This schematic depicts energy band diagram of a plasmonic Schottky detector. When illuminated with light, localized surface plasmons are excited within the metallic nanostructure. These plasmons decay non-radiatively, generating "hot electrons" with kinetic energy (KE_E) exceeding the Fermi level. Correspondingly, "hot holes" are created with kinetic energy (KE_H) [20]. **(c) Plasmonic Hot-Electron Injection:** The energy stored in surface plasmons can be harnessed for various applications through the phenomenon of hot-electron injection. When a plasmonic nanostructure is placed in contact with a semiconductor, a Schottky barrier can form at the interface. This barrier arises due to the work function difference between the metal and the semiconductor. Hot electrons generated within the plasmonic nanostructure possess sufficient kinetic energy to overcome the Schottky barrier (ϕ_{SB}), enabling their injection into the conduction band (E_c) of the neighboring semiconductor. The value of the Schottky barrier depends on the work function (ϕ_M) of the metal and the electron affinity (χ_S) of the semiconductor.

Illuminated nanostructures exhibit rapid energy dissipation (within femtoseconds) driven by LSPR. This decay can be radiative (emitting light) or non-radiative (creating energetic electrons) (Fig. 6.2(a)). Non-radiative decay, particularly through Landau damping, plays a key role in hot electron generation. During this process, plasmon energy is directly transferred to an electron, pushing it above the Fermi level and generating an electron-hole pair with high kinetic energy (hot carriers).

In noble-metal nanostructures, non-radiative decay typically involves excitations within the conduction band or inter-band transitions, particularly involving *d*-bands. However, due to the significant energy gap between *d*-band levels and the Fermi level in materials like gold and

silver, intraband excitations dominate. Hot electrons then lose energy through interactions with other electrons and the lattice, eventually converting to heat.

Figure 6.2(b) illustrates the process of hot electron generation using the concept of the parabolic density of states (DOS) in the conduction band. Notably, in noble metals, surface plasmons can impart energies ranging from 1 eV to 4 eV to hot electrons, depending on nanostructure characteristics like carrier concentration, size, and shape.

A promising approach to utilize hot electrons involves creating a Schottky barrier between the metallic nanostructure and an n-type semiconductor (Fig. 6.2(b)). These semiconductors possess a high DOS in their conduction band, making them efficient electron acceptors and facilitating injection. Hot electrons with energies exceeding the Schottky barrier height (ϕ_{SB}) can be injected into the semiconductor's conduction band with varying efficiencies. Tunneling through the barrier is also possible, although less likely. Importantly, the energy required to overcome the Schottky barrier is significantly lower than the semiconductor's bandgap (E_g).

Once injected, the metallic nanostructure becomes positively charged due to electron depletion (Fig. 6.2(c)). Figure 6.2(c) depicts a simplified schematic of a surface plasmon detector. A plasmon with energy ($\hbar\omega$) generates hot electrons with kinetic energy (KE_E) above the Fermi level and holes with kinetic energy (KE_H). Electrons with sufficient energy can overcome the Schottky barrier (ϕ_{SB}) and be injected into the semiconductor's conduction band (E_c), contributing to the photocurrent. However, successful injection requires the electron to travel an unimpeded path (x) to the interface and possess a sufficiently low in-plane momentum component to enter the semiconductor. This avoids reflection analogous to total internal reflection in optics [20].

The critical factor is the significant momentum mismatch between the metal (where high kinetic energy aligns with the Fermi level, typically 5-6 eV in gold or silver) and the semiconductor (where hot electron kinetic energy is KE_E - ϕ_{SB}, or at most 1 eV).

The acceptance angle [21] is given by:

$$\Theta_a = Sin^{-1}\left[\sqrt{\frac{m_s(KE_E - \phi_{SB})}{m_0 E_F}}\right]$$

where m_s and m_o represent the effective masses in the semiconductor and metal, respectively. This typically results in an acceptance angle of 10-20 degrees. Consequently, overall injection efficiencies for carriers propagating in all directions are often below 1%. Therefore, analyzing the energy, spatial, and angular distributions of hot carriers generated by surface plasmon decay is crucial.

To maintain current flow and electrical continuity, an electron-donor solution or a hole-transporting material needs to be integrated with the nanostructures, facilitating hole transfer to the counter electrode.

6.2 Lattice effect for enhanced hot-electron generation in nanoelectrodes

The illumination of plasmonic-metal nanostructures and nanoparticles with light gives rise to collective oscillations of electrons at the interface of the nanostructures if the incident electromagnetic field matches the resonant frequency of collective electrons. This phenomenon generates intense electromagnetic fields known as localized surface plasmon resonance (LSPR). Recently, surface-plasmon-based nanostructures have been employed to concentrate and manipulate light, enhance light-matter interaction, and couple light energy to photonic devices at the nanoscale regime [22-24].

The excited plasmonic resonances undergo radiative and nonradiative decays. The far-field light scattering leads to radiative loss. In turn, plasmonic enhancement of the near electromagnetic field results in the interband and intraband transitions, which generate energetic (hot) electrons with very high kinetic energies [24]. In many cases, the generation of hot electrons in plasmonic nanostructures is attributed to the nonradiative decay of surface plasmon resonance through Landau damping [24,25]. Plasmon-generated hot electrons have attracted increased attention due to their ability to improve the efficiency of photovoltaic devices and photodetectors, photocatalysis for green fuels, photochemistry and electrochemical processes, photothermal heating, as well as their potential applications in optoelectronics and nonlinear optics [26-31].

The development of injection of plasmonic hot electrons into vacuum, solid, or liquid environments has been reported both numerically and experimentally by many research groups [33-39]. For instance, Dombi *et al.* reported numerical investigation of highly directional and monoenergetic plasmonic hot electrons into vacuum for ultrafast and high spatial resolution

applications [40]. Knight *et al.* experimentally investigated plasmonic hot electron injection into a semiconductor (silicon) for photodetection [41]. Boulais *et al.* reported investigations of plasma-mediated off-resonance plasmon-enhanced nanocavitation by the injection of plasmonic hot electrons from a gold nanosphere into water, induced by ultrafast laser radiation [42]. Zilio *et al.* used both numerical and experimental techniques to demonstrate that the energy transfer of plasmonic hot electrons from gold nanoelectrodes into water is more efficient in water than in vacuum (17 times higher), because free-electron clouds are more confined when injected hot electrons from the gold nanoelectrodes contact water molecules [43].

(a) (b)

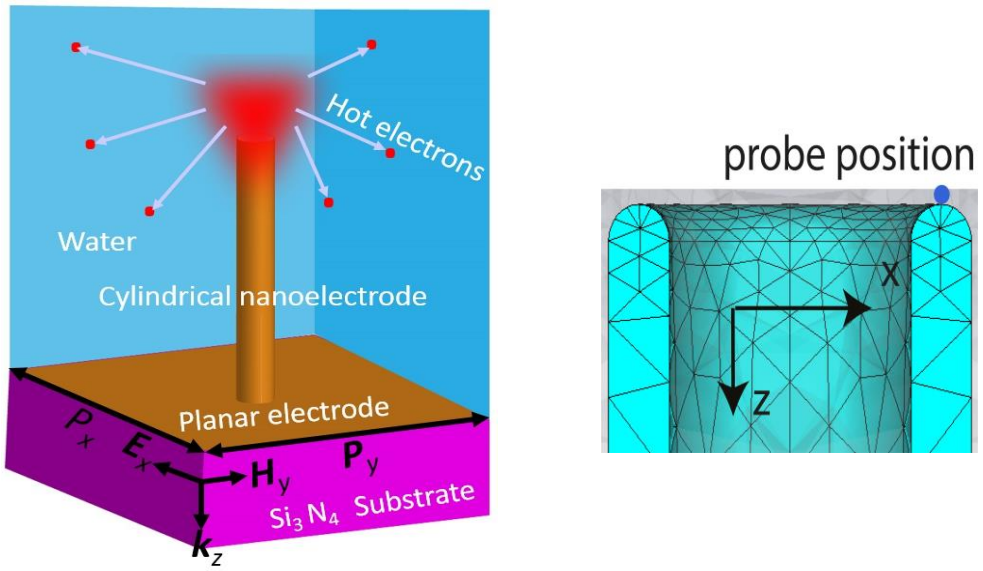

Figure 6.3. (a) Unit cell of the nanostructure under consideration. The period is $P = P_x = P_y$ in the x- and y-directions. The cylindrical gold nanoelectrode (nanotube) has a height of h = 1800 nm and an internal radius of 60 nm. The nanotube has 30-nm-thick walls, and it is connected to a planar gold electrode of 30-nm thickness. Both the nanotube and planar electrodes are immersed in water (upper half-plane) and are placed on a silicon nitride substrate. The wave propagates in the z-direction and is polarized in the x-direction. (b) Schematic of the mesh curvature in the numerical simulations and position of the probe for detecting electric field. Assuming the center of the nanotube is at $x_o = 0$ and $y_o = 0$, the probe is positioned at x_p = 75 nm and $y_p = 0$ and at the height of $z_p = h + 1$ nm = 1801 nm from the substrate surface or 1 nm above the nanotube.

A periodic array of metallic nanoparticles has been shown to support LSPR and possess diffractive behavior in the same spectral region [44-46]. The Rayleigh anomaly is defined as wavelengths at which a diffracted order appears or disappears at a grazing angle, and the diffractive effects are attributed to the interparticle lattice period. By tuning the interparticle lattice period, it is possible to excite lattice modes resulting from the hybridization of the LSPRs and lattice resonances in the proximity to the Rayleigh anomaly induced by the periodic arrangement of the nanostructure. When the lattice period is altered, one can achieve a rapid increase in the amplitude of the diffracted spectral orders resulting from the Rayleigh anomaly, and thereby generating intense electric field enhancement [47-50]. The very high-quality factors associated with plasmonic nanoparticle arrays due to diffractively coupled plasmon resonances can offer potential applications in the development of optoelectronics, photovoltaics, data storage, and biosensing [51].

Nanoelectrodes involving the injection of hot electrons have many potential applications in electrochemical sensing of single nanoparticles, chemical imaging of samples at the ultrahigh spatial resolution, development of plasmonic nanobubbles, and energy storage such as batteries and capacitors. Most importantly, such nanoelectrodes can be used, for example, as an *in vitro* platform for delivering a broad range of molecules into the intracellular compartment [39]. Injected hot electrons can be accelerated in the nanoantennas near-field and produce nanoscopic shockwaves opening membrane pores. This process allows avoiding nanobubbles, which are dangerous for biological cells. The microfluidic chip underneath the nanostructure allows bringing the required components to the targeted cell part.

Nanoelectrodes can be optical antennas (nanotubes) made up of either metals or semiconductors of nanometer dimensions. Plasmonic nanoantenna with a high aspect ratio can

support the excitation of multiple resonances because of its complex shape and possibility of excitation of higher-order modes [52]. Such three-dimensional vertical plasmonic gold nanoantennas (nanoelectrodes) can radiate in all directions and act as a metal reservoir [53,54]. This configuration also offers a stronger plasmonic response, higher field enhancement, longer carrier lifetime, and more efficient carrier generation and recombination.

Here, we report on a numerical study of a strong plasmonic field enhancement in a gold nanoelectrode array applied for hot-electron generation in a water environment. The schematic of the unit cell of the nanostructure under study is illustrated in Fig. 6.3a, with corresponding parameters used in numerical simulations. We show an excitation of the unique optical modes induced by the Rayleigh anomalies supported by the periodicity of the nanostructure and thereby enhancing the generation of plasmonic hot electrons. The modes are observed in the resonant absorptance and field enhancement in the nanostructure. We demonstrate the effect that can serve as a guideline for improving electric field enhancement and consequently stimulate the generation of plasmonic hot electrons from the nanoelectrodes in an aqueous environment.

In our design, both planar and nanotube electrodes are placed on a silicon nitride substrate, as shown in the schematic in Fig. 6.3a. To simulate the nanostructure, we consider a cylindrical gold nanoelectrode with an internal radius R and a height h. The nanoelectrode walls are 30-nm-thick. The nanoelectrode is positioned on a planar gold film of thickness 30 nm. We choose the same thickness for the walls of the plasmonic gold nanoantenna and planar electrode because of the specifics of the possible fabrication procedures [53]. For the same reason, the material of the cylindrical and planar electrodes is the same. In the fabrication of the cylindrical gold nanoantenna (nanoelectrode), a layer of insoluble resist is deposited on a silicon nitride

substrate. A thin layer of gold, whose shape is determined by the insoluble resist, is then deposited, covering the whole sample surface. As a result, the planar electrode is deposited at the same time as the nanotube, and because of it, they have a comparable thickness and the same material. The planar electrode also acts as a heat sink to decrease thermal effects resulting from electromagnetic heating of the plasmonic gold nanoantenna, generated due to resistive losses.

In the near-field zone, the electric field radiates in all directions at the tip of the nanoelectrode. To analyze the nanostructure's resonant behavior, we carry out full-wave numerical simulations using the finite-element method (FEM) implemented in CST Studio Suite frequency-domain solver. We use periodic boundary conditions in the *x*- and *y*-directions and domain with the same periodicity *P*. The structure is illuminated with a plane wave propagating along the *z*-direction and with the electric field polarized in the *x*-direction (electric field along the *x*-axis) at normal incidence. The top edge of the nanoelectrode is curved (Fig. 6.3b) to avoid artificial hot spots from artifacts of numerical simulations. We use data from Refs. 55,56 to define complex permittivities of gold and silicon nitride, and the refractive index of water is $n_w = 1.33$.

(a) (b)

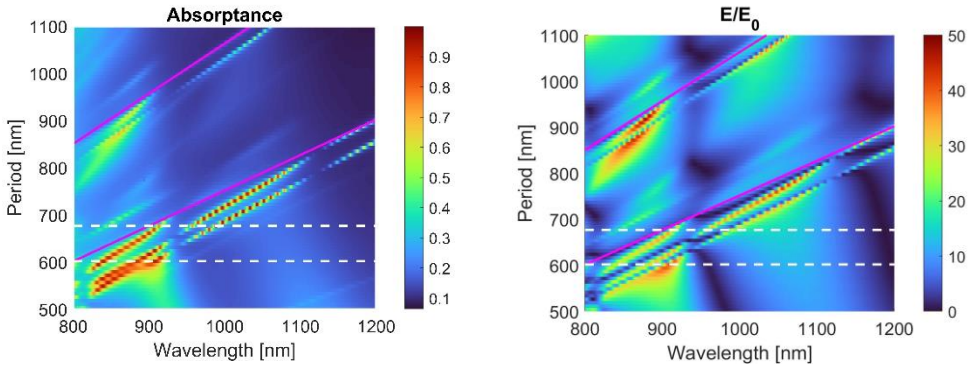

Figure 6.4. (a) Absorptance in the array of gold nanoelectrodes for different lattice periods *P*. The absorptance increase indicates spectral positions of modes excited in the nanostructure. The solid magenta lines indicate Rayleigh anomalies (1,0) and (1,1). The dashed white lines indicate periods *P* = 602 and 677 nm, analyzed in the figure that follows (see Fig. 6.5). See in Appendix for the simulation results in a broader range of periods and wavelengths. (b) The electric field enhancement E/E_0 in the array of gold nanoelectrodes for different lattice periods *P* at a particular probe position (see Fig. 1b). The enhancement reaches the values of up to 50 times in resonances following Rayleigh anomalies. The internal radius is *R* = 60 nm, and the height is *h* = 1800 nm.

Figure 6.4 illustrates the spectra maps of the absorptance and the electric field enhancement at a particular probe position indicated in Fig 6.3b, calculated for the plasmonic gold nanoantenna with a varying periodicity of the nanostructure *P*. Absorptance is defined as a ratio of optical power lost in the nanotube and planar electrode to the incident power. Absorptance in each nanostructure element is extracted from the simulation software package directly (settings "Specials" → "Calculate material power loss" → "Store per solid"). It does not require additional simulations as the software stores each solid's characteristics and material separately. While a significant portion of the absorbed incident power goes into heating rather than generating hot carriers [31], the latter is higher for higher absorptance. In our simulations,

the part of absorptance that is due to the silicon nitride substrate is negligible for the entire lattice period range under consideration. Some optical power is absorbed in the nanotube, and some in the planar electrode. The planar electrode absorptance is negligible for the lattice period larger than 677 nm (not presented here). On one side, with an increase of lattice period, a larger portion of the unit cell is occupied by the planar electrode, so its contribution to the absorptance increases proportionally with the increase of lattice period. However, on another side, the lattice with a period larger than 677 nm is sparse, and the nanotubes are positioned far away from each other. Absorptance in the planar electrode is defined mainly by the tails of the near field around the nanotubes. The sparse lattice result in weaker nanotube resonances, a smaller electric field around the nanotube and in the planar electrode, and therefore smaller absorptance in the planar electrode. Below those values, the absorptance due to the planar electrode is about 10 to 15% of the total. The absorptance in the nanostructure due to the nanotube is about 90%, leading to intense electric field enhancement and hence high generation of plasmonic hot electrons.

Absorptance is an integral characteristic that determines the spectral position of field enhancement in the whole structure (Fig. 6.4a). Alternatively, one can analyze an enhancement of the field at the specific point of the nanostructure (Fig. 6.4b), and one can identify places with the higher field enhancement. Whenever electric field enhancement is presented in our work, it is detected by a probe positioned as shown in Fig. 6.3b. To calculate the enhancement E/E_0 in the array, the electric field E at the probe position is normalized to the magnitude of the incident electric field in water E_0. We compare Figs. 6.4a and 6.4b as scan maps to Figs. 6.5a and 6.5b as linear profiles, and we see that peaks in both characteristics are in good agreement. It confirms that enhancement of the electric field at the probe position close to the

nanotube edge spectrally coincides with increases in absorptance for the whole structure. It also confirms that both absorptance and field enhancement can be used for identifying most efficient regimes for hot electron generation.

(a) (b)

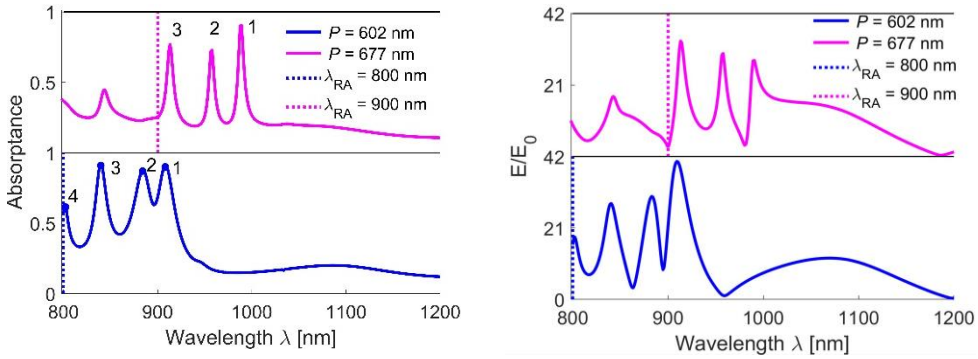

(c) #1 (d) #2 (e) #3 (f) #4 (g)

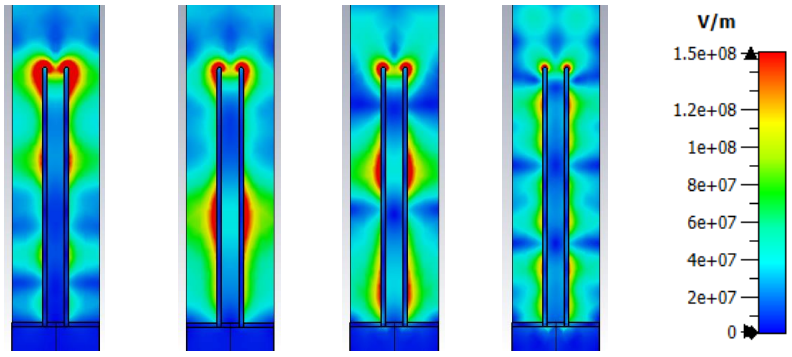

λ_1 = 908 nm λ_2 = 884 nm λ_3 = 840 nm λ_4 = 802 nm

Figure 6.5. (a) Absorptance and (b) electric field enhancement E/E_0 at a particular probe position (shown in Fig. 1b) in the array of gold nanoelectrodes for periods P = 602 and 677 nm. The dashed lines indicate Rayleigh anomalies (1,0): λ_{RA} = 800 nm for period P = 602 nm (blue dashed line) and λ_{RA} = 900 nm for period P = 677 nm (magenta dashed line). The spectra are shifted in the ordinate axis for clarity. Four resonances for P = 602 nm and three resonances for P = 677 nm are labeled for further discussion. (c)-

(f) Field distributions averaged over the wave oscillation cycle at the resonances #1-4 for P = 602 nm. The maps are shown in the *xz*-coordinate cross-section (for y = 0). (g) Color scale that corresponds to all resonances in panels (c)-(f). The internal radius of the nanotube is R = 60 nm, and the height is h = 1800 nm.

Tracing absorptance peaks is the most reliable way to interpret the nanostructure spectrum and identify the mode spectral position. Being an integral characteristic of field enhancement in the nanostructure, the absorptance profiles are accurate indicators of nanostructure modes and their resonances. If nanostructure modes do not couple with each other (*e.g.*, uncoupled dipole, quadrupole, etc., eigenmodes of a single nanoparticle), the absorptance profile is not subjected to interference effects, as opposed to reflection or transmission.

The sharp resonances are observed due to diffraction at the Rayleigh anomaly, resulting from collective plasmonic resonances in the nanostructure. By tuning the periodicity of the nanostructure, we can excite lattice resonances at the wavelength close to the Rayleigh anomaly. Since the nanoantennas are immersed in water with the refractive index n_w = 1.33, the resonance positions of absorptance and field enhancement occur at the wavelength close to $\lambda_{RA} = n_w P$, where λ_{RA} is the Rayleigh anomaly wavelength. We denote this Rayleigh anomaly (1,0), and because the lattice is square in our case, the notations (1,0) and (0,1) can be used interchangeably. The next Rayleigh anomaly for the square lattice appears at $\lambda_{RA} = n_w P/\sqrt{2}$, and we denote it as (1,1) Rayleigh anomaly. In the general case of rectangular lattice with periods P_x and P_y. and with normal light incidence, the spectral positions of Rayleigh anomalies can be found from the equation $(\frac{2\pi}{P_x} n_x)^2 + (\frac{2\pi}{P_y} n_y)^2 = k_w^2$, where n_x and n_y are the integers 0, ±1, ±2,…, and k_w is the propagation constant in the surrounding medium that corresponds to the Rayleigh anomaly (n_x, n_y), that is $k_w = 2\pi/\lambda_{RA}$. The case of an oblique incidence and different polarizations is discussed in [55].

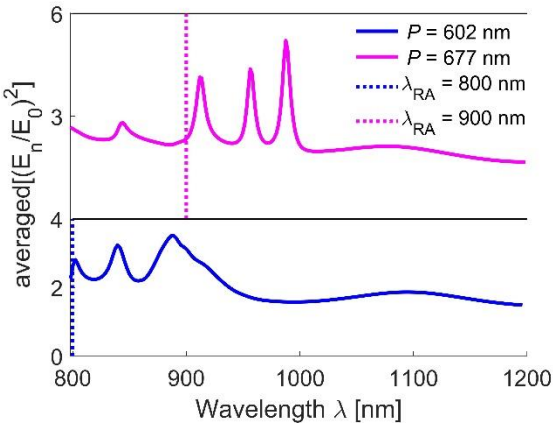

Figure 6.6. Normal electric field enhancement square $(E_n/E_0)^2$ averaged over the nanoelectrode surface in the array of gold nanoelectrodes for periods P = 602 and 677 nm. The dashed lines indicate Rayleigh anomalies (1,0): λ_{RA} = 800 nm for period P = 602 nm (blue dashed line) and λ_{RA} = 900 nm for period P = 677 nm (magenta dashed line). The spectra are shifted in the ordinate axis for clarity. The internal radius of the nanotube is R = 60 nm, and the height is h = 1800 nm.

Lattice resonances provide an additional degree of freedom and great flexibility in tuning the resonant response of the nanostructure. Because of the excitation of lattice resonances in the proximity to Rayleigh anomaly wavelength, one can adjust resonance wavelength by changing the period of the structure. One can see in Fig. 6.4a that resonances closely follow Rayleigh anomalies (1,0), (1,1), and higher-order (not presented here). In Fig. 6.5, we demonstrate the linear plots of the absorptance and field enhancement in the structure at two different lattice periods, P = 602 and 677 nm, and we study the effects on the nanostructure spectral response at these lattice periods. We observe that in the case of the smaller lattice period of 602 nm, there are slightly higher absorptance peaks compared to those for the lattice period of 677 nm. Also, we notice a slightly higher field enhancement for the lattice period of 602 nm than for the lattice period of 677 nm. Examples of spectra for two different periods, P = 602 and 677 nm, are shown in Fig. 6.5a. We deliberately choose lattice periods that result in multiple

resonances, and we show the change in resonance position with the shift of Rayleigh anomalies, λ_{RA} = 800 and 900 nm for the periods P = 602 and 677 nm, respectively (Figs. 6.5a, b).

Multiple resonances are excited because the nanotube supports modes of different orders due to its elongation. In the periodic array, these modes experience hybridization, which results in multiple lattice resonances. Figures 6.5c-f show the simulated electromagnetic field distribution around the plasmonic gold nanoantenna of lattice period P = 602 nm, where we observe an electric field enhancement in the proximity to Rayleigh anomaly λ_{RA} = 800 nm. Namely, there are four peaks with field profiles that correspond to the excitation of different modes. The results show strong electric field enhancement around the plasmonic nanoantenna along its walls and at the tip. Figures 6.5c-f depict the electric field distribution around the nanoantenna due to higher-order modes resulting from the coupling of these modes of plasmonic gold nanoantenna into diffractive orders of the lattice period. These resonances can be controlled by the lattice period and shifted altogether (see Fig. 6.4 and 6.5).

Most of the lattice resonances, whether they are excited in the arrays of nanoparticles of simple shapes, such as a sphere, or nanoantennas with rather complex modes, possess similar features with respect to Rayleigh anomaly tuning. When the Rayleigh anomaly is close to the resonance of a single nanoscatterer (nanoparticle, nanorod, nanotube, *etc.*), the lattice resonance is relatively broad and spectrally positioned at a distance from the Rayleigh anomaly [51]. When the array period increases, the lattice resonance gets narrower and moves spectrally closer to the Rayleigh anomaly. Higher-order resonances approach the Rayleigh anomaly faster, while lower-order resonances often move parallel to the Rayleigh anomaly in a large spectral range. One can see in Figs. 6.4a,b and 6.5a,b that resonances #1 and #2 shift parallel to the Rayleigh

anomaly (*i.e.*, remain at the same spectral distance for periods P = 602 and 677 nm), resonances #3 moves spectrally much closer to the Rayleigh anomaly for period P = 677 nm in comparison to its spectral position for period P = 602 nm, and resonance #4 disappears for periods P = 677 nm. A similar trend can be seen for higher-order Rayleigh anomaly (1,1) in Fig. 6.4.

Lattice resonances are narrow and appear as sharp features in the spectra. Besides them, one can see broader features, *e.g.*, minima at wavelengths around 800, 950, and 1180 nm (vertical dark regions in Fig. 6.4) and maxima at the wavelengths around 880 and 1080 nm for any period. These features do not have a resonant nature and are not of the Lorentzian line shape (see, *e.g.*, Fig. 6.5b, blue line for P = 602 nm for the wavelength range 960 - 1200 nm). Instead, these are interference patterns related to the reflection from the substrate and planar gold electrode of 30 nm thick. The interference brings an envelope function and modulates lattice resonance excitations.

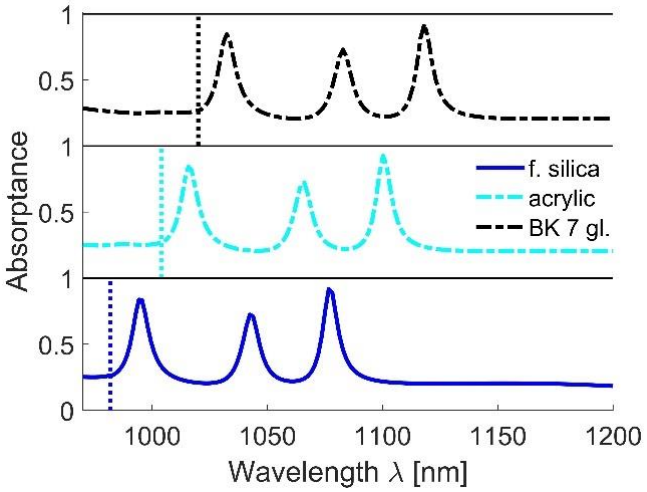

Figure 6.7. Lattice resonances for nanoelectrodes in a different environment. The uniform surrounding can be realized by means of the substrate and index-matching liquid in the upper half. We show examples for fused silica, acrylic, and BK 7 glass, using Cargille datasheets for the refractive indices [40]. The dashed lines indicate Rayleigh anomalies (1,0), and they are shifted because of the different material

indices. The period P = 677 nm and other geometrical parameters are the same as in Figs. 2 and 3. The spectra are shifted in the ordinate axis for clarity. The internal radius of the nanotube is R = 60 nm, and the height is h = 1800 nm.

Surface and volume photoelectric effects are competing causes of hot electron generation [16,37]. As discussed above, the total loss of optical power in the nanoelectrode defines the efficiency of the volume mechanism. Similarly, the normal electric field enhancement square $(E_n/E_0)^2$ averaged over the nanoelectrode surface defines the efficiency of the surface mechanism [36,57-59]. Absorptance in the nanostructure is chosen in Figs. 6.4 and 6.5 to predict the efficiency of hot electron generation. As a counterpart, in Fig. 6.6, we calculate the wavelength dependence of $(E_n/E_0)^2$ averaged over the nanoelectrode surface in the structure at two different lattice periods, P = 602 and 677 nm. Normal electric field E_n is an E field component normal to the nanotube's surface at each coordinate point. We further average its normalized square by integrating this characteristic over the entire nanotube surface and dividing this integral by the total nanotube surface. The total nanotube surface includes the outer and inner walls of the tube.

The normal electric field enhancement square $(E_n/E_0)^2$ averaged over the nanoelectrode surface (in Fig. 6.6) is about one order of magnitude smaller than the magnitude of E/E_0 at the probe position (in Fig. 5b). The reason is that the probe position is chosen at the nanotube edge, where the field enhancement is very strong. It is common for near fields in a plasmonic nanostructure to be significantly enhanced at the curved surfaces of the nanostructure. In contrast, the normal electric field enhancement square $(E_n/E_0)^2$ is an average characteristic and accounts for the regions in nanotube with smaller field enhancement.

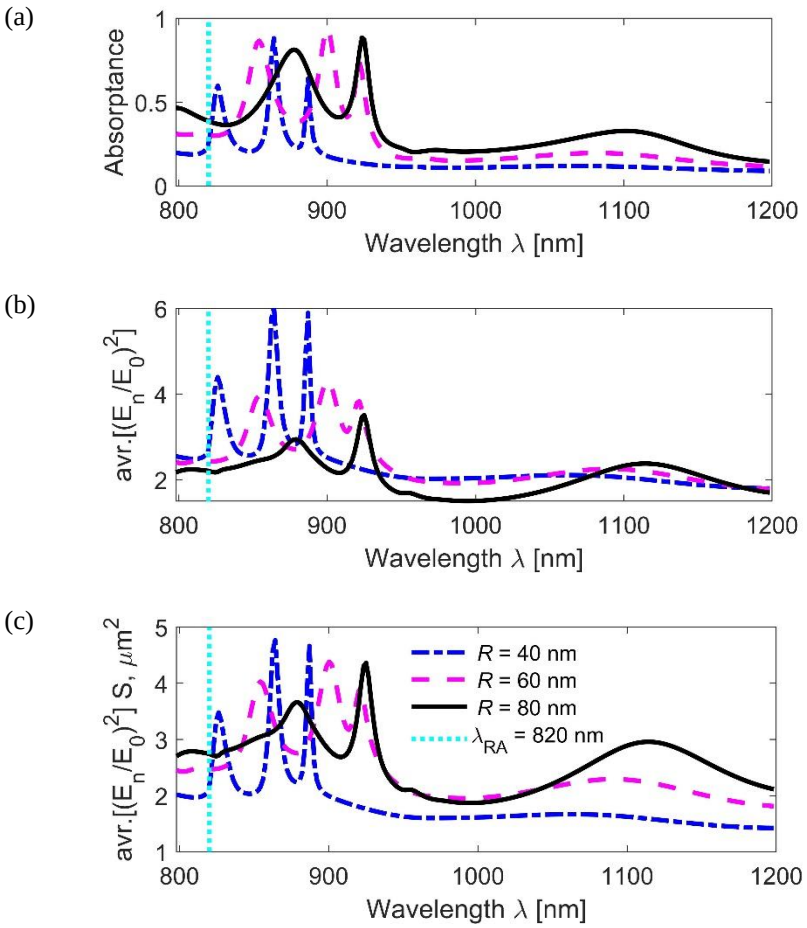

Figure 6.8 Change in absorptance and averaged field enhancement under variations of the internal radius of nanotube *R*. (a) Absorptance; (b) Normal electric field enhancement square $(E_n/E_0)^2$ averaged over the nanoelectrode surface; (c) Same as (b) but multiplied by nanotube surface area for an accurate comparison of surface photoemission efficiency. The legend is the same for all three panels. The period P = 616 nm. The dashed lines indicate Rayleigh anomalies (1,0): λ_{RA} = 820 nm for period P = 616 nm. The nanotube height is h = 1800 nm.

In Fig. 6.6, peaks #1 and #2 are very close to each other, and they are indistinguishable because of their broad linewidth. Nevertheless, results in Figs. 6.5 and 6.6 have the qualitative agreement, and we see that the peaks are spectrally positioned at the same wavelength. It confirms that the lattice resonances can increase the efficiency of hot-electron generation

regardless of whether the surface or volume mechanism dominates in the photoelectric effect. Excitation of lattice resonances results in a more prominent field enhancement in the nanostructure, which, in turn, produces more hot electrons.

Lattice resonances are stronger in the case of a uniform environment or when substrate and superstrate have close or equal refractive indices [51]. For this situation, we choose three common examples of the substrate and corresponding index-matching liquid [60]: fused silica, acrylic, and BK 7 glass (Fig. 6.7). One can see from the simulation results that even a slight change in the refractive index (1.45, 1.48, and 1.51 for fused silica, acrylic, and BK 7 glass, respectively) of the surroundings results in a significant shift in the nanoelectrode resonance.

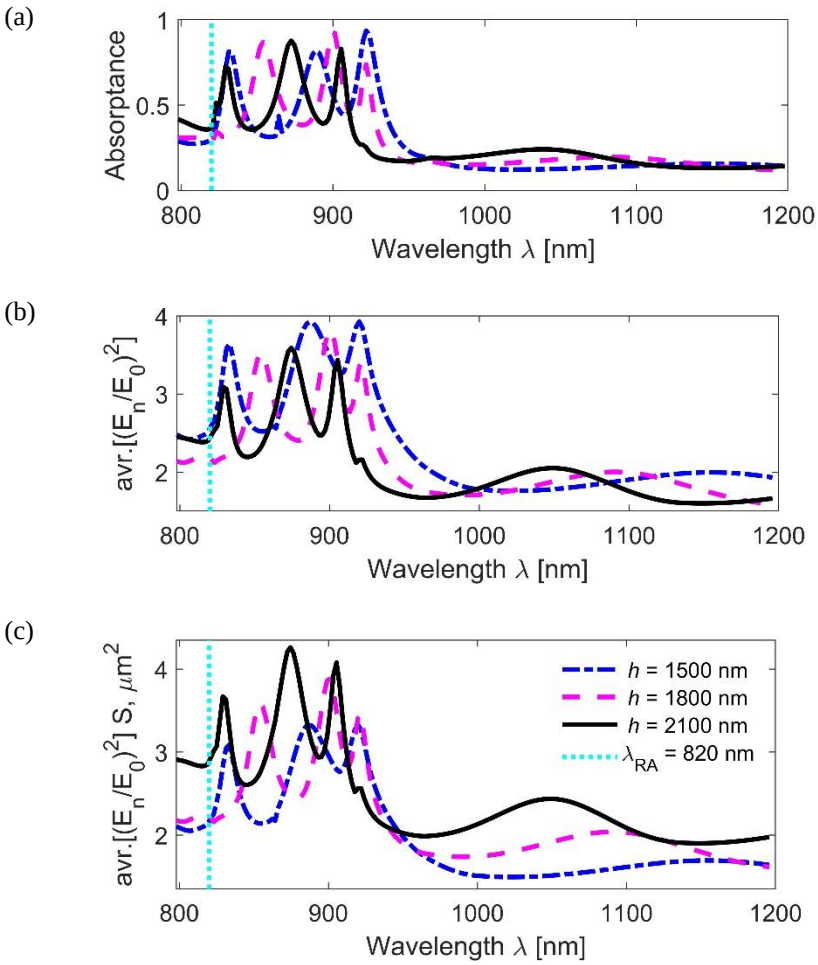

Figure 6.9. Change in absorptance and averaged field enhancement under variations of nanotube height h. (a) Absorptance; (b) Normal electric field enhancement square $(E_n/E_0)^2$ averaged over the nanoelectrode surface; (c) Same as (b) but multiplied by nanotube surface area for an accurate comparison of surface photoemission efficiency. The legend is the same for all three panels. The period P = 616 nm. The dashed lines indicate Rayleigh anomalies (1,0): λ_{RA} = 820 nm for period P = 616 nm. The internal radius of the nanotube is R = 60 nm.

The enhancement of the near field produced by the lattice resonances of arrays of metallic nanoparticles has been investigated extensively in recent years. In particular, it has been shown that for infinite arrays, the enhancement can be made arbitrarily large by appropriately designing the geometrical characteristics of the array [62]. Here, we aim to show the general mechanism of enhancing hot electron generation with the lattice resonances. We refrain from

optimizing the nanostructure, as this routine task can be performed at a later stage of engineering a particular practical application. Figures 6.8 and 6.9 indicate that the nanotube height and radius variations can result in more optimal hot electron generation. Varying the internal radius of the nanotube, we also change the external radius so that their difference remains at 30 nm. In Fig. 6.8, we see that using a larger radius, *e.g.*, R = 60 or 80 nm, results in a higher absorptance (panel (a)) and consequently more efficient volume photoemission. However, a smaller radius, *e.g.*, R = 40 nm, results in a larger normal electric field enhancement square $(E_n/E_0)^2$ averaged over the nanoelectrode surface and multiplied by the nanotube surface area (panel (c)). We use this characteristic for an accurate comparison of surface photoemission efficiency in the case of nanotubes with different radii and correspondently different surface areas. In Fig. 6.9, we see that a larger nanotube length facilitates more intense surface photoemission. Further optimizations, potentially involving machine learning algorithms, can be performed to identify specific nanostructure parameters targeting applications with a particular wavelength, material composition, and so on.

In conclusion, we have numerically studied the collective modes observed in the electric field enhancement and absorptance spectra in the plasmonic gold nanostructure. We have demonstrated that by selecting the array period comparable to the resonance wavelength, one can achieve high and narrow bandwidth absorptance and electric field resonances in the proximity of the Rayleigh anomaly in the nanostructure. We have shown intense electric field enhancement close to the Rayleigh anomaly wavelengths, consequently enhancing the generation of plasmonic hot electrons in the plasmonic gold nanoantenna (nanoelectrodes). We believe this novel approach for designing nanoelectrodes will be useful in researching and developing enhanced plasmonic hot-electron generation.

Figure 6.10 showcases the behavior of lattice modes across a wider range of wavelengths and periods.

(a)

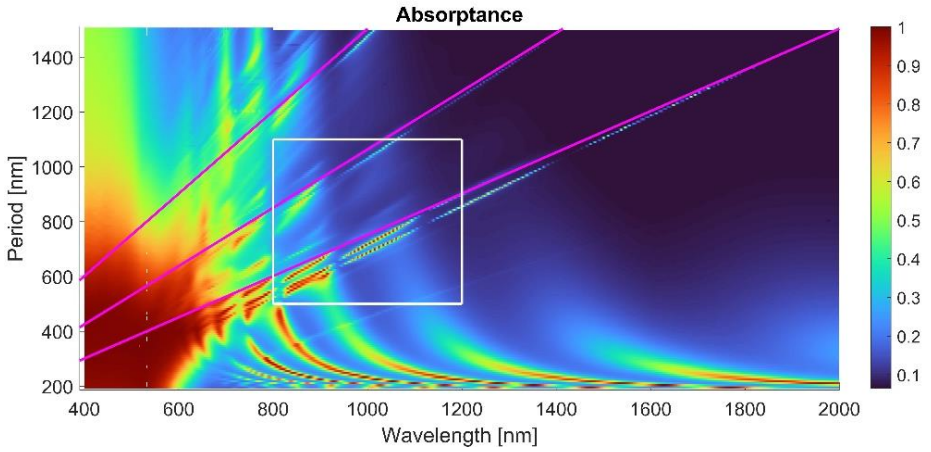

(b)

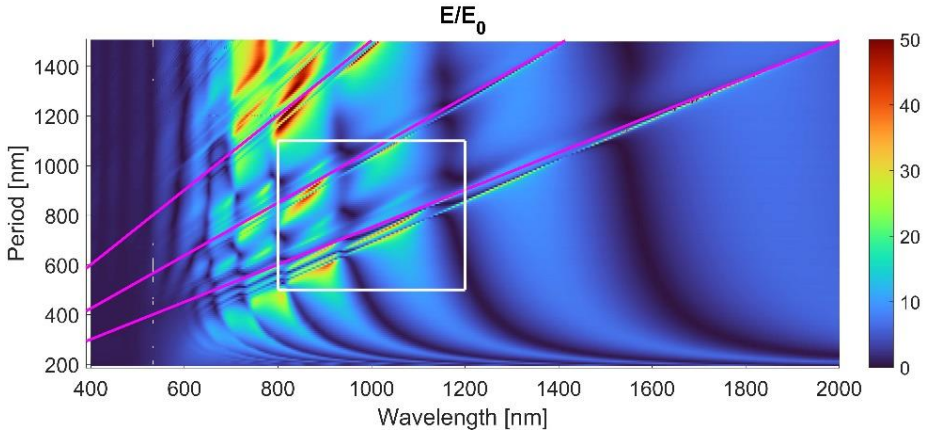

Figure. 6.10. Absorptance in the array of gold nanoelectrodes for different lattice periods *P*. Compared to Fig. 6.4, the range of wavelengths and periods is larger. The white rectangle shows the range of results in Fig. 6.4. (a) Absorptance map. (b) Electric field enhancement map.

6.3 References

[1] Albert Einstein, "Über einen die Erzeugung und Verwandlung des Lichtes betreffenden heuristischen Gesichtspunkt," Annalen der Physik, 322(6), 132–148 (1905).

[2] Shuwen Zeng, David Baillargeat, Ho-Pui Ho, and Kuan-Ting Yong, "Nanomaterials enhanced surface plasmon resonance for biological and chemical sensing applications," Chemical Society Reviews, 3426 (2014).

[3] K. L. Kelly, E. Coronado, L. L. Zhao, and G. C. Schatz, "The optical properties of metal nanoparticles: The influence of size, shape, and dielectric environment," The Journal of Physical Chemistry B, 107(3), 668–677 (2003).

[4] Weijia Li and Jeremy G. Valentine, "Harvesting the loss: surface plasmon-based hot electron photodetection," Nanophotonics, 6(1), 177–191 (2017).

[5] Wen Ou, Bo Zhou, Jun Shen, Chun Zhao, Yu Yuan Li, and Jun Lu, "Plasmonic metal nanostructures: Concepts, challenges, and opportunities in photo-mediated chemical transformations," iScience, 24, 101982 (2021).

[6] Harish Reddy and Vladimir M. Shalaev, "Plasmonic hot-carriers and their applications: Opinion," Optical Materials Express, 11(11), 3827–3832 (2021).

[7] H. Chalabi and M. Brongersma, "Harvest season for hot electrons," Nature Nanotechnology, 8, 229–230 (2013).

[8] Sung Wook Lee, "Hot electron-driven chemical reactions: A review," Applied Surface Science Advances, 16, 100428 (2023).

[9] Amin Sobhani, Matthew W. Knight, Yuecheng Wang, Bin Zheng, Nicholas S. King, Logan V. Brown, Zhifeng Fang, Peter Nordlander, and Naomi J. Halas, "Narrowband photodetection in the near-infrared with a plasmon-induced hot electron device," Nature Communications, 4, Article 1643 (2013).

[10] Luis V. Besteiro, Xiang-Tian Kong, Zhen Wang, Gregory Hartland, and Alexander O. Govorov, "Understanding hot-electron generation and plasmon relaxation in metal nanocrystals: Quantum and classical mechanisms," ACS Photonics, 4(11), 2759–2781 (2017).

[11] Esteban Y. Santiago, Luis V. Besteiro, Xiang-Tian Kong, Mauricio A. Correa-Duarte, Zhen Wang, and Alexander O. Govorov, "Efficiency of hot-electron generation in plasmonic nanocrystals with complex shapes: Surface-induced scattering, hot spots, and interband transitions," ACS Photonics, 7(10), 2807–2824 (2020).

[12] Xin Cui, Qi Ruan, Xing Zhuo, Xiaoyu Xia, Jiajia Hu, Rong Fu, Yongbo Li, Jianfang Wang, and Hong Xu, "Photothermal nanomaterials: A powerful light-to-heat converter," Chemical Reviews, 123(11) 6891–6952 (2023).

[13] Hailong Tang, Chih-Jen Chen, Zhiwen Huang, Jonathan Bright, Guihua Meng, Rong-Sheng Liu, and Nianqiang Wu, "Plasmonic hot electrons for sensing, photodetection, and solar energy applications: A perspective," The Journal of Chemical Physics, 152(22), 220901 (2020).

[14] V. G. Kravets, A. V. Kabashin, W. L. Barnes, and A. N. Grigorenko, "Plasmonic surface lattice resonances: A review of properties and applications," Chemical Reviews, 118(12), 5912–5951 (2018).

[15] Andrea Schirato, Marco Maiuri, Giulio Cerullo, and Giuseppe Della Valle, "Ultrafast hot electron dynamics in plasmonic nanostructures: Experiments, modelling, design," Nanophotonics, 12(1), 1–28 (2023).

[16] Huixia Shi, Xianzhe Zhu, Shuang Zhang, Guoliang Wen, Ming Zheng, and Hui Duan, "Plasmonic metal nanostructures with extremely small features: New effects, fabrication, and applications," Nanoscale Advances, 3(15), 4349–4369 (2021).

[17] Vera E. Babicheva, "Optical processes behind plasmonic applications," *Nanomaterials*, 13(7), 1270 (2023).

[18] Mark L. Brongersma, Naomi J. Halas, and Peter Nordlander, "Plasmon-induced hot carrier science and technology," Nature Nanotechnology, 10(1).

[19] Clavero, C. (2014). "Plasmon-induced hot-electron generation at nanoparticle/metal-oxide interfaces for photovoltaic and photocatalytic devices," Nature Photonics, 8, 95–103.

[20] Khurgin, J. B. (2019). "Hot carriers generated by plasmons: Where are they are generated and where do they go from there?" Faraday Discussions, 214, 35-58.

[21] M. Grajower, U. Levy, and J. B. Khurgin, "The role of surface roughness in plasmonic-assisted internal photoemission Schottky photodetectors," ACS Photonics, 5(10), 4030-4036 (2018).

[22] Kuang-Ta Lin, Hsin Lin, and Baojun Jia, "Plasmonic nanostructures in photodetection, energy conversion and beyond," Nanophotonics, 9(10), 3135–3163 (2020).

[23] Hao-Kai Yu, Ying-Sheng Peng, Yuxuan Yang, and Zhong-Yuan Li, "Plasmon-enhanced light-matter interactions and applications," npj Computational Materials, 5(1), 45 (2019).

[24] W. Li and J. G. Valentine, "Harvesting the loss: Surface plasmon-based hot electron photodetection," Nanophotonics, 6(1), 177–191 (2017).

[25] Harsha Reddy, Kebin Wang, Zakhar Kudyshev, Longxiang Zhu, Shuaidi Yan, Alberto Vezzoli, Stephen J. Higgins, Vikram Gavini, Alexandra Boltasseva, Pramod Reddy, Vladimir M. Shalaev, and Edgar Meyhofer, "Determining plasmonic hot-carrier energy distributions via single-molecule transport measurements," Science, 369(6502), 423–426 (2020).

[26] Shahin Memarzadeh, Jin-Bum Kim, Yusuf Aytac, Thomas E. Murphy, and Jeremy N. Munday, "Surface plasmon assisted control of hot-electron relaxation time," Optica, 7(6), 608–612 (2020).

[27] Carlos Clavero, "Plasmon-induced hot-electron generation at nanoparticle/metal-oxide interfaces for photovoltaic and photocatalytic devices," Nature Photonics, 8(2), 95–103 (2014).

[28] Yuxuan Yu, Zhi-Hong Ji, Shaojun Zu, Bo-Wei Du, Yu-Ming Kang, Zhi-Wei Li, Zhi-Kang Zhou, Kai-Bin Shi, and Zhi-Yuan Fang, "Ultrafast plasmonic hot electron transfer in Au nanoantenna/MoS2 heterostructures," Advanced Functional Materials, 26(35), 6394–6401 (2016).

[29] L. V. Besteiro, X.-T. Kong, Z. M. Wang, G. Hartland, and A. O. Govorov, "Understanding hot-electron generation and plasmon relaxation in metal nanocrystals: Quantum and classical mechanisms," ACS Photonics, 4(11), 2759–2781 (2017).

[30] Mark L. Brongersma, Naomi J. Halas, and Peter Nordlander, "Plasmon-induced hot carrier science and technology," Nature Nanotechnology, 10(1), 25–34 (2015).

[31] L. V. Besteiro, P. Yu, Z. M. Wang, A. W. Holleitner, G. V. Hartland, G. P. Wiederrecht, and A. O. Govorov, "The fast and the furious: Ultrafast hot electrons in plasmonic metastructures: size and structure matter," Nano Today, 27, 120–145 (2019).

[32] Yonatan Dub and Yonatan Sivan, "“Hot” electrons in metallic nanostructures–non-thermal carriers or heating?" Light: Science & Applications,8(1), 89 (2019).

[33] Mohammad Sistani, Matthias G. Bartmann, Nicola A. Gusken, Rupert F. Oulton, Hamed Keshmiri, Minh Anh Luong, Zahra S. Momtaz, Marcel I. D. Hertog, and Andreas Lugstein, "Plasmon-driven hot electron transfer at atomically sharp metal-semiconductor nanojunctions," ACS Photonics, 7(7), 1642–1648 (2020).

[34] Peter Dombi, Alexander Horl, Peter Racz, Istvan Marton, Alexander Trugler, Johannes R. Krenn, and Ulrich Hohenester, "Ultrafast strong-field photoemission from plasmonic nanoparticles," Nano Letters, 13(2), 674–678 (2013).

[35] Amirreza Ahmadivand, Rohit Sinha, Prashanth Kumar Vabbina, Mustafa Karabiyik, Seda Kaya, and Nezih Pala, "Hot electron generation by aluminum oligomers in plasmonic ultraviolet photodetectors," Optics Express, 24(12), 13665–13678 (2016).

[36] V. E. Babicheva, S. V. Zhukovsky, R. S. Ikhsanov, I. E. Protsenko, I. V. Smetanin, and A. Uskov, "Hot electron photoemission from plasmonic nanostructures: the role of surface photoemission and transition absorption," ACS Photonics, 2(8), 1039–1048 (2015).

[37] Giacomo Tagliabue, Adam S. Jermyn, Ruzan Sundararaman, Alexander J. Welch, J. Sebastian DuChene, Ruzan Pala, Amir R. Davoyan, Prineha Narang, and Harry A. Atwater,

"Quantifying the role of surface plasmon excitation and hot carrier transport in plasmonic devices," Nature Communications, 9(1), 3394 (2018).

[38] Stefano Neretina, Wei Qian, Eunice Dreaden, Mostafa A. El-Sayed, Robert A. Hughes, J. Scott Preston, and Pascal Mascher, "Plasmon field effects on the nonradiative relaxation of hot electrons in an electronically quantized system: CdTe-Au core-shell nanowires," Nano Letters, 8(8), 2410–2418 (2008).

[39] Gianluca C. Messina, Marco Dipalo, Rosaria L. Rocca, Pietro Zilio, Valeria Caprettini, Ruzan P. Zaccaria, Alessandro Toma, Francesco Tantussi, Laura Berdondini, and Francesco de Angelis, "Spatially, temporally, and quantitatively controlled delivery of broad range of molecules into selected cells through plasmonic nanotubes," Advanced Materials, 27(44), 7145–7149 (2015).

[40] Peter Dombi and Peter Raez, "Ultrafast monoenergetic electron source by optical wavefront of surface plasmons," Optics Express,16(5), 2887–2893 (2008).

[41] Matthew W. Knight, Hamed Sobhani, Peter Nordlander, and Naomi J. Halas, "Photodetection with active optical antennas," Science, 332(6030), 702–704 (2011).

[42] Etienne Boulais, Réal Lachaine, and Michel Meunier, "Plasma mediated off-resonance plasmonic enhanced ultrafast laser-induced nanocavitation," Nano Letters, 12(9), 4763–4769 (2012).

[43] Pietro Zilio, Marco Dipalo, Francesco Tantussi, Gianluca C. Messina, and Francesco de Angelis, "Hot electrons in water: Injection and ponderomotive acceleration by means of plasmonic nanoelectrodes," Light: Science & Applications, 6(6), e17002 (2017).

[44] V. E. Babicheva and A. B. Evlyukhin, "Resonant lattice Kerker effect in metasurfaces with electric and magnetic optical responses," Lasers & Photonics Reviews, 11(6), 1700132 (2017).

[45] Jui-Hung Yang, Victoria E. Babicheva, Ming-Wei Yu, Tsung-Chieh Lu, Tsung-Ru Lin, and Kun-Ping Chen, "Structural colors enabled by lattice resonance on silicon nitride metasurfaces," ACS Nano, 14(5), 5678–5685 (2020).

[46] Chien-Yao Yang, Jui-Hung Yang, Zong-Xuan Yang, Zheng-Gao Sun, Victoria E. Babicheva, and Kun-Ping Chen, "Nonradiating silicon nanoantenna metasurfaces as narrowband absorbers," ACS Photonics, 5(7), 2596–2601 (2018).

[47] Victoria E. Babicheva and Andrey B. Evlyukhin, "Metasurfaces with electric quadrupole and magnetic dipole resonant coupling," ACS Photonics, 5(5), 2022–2033 (2018).

[48] David Khopin, Fabian Laux, William P. Wardley, Julien Martin, G. Augusto Wurtz, Julien Plain, Nicolas Bonod, Anatoly V. Zayats, Wolfgang Dickson, and David Gerard, "Lattice modes and plasmonic linewidth engineering in gold and aluminum nanoparticle arrays," Journal of the Optical Society of America B, 34(3), 691–700 (2017).

[49] V. I. Zakomirnyi, A. E. Ershov, V. S. Gerasimov, S. V. Karpov, H. Ågren, and I. L. Rasskazov, "Collective lattice resonances in arrays of dielectric nanoparticles: A matter of size," Optics Letters, 44(23), 5743–5746 (2019).

[50] V. I. Zakomirnyi, S. V. Karpov, H. Ågren, and I. L. Rasskazov, "Collective lattice resonances in disordered and quasi-random all-dielectric metasurfaces," Journal of the Optical Society of America B, 36(7), E21–E29 (2019).

[51] V. G. Kravets, A. V. Kabashin, W. L. Barnes, and A. N. Grigorenko, "Plasmonic surface lattice resonances: A review of properties and applications," Chemical Reviews, 118(12), 5912–5951 (2018).

[52] D. Bosomtwi, M. Osiński, and V. E. Babicheva, "Mode coupling and Rabi splitting in transdimensional photonic lattices," Proceedings of the 20th IEEE International Conference on Nanotechnology (IEEE-NANO 2020), 107–110 (2020).

[53] F. de Angelis, M. Malerba, M. Patrini, E. Miele, G. Das, A. Toma, R. Proietti Zaccaria, and E. Di Fabrizio, "3D hollow nanostructures as building blocks for multifunctional plasmonics," Nano Letters, 13(8), 3553–3558 (2013).

[54] M. Malerba, A. Alabastri, E. Miele, P. Zilio, M. Patrini, D. Bajoni, G. C. Messina, M. Dipalo, A. Toma, R. Proietti Zaccaria, and F. de Angelis, "3D vertical nanostructures for enhanced infrared plasmonics," Scientific Reports, 5(1), 16436–16438 (2015).

[55] K. Luke, Y. Okawachi, M. R. E. Lamont, A. L. Gaeta, and M. Lipson, "Broadband mid-infrared frequency comb generation in a Si3N4 microresonator," Optics Letters, 40(21), 4823–4826 (2015).

[56] P. B. Johnson and R. W. Christy, "Optical constants of the noble metals," Physical Review B, 6(12), 4370–4379 (1972).

[57] A. V. Uskov, I. E. Protsenko, R. S. Ikhsanov, V. E. Babicheva, S. V. Zhukovsky, A. V. Lavrinenko, E. P. O'Reilly, and H. X. Xu, "Internal photoemission from plasmonic nanoparticles: Comparison between surface and volume photoelectric effects," Nanoscale, 6(9), 4716–4727 (2014).

[58] G. V. Hartland, L. V. Besteiro, P. Johns, and A. O. Govorov, "What's so hot about electrons in metal nanoparticles?" ACS Energy Letters, 2(7), 1641–1653 (2017).

[59] S. V. Zhukovsky, I. E. Protsenko, R. S. Ikhsanov, I. V. Smetanin, V. E. Babicheva, and A. V. Uskov, "Transition absorption as a mechanism of surface photoelectron emission from metals," Physica Status Solidi RRL, 9(10), 570–574 (2015).

[60] V. E. Babicheva, "Lattice effect in Mie-resonant dielectric nanoparticle array under the oblique light incidence," MRS Communications, 8(4), 1455–1462 (2018).

[61] Specialized Optical Coupling (index matching) Liquids, [Online]. Available: https://www.cargille.com/matching-liquids/

[62] A. Manjavacas, L. Zundel, and S. Sanders, "Analysis of the limits of the near-field produced by nanoparticle arrays," ACS Nano, 13(9), 10682–10693 (2019).

Chapter 7

Conclusions

This dissertation explored the design of nanostructures using hybrid plasmonic-dielectric metasurfaces. By meticulously adjusting nanoantenna dimensions, we achieved the formation of multiple Fano resonances, bound states in the continuum (BICs), and strong couplings, culminating in the observation of Rabi splitting.

These findings illuminate the power of manipulating Fano resonances to induce strong interactions and generate new eigenstates (Rabi splitting). This knowledge unlocks the potential for a new generation of tunable devices, high-Q-factor resonators, and advanced optical filters.

Furthermore, the dissertation presents a novel nanostructure design with periodically arranged gold nanoelectrodes for efficient plasmonic hot electron generation. Numerical simulations revealed a critical link between array period, resonance wavelength, and generation efficiency. This approach offers valuable insights for future research on hot electron generation in aqueous environments.

Overall, this dissertation demonstrates the immense potential of hybrid plasmonic-dielectric metasurfaces and periodic nanostructures for manipulating light-matter interactions at the nanoscale. By highlighting their tunability, sensitivity, and selectivity, we have established a strong foundation for the development of advanced photonic devices and inspired future research in this exciting field.

Chapter 8

Future Work

This dissertation primarily explored the potential of multilayer plasmonic-dielectric metasurfaces for manipulating light at the nanoscale. While these structures offer exciting possibilities, their real-world application faces limitations due to inherent challenges with plasmonic materials. These limitations include high intrinsic losses, difficulties in integration with other photonic components, and complex fabrication processes. To overcome these limitations and broaden the applicability of the studied structures, future work proposes a strategic shift towards all-dielectric metasurfaces.

Proposed Material Composition Changes

High-Index Dielectric Layers: The current design utilizes plasmonic layers, which, despite their light manipulation capabilities, suffer from high optical losses and thermal instability. These issues are particularly detrimental for applications requiring high efficiency and durability. Future work proposes replacing these layers with high-index dielectric materials like silicon, germanium, or titanium dioxide. These materials offer low optical losses and support both electric and magnetic resonances, potentially enhancing efficiency and operational bandwidth.

Porous Silica Integration: The current dielectric component will be replaced with porous silica. This choice is motivated by its lower refractive index and unique structural properties that can introduce additional light-scattering mechanisms for finer control over light propagation. Additionally, porous silica offers improved compatibility with biological environments, making it advantageous for biosensing applications.

Advantages of All-Dielectric Metasurfaces

Simplified Fabrication and Integration: All-dielectric metasurfaces are compatible with standard lithographic techniques used in semiconductor manufacturing, simplifying the fabrication process. This compatibility facilitates easier integration with existing photonic circuits and electronic components, crucial for developing integrated photonic systems.

Enhanced Device Performance: By utilizing all-dielectric materials, the proposed metasurfaces aim to significantly reduce energy losses and increase the Q-factor of resonant elements. This improvement is vital for applications in laser technology, imaging systems, and advanced sensing where energy efficiency and signal clarity are paramount.

Broadened Application Spectrum: The introduction of porous silica and high-index dielectrics opens new avenues in applications ranging from non-invasive medical diagnostics to robust environmental sensing. The unique properties of these materials, such as chemical inertness and mechanical stability, extend the functional environment where these metasurfaces can be employed.

Research Objectives and Methodology

Future investigations will focus on optimizing the design and arrangement of the all-dielectric elements to maximize their light-manipulating capabilities. This will involve:

Simulation and Modeling: Extensive numerical simulations will be conducted to study the light-matter interaction within the new metasurface configuration. Optimization algorithms will be employed to identify the most effective patterns and structures.

Experimental Validation: Prototype devices will be fabricated and rigorously tested in controlled environments. These experiments will validate theoretical predictions and refine the models based on empirical data.

In summary, by transitioning to all-dielectric metasurfaces and addressing the limitations of plasmonic materials, this proposed future work aims to significantly advance the field of nanophotonics. The proposed changes not only promise enhanced performance and broader applicability but also pave the way for the practical deployment of these advanced optical devices in real-world applications.